



LUND UNIVERSITY

Towards Quantitative Diagnostics using Short-Pulse Laser Techniques

Ehn, Andreas

2012

[Link to publication](#)

Citation for published version (APA):

Ehn, A. (2012). *Towards Quantitative Diagnostics using Short-Pulse Laser Techniques*. [Doctoral Thesis (compilation), Combustion Physics].

Total number of authors:

1

General rights

Unless other specific re-use rights are stated the following general rights apply:

Copyright and moral rights for the publications made accessible in the public portal are retained by the authors and/or other copyright owners and it is a condition of accessing publications that users recognise and abide by the legal requirements associated with these rights.

- Users may download and print one copy of any publication from the public portal for the purpose of private study or research.
- You may not further distribute the material or use it for any profit-making activity or commercial gain
- You may freely distribute the URL identifying the publication in the public portal

Read more about Creative commons licenses: <https://creativecommons.org/licenses/>

Take down policy

If you believe that this document breaches copyright please contact us providing details, and we will remove access to the work immediately and investigate your claim.

LUND UNIVERSITY

PO Box 117
221 00 Lund
+46 46-222 00 00

TOWARDS QUANTITATIVE DIAGNOSTICS USING
SHORT-PULSE LASER TECHNIQUES

DOCTORAL THESIS

ANDREAS EHN

Division of Combustion Physics
Department of Physics



LUND UNIVERSITY

© Andreas Ehn, 2012
Printed at Tryckeriet i E-huset, Lund, Sweden
May 2012

Lund Reports on Combustion Physics, LRCP-160
ISSN 1102-8718
ISRN LUTFD2/TFCP-152-SE
ISBN 978-91-7473-340-2

Andreas Ehn
Division of Combustion Physics
Department of Physics
Lund University
P.O. Box 118
SE-221 00, Lund, Sweden

Populärvetenskaplig Sammanfattning

Med utvecklingen av lasern tillkom ett diagnostiseringsverktyg för forskning inom medicin, biologi, fysik, kemi mm. En laser är i princip en ljuskälla som skickar ut ljus med synnerligen välbestämd färg och riktning. Ljus som har en viss färg kan påverka vissa molekyler och atomer. Under vissa förutsättningar svarar dessa ämnen genom att i sin tur skicka ut ljus i en annan färg som är typsikt för detta ämnen. Därför kan man mäta förekomsten av vissa ämnen med hjälp av laser. Det ljus som dessa ämnen skickar ut kan även bära på information av miljön som ämnet befinner sig i, såsom temperatur, tryck, förekomsten av andra ämnen osv. Det finns dock en hel uppsjö av andra mätmetoder som kan mäta liknande storheter, men den stora fördelen med laser är att man kan utföra beröringsfria mätningar, med hög precision *in-situ*, dvs att man mäter objektet i dess naturliga miljö ("på plats"). Dessa fördelar gör lasermätningar synnerligen användbara i ett flertal forskningsområden, tex i medicinforskning då man kan göra mätningar inne i kroppen eller i förbränningsforskning där man inte stör förbränningen i en motorer eller gasturbinner.

Målet med det arbete som denna avhandling bygger på har varit att utveckla och demonstrera nya laserbaserade mättekniker för undersökningar av tillämpad karraktär, med inriktning på flödesdynamik och förbränning. De problem man försökt att handskas med är mätningar i besvärliga mätmiljöer. Typer av besvärligheter kan vara stora mängder ströljus eller då även ämnen utan intresse påverkas av laserljuset och förstör mätningen. Vidare har modeller utvecklats som gör att andra forskare ska kunna förutse potentialen för detta verktyg i sin forskning. Det har även utvecklats mätmetoder som skapar tvådimensionella bilder av hur ämnenas responsignal ser ut i tidsdomänen. Sådan information är av betydelse eftersom det ger information om ämnets omgivning, och är nödvändig om man ska kunna mäta ämneskoncentrationer från dessa respons signaler. Denna mätmetod möjliggör även kvantitativa koncentrationer av ämnen i ett laserskott, vilket är en fördel när man studerar flödesdynamik och turbulens. Tekniken har vidare kombinerats med en tredje mätmetod som möjliggör mätningar av signalresponsens tidsberoende i besvärliga mätmiljöer där spritt ljus och

andra störande ljuskällor kan undertryckas. Avhandlingen innehåller även utveckling och utnyttjande av avbildande mätmetoder av ämnen som tidigare inte varit möjliga att avbilda. Slutligen har utveckling och demonstration av en typ av ljusradar utförts som möjliggör mätningar av kvantitativa koncentrations- och temperaturmätningar med mycket hög rumsupplösning.

Abstract

Laser based diagnostic tools have had an exploding impact on fundamental as well as applied research in a number of disciplines, such as biomedicine, physical chemistry etc over the last decades. Whereas fundamental research often investigate phenomena in extreme conditions, applied research aims at performing *in-situ* measurements, in order to understand the many aspects and entangled phenomena that affects the research of interest. Moreover, laser measurements performed in applied research often aims at presenting images, since variations, fluctuations and the complexity of dynamical events are better viewed and understood in its context, which is provided in an image. Therefore, a number of diagnostic techniques have been developed and demonstrated in this work to facilitate laser-based studies in problematic environments. Issues that often makes optical measurements problematic could be scattered light and interfering photo-induced signals. Picosecond lasers and short gated ICCD cameras has been used to suppress interfering signals in Raman as well as fluorescence studies. Moreover, a model so simulate the detection has been developed that should be used to evaluate the potential of performing temporal filtering. By using this evaluation tool, a specific experimental setup can be evaluated in Raman as well as fluorescence measurements, if the system is characterized and the temporal shape of the signals are known. Temporal filtering should be considered as a complementary to other filtering techniques, such as spectral or polarization filters. The simulating detection model was further developed to determine temporal shapes of signals in an image. We call this technique DIME, Dual Imaging with Modeling Evaluation, since two acquired images are combined and evaluated by modeling the detection of these two images. The most common application of such a scheme is fluorescence lifetime imaging (FLI), which is a widely used optical tool in biomedicine. In comparison to traditional FLI techniques, the DIME concept allows higher signal-to-noise ratios. Furthermore, a rapid lifetime determination algorithm is presented, called RGP-LD (Ramped Gain Profile-Lifetime Determination), that shows promising potential for fluorescence lifetime imaging, especially in combination with DIME. The DIME concept has been utilized to achieve quenching corrected fluorescence images of formaldehyde in a flame, as well as quantitative oxygen concentration measurements in toluene seeded N_2/O_2 flows. DIME was also evaluated in combination with an optical measurement technique called SLIPI (Structured Laser Illumination Planar Imaging). The combination of techniques was able to provide quantitative fluorescence lifetime data even though the signal was collected through multiple scattering media. Picosecond lasers and fast detection systems, such as streak cameras, MCP-PMT, where used to demonstrate and develop picosecond LIDAR (LIght Detection And Ranging). Such a scheme allows single ended measurements in case of limited optical access, which most often is the case in practical applications.

List of Papers

This thesis is based on the following papers, which will be referenced by Roman numerals in the text. The papers are referenced and appended to the thesis in the order listed here.

- I. **Ehn, A.**, Kaldvee, B., Bood, J., Aldén, M., *Development of a temporal filtering technique for suppression of interferences in applied laser-induced fluorescence diagnostics*, Appl. Opt., **48**, 2373-2387, 2009.
- II. Kaldvee, B., **Ehn, A.**, Bood, J., and Aldén, M., *Development of a picosecond lidar system for large-scale combustion diagnostics*, Appl. Opt., **48**, B65-B72, 2008.
- III. Wang, Z. H., Li, B., **Ehn, A.**, Sun Z., Li, Z., Bood, J., Aldén, M., Cen, K. F., *Investigation of flue-gas treatment with O₃ injection using NO and NO₂ planar laser-induced fluorescence*, Fuel, **89**, 2346-2352, 2010.
- IV. Johansson, O., Bood, J., Li, B., **Ehn, A.**, Li, Z., Sun, Z., Jonsson, M., Konnov, A., Aldén, M., *Photo-fragmentation laser-induced fluorescence imaging in premixed flames*, Combustion and Flame, **158**, 1908-1919, 2011.
- V. **Ehn, A.**, Johansson, O., Bood, J., Arvidsson, A., Li, B., and Aldén, M., *Fluorescence lifetime imaging in a flame*, 33rd International Symposium on Combustion, 2010.
- VI. **Ehn, A.**, Johansson, O., Arvidsson, A., Aldén, M., and Bood, J., *Single-laser shot fluorescence lifetime imaging on the nanosecond timescale using a Dual Image and Modeling Evaluation algorithm*, Opt. Express, **20**, 3043-3056, 2012.
- VII. **Ehn, A.**, Jonsson, M., Johansson, O., M., Aldén, M. and Bood, J., *Quantitative oxygen concentration imaging in toluene atmospheres using Dual Imaging with Modeling Evaluation*, Submitted to Exp. Fluids (2012).

- VIII. **Ehn, A.**, Levenius, M., Jonsson, M., Aldén, M., and Bood, J., *Temporal filtering in spontaneous Raman studies*, submitted to Journal of Raman Spectroscopy (2012).
- IX. **Ehn, A.**, Kristensson, E., Johansson, O., Aldén, M., and Bood, J., *Fluorescence Lifetime Imaging Through Scattering Media using Dual Imaging Modeling Evaluation in combination with Structured Laser Illumination Planar Imaging*, Conference paper to LACSEA, San Diego 2012.

Related Work

- A. **Ehn, A**, Høgh, J., Graczyk, M., Norrman, K., Montelius, L., Linne, M., and Mogensen, M., *Electrochemical Investigation of Nickel Pattern Electrodes in H_2/H_2O and CO/CO_2 Atmospheres*, J. Electrochem. Soc., **157**:B1588-B1596, 2010.
- B. **Ehn, A**, Høgh, J., Graczyk, M., Norrman, K., Montelius, L., Linne, M., and Mogensen, M., *Electrochemical measurements made in dry CO/CO_2 and H_2/H_2O atmospheres on single crystal YSZ using pattern electrodes*, Proceeding of the 26th Risø International Symposium on Material Science: *Solid State Electrochemistry*, Editors: S. Linderoth, A. Smith, N. Bonanos, A. Hagen, L. Mikkelsen, K. Kammer, D. Lybye, P. V. Hendriksen, F. W. Poulsen, M. Mogensen, W. G. Wang, Risø National Laboratory, Roskilde, Denmark, 177 - 183, 2005.

Contents

Abstract	i
Populärvetenskaplig Sammanfattning	i
List of Papers	v
Related Work	vii
Contents	ix
1 Introduction	1
2 Background Physics	5
2.1 Quantum mechanics	5
2.2 Molecular Physics	7
3 Molecular Response to Laser Perturbation	11
3.1 Prior to Light Matter Interaction	11
3.1.1 Light	11
3.1.2 Matter described as Dipoles	13
3.1.3 Molecular Energy Diagram	14
3.2 Light-Matter interaction	16
3.2.1 The Dipole Approximation	17
3.2.2 Absorption	17
3.2.3 Linewidth and broadening effects	19
3.3 Laser induced energy transfer effects	21
3.3.1 Population distribution	22
3.3.2 Collisional Quenching	23
3.4 Fluorescence signal	24
3.5 Scattering processes	26

4	Experimental Equipment	29
4.1	Lasers	29
4.1.1	Q-switched lasers	30
4.1.2	Mode-locked lasers	31
4.1.3	Characterization of pulse duration and time jitter	33
4.2	Detectors	33
4.2.1	MCP-PMT	34
4.2.2	Streak Camera	35
4.2.3	ICCD camera	37
5	Temporal Filtering	39
5.1	Picosecond laser diagnostics	39
5.2	Temporal Filtering	40
5.2.1	Temporal Filtering in Fluorescence Measurements	45
5.2.2	Temporal Filtering in Raman Scattering Measurements	50
5.2.3	Signal-to-noise limits in filtering and background subtraction schemes	58
6	Fluorescence Lifetime Imaging (FLI)	63
6.1	Lifetime Determination	63
6.1.1	Lifetime determination in the frequency domain	63
6.1.2	Lifetime determination in the temporal domain	65
6.1.3	Comparisons between the lifetime determination algorithms	69
6.2	Dual Imaging with Modeling Evaluation	73
6.2.1	Single shot accuracy and precision	77
7	Quantitative imaging	81
7.1	Differential Absorption LIDAR (DIAL)	81
7.1.1	DIAL Experimental Arrangement	82
7.1.2	DIAL Results	82
7.2	Visualization of nitric oxide concentration using Planar Laser Induced Fluorescence	83
7.2.1	NO-PLIF Experimental Arrangement	85
7.2.2	NO-PLIF Results	85
7.3	Fluorescence Lifetime Imaging Measurements	87
7.3.1	Single-shot FLI of sub-nanosecond lifetimes	87
7.3.2	Quenching corrected PLIF of formaldehyde in a flame	88
7.3.3	Oxygen concentration measurements	89
7.4	Quantitative measurements in scattering environments	91
8	Conclusion	97

9 Outlook	99
Acknowledgements	105
Bibliography	105
Summary of Papers	113

Chapter 1

Introduction

SINCE 1960, when the first molecules were exposed to laser light [1], the number of application for laser diagnostics has exploded. Still new commercial and scientific fields will benefit from use of lasers in the future. The particular advantages of laser-based diagnostic measurements is that they allow the following:

Remote measurements, in the sense that the measurement object can be located far away or be inside a closed environment. Good examples of distant measurement objects are to be found in atmospheric [2] and explosive detection studies [3], and examples of closed-in measurement objects are present in medical [4] as well as in combustion engine [5] studies.

Non-intrusive measurements, in which laser light interacts with a small portion of the molecules in the probe volume without use of probes or physical sampling. Physical phenomena studied on a macroscopic scale are not disturbed by the quantum mechanical information transfer that occurs on a quantum scale between photons and molecules or atoms.

Species-specific measurements, in which the energy of the laser light can be tuned to the resonant transition of particular molecules being studied, or spectroscopic studies of non-resonant measurement techniques.

Spatial selectivity, in which the probe volume is defined by the laser and the detection it achieves, such as in planar laser induced fluorescence imaging [6].

Temporal selectivity, in which the time delay between the probe and

detected signal is very short [7]. This can be achieved by use of pulsed lasers, which then provide spatially selective images with a high degree of temporal resolution, much like flash photography.

These advantageous features make laser-based diagnostic tools ideal for a variety of studies in applied science. Such studies very often involves the combined occurrence of many exceedingly complex phenomena. When more sophisticated models, instrumentation and experimental tools are employed, competences of three different types may be needed to understand such phenomena. First, in order to control and to understand macroscopic phenomena, engineering competence is of utmost importance. Second, in order to perform well controlled laser measurements of macroscopic phenomena, experimental physics is needed. Finally, numerical modeling of the often entangled physical, chemical and mechanical phenomena may need to be carried out in order to be able to describe details of the phenomena in their entirety. When highly sophisticated models are being dealt with, a combination of numerical, mechanical and physiochemical expertise can be called for to adequately manage to combine modeling clusters. Examples of applied research fields within energy science in which such multidisciplinary considerations are involved are the following:

Engine research, in which *in situ* measurements provide information concerning mixing, evaporation, ignition, combustion and the like [8]. Work in this area is a multi-billion dollar industry in which laser-based measurement tools often provide essential information.

Flow studies, in which temporally and spatially resolved measurement results concerning mixing and turbulence can be used to validate fluid mechanical models [9]. Such models are of vital importance for optimization and for gaining an adequate understanding of aerodynamics, the geometries involved in large scale mixing, and the like.

Applied catalysis, in which models based on heterogeneous electrochemistry kinetics in combination with fluid dynamics and gas-phase chemistry benefit from *in situ* measurements both for obtaining *in-data* and for validation purposes. Catalysis research in this area benefits from such work in its providing of fundamental understanding of the problems involved, and its contributing to the development and testing of new materials [10].

Gas turbine research, in which studies of flashback, emission and combustion mixing for example need to be studied under real, or at least in adequate, conditions [11].

Spray diagnostics, in which in-data and the validation of models are critical, especially since there are very few tools that can provide experimental results concerning such dense measurement objects [12].

An overall aim within energy related research fields of this sort is to provide cost-efficient and environmentally friendly energy conversion. Typical problems that need to be kept to a minimum are the emission of toxic molecules such as of nitric oxides (NO_x) and of carbon monoxide (CO). In order to minimize emission containing such product gases, as thorough a characterization of the combustion conditions as possible needs to be achieved. On a global scale, combustion-product gases that contribute to the greenhouse effect should be kept to a minimum. Carbon dioxide (CO_2), an inevitable product of combustion, is perhaps the most common discussed greenhouse gas. Through optimizing the energy produced by combustion processes, the emission of carbon monoxide can be minimized. Other greenhouse gases, such as methane, are products of incomplete combustion, resulting from the failure to optimize combustion conditions adequately.

In research fields concerned with combustion, the steep gradients of temperature, pressure and species-concentration as well as the turbulence, the multi-phase media, the droplets and solid particles, and the like that, sum up just about all practical challenges for using optical techniques. Accordingly, various of the measurement techniques employed and the conclusions drawn in the present work are applicable to other research fields as well, in which use is made of laser-based diagnostics. Biomedicine is one of the fastest growing research fields of this sort in which optical laser techniques are utilized, spontaneous Raman scattering, laser-induced fluorescence and fluorescence lifetime imaging being of interest there as well. In ongoing work on proteins [13], cell biology [14], cancer [15] and Parkinsons disease [16] for example, there is likewise a very strong need of better measurement schemes and better tools.

The work presented in the thesis is aimed at helping to provide more adequate tools for experimentalists, enabling them to better understand to use in order to better understand, diagnose and optimize energy conversion. The work can also be seen as applicable to research in the area of biomedicine, where better knowledge of the diagnosis and cure of harmful diseases is extremely important.

In the chapters immediately following, certain background physics relevant to the work that has been carried out, will be taken up, for example, the microscopic world of molecules (Chapter 2) and the physical processes that make quantitative laser-induced fluorescence troublesome (Chapter 3). In the latter chapters, certain background physics concerning the light matter interaction is also being reviewed. Chapter 4 concerns the equipment used in the experimental work. In Chapter 5 the temporal filtering used to

suppress interfering signals is being dealt with. In that chapter the work presented in Papers I and VIII is summarized, and the evaluation routines used in determining the effects of the temporal filter in the fluorescence and Raman studies are discussed. Chapter 6 starts with a review of algorithms for determining decay times that can be used in ICCD camera imaging. One of these schemes, termed RGP-LD, was dealt with in Paper VI. An evaluation routine termed DIME for determining the temporal shapes of signals is likewise presented in that paper. In Chapter 7, various examples of quantitative measurements are reported on in Papers II, III V, VI, VII and IX. In Chapter 8 the work as a whole is summarized and in the final chapter the future perspectives within this area are explored.

Chapter 2

Background Physics

THIS chapter provides a brief overview of molecular physics from an experimentalist point of view, laser-based studies being dealt with on a molecular level. In modern textbooks on quantum mechanics, [17], [18], [19], [20], the pedagogic framework is most often built around the mathematical model describing the physical nature of atoms and molecules. The present chapter aims at presenting certain of the fundamental ideas of quantum mechanics and molecular physics from a partly standpoint.

At the beginning of the twentieth century, Lord Kelvin published an article in the Philosophical Magazine entitled; "Nineteenth century clouds over the dynamical theory of heat and light" [21], one of these clouds that Lord Kelvin was referring to being the inconsistency between experimental results and theory regarding black body radiation. An explanation of this inconsistency was presented by Max Planck [18], this providing an initial glimpse of quantum mechanics, which can well be regarded as representing the most important part of modern physics as we know it today.

2.1 Quantum mechanics

The revolutionary idea that Max Planck proposed here was that atoms and molecules have internal energy distributions that differ from what had been taught in classical physics. It appeared that these small elements had quantized energy distributions, rather than the continuous energy distributions, described in classical physics as being characteristic of matter generally. As Planck's hypothesis was tested and the insights regarding it were shared and became established, a more complete picture of the nature of these systems appeared and a theoretical quantum mechanical model was constructed. In modern quantum mechanic textbooks, a number of postulates are listed that

2. BACKGROUND PHYSICS

define the core of quantum mechanics. For a detailed account and discussion of these postulates, see e.g. [18] and [22]. The postulates involved can be divided into three separate parts:

1. The definition of an ensemble of physical states, $|\alpha\rangle$.
2. Guidelines on how to interpret and measure observables with use of linear operators.
3. The time evolution of a physical system as determined on the basis of the time-dependent Schrödinger equation.

The first of these defines the system, which for an experimentalist can be either a molecule or an atom. The theoretical representation of a molecule can be described by use a state function that includes all the information that can be measured for the system, $|\alpha\rangle$. The formalism for describing states as $\langle\alpha|$ and $|\alpha\rangle$ is called the bra-ket notation. Even though the measurement of such a system determines one particular state, $|a_n\rangle$, the physical system as a whole represents the superposition of all possible states of it prior to measurements being conducted.

$$|\alpha\rangle = \sum_n |a_n\rangle. \quad (2.1)$$

The second part of the postulates above states that each entity of a physical state A that is observable through measurements has a corresponding theoretical measurement (linear) operator \hat{A} . Similar to an experiment, in which a physical system is exposed to an experimental test, such an operator pertains to a physical state, i.e. $\hat{A}|\alpha\rangle$. The results of any such a precise theoretical experiment can only be an eigenvalue a_n of the operator. The theoretical experiment involved can be written as

$$\hat{A}|\alpha\rangle = a_n|a_n\rangle. \quad (2.2)$$

If a number of experiments corresponding to the operator \hat{A} are conducted on identically prepared molecules, the expectation value of these results can be calculated as

$$\langle\hat{A}\rangle = \frac{\langle\alpha | \hat{A} | \alpha\rangle}{\langle\alpha | \alpha\rangle}. \quad (2.3)$$

Mathematically, the state function of the molecule can be expressed as a linear combination of the eigenfunctions of the operator \hat{A} , provided \hat{A} is a self adjoint operator. Basically, this means that the operator \hat{A} is associated with an observable. Note that some experiments cannot be combined in a sequence. The theoretical analogy to this is that of two theoretical experiments (operators) do not commute. On the other hand, if the results of two

sequential experiments, regardless of the order in which they were conducted, are identical, the state function after corresponding theoretical measurement (operator) is expressed by identical eigenfunctions, which means that

$$\hat{A}\hat{B}|\alpha\rangle = \hat{B}\hat{A}|\alpha\rangle. \quad (2.4)$$

These postulates form the basis for a model used to perform theoretical measurements of physical state functions. By performing experimental and theoretical measurements on physical systems such as molecules, the nature of the microcosmos can be better understood. This can be utilized, for example in applied laser-based measurements.

2.2 Molecular Physics

Information concerning the energy structure of a molecule can be obtained by making the molecules interact with photons in carefully designed laser experiments. The results of such an experiment are displayed in Figure 2.1, in which an excitation scan of nitric oxide (NO), as recorded in a flame, is shown. The x -axis indicates the photon energy that excites a transition of the NO molecules, each peak position corresponding to the energy difference between the two discrete energy levels involved.

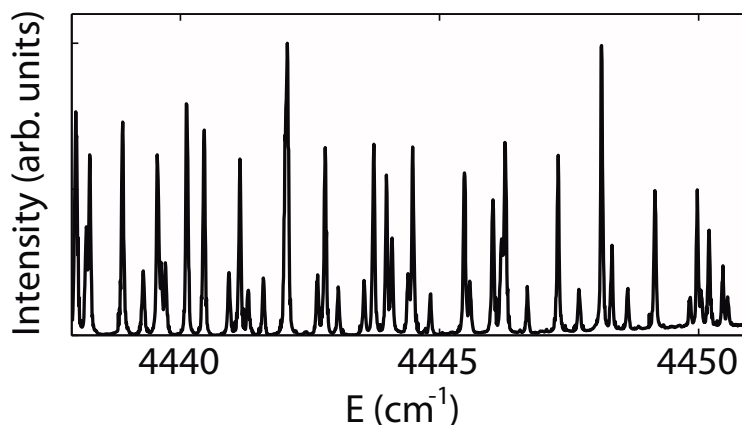


Figure 2.1: An excitation scan of NO recorded in a McKenna flame under Stoichiometric conditions.

As stated in Section 2.1, the second part of the quantum mechanical postulates deals with observables that can be determined on the basis of measurements. Such an observable can be the molecular energy associated with the total energy operator, i.e. the Hamiltonian \hat{H} . The Hamiltonian is a theoretical experiment that results in the energy levels of the eigenvalues

2. BACKGROUND PHYSICS

of the molecule \hat{H} acting on the molecular state function. The internal energy of a molecule is distributed over its different physical properties. For a laser spectroscopist, the internal energy of interest would be the energy of the electrons and the vibrational and rotational energies associated with the motion of the nuclei. Even though a molecule binds higher energies, for example in the nuclei, these sources of energy are not of interest in connection with laser spectroscopy. This is why the electronic, the vibrational and the rotational energy together are referred below to as the total energy.

Whereas rather complex models are needed for determining the energy structure of complex molecules, fairly straightforward concepts have been developed for describing the simplest type of molecules, diatomic molecules, such as OH and NO , for example. It should be emphasized that these schemes include a number of approximations. For a diatomic molecule, the Hamiltonian describing the molecular energy can be written as

$$\hat{H} = \hat{T}^N(R, \theta, \phi) + \hat{T}^e(r) + \hat{V}(r, R). \quad (2.5)$$

Here \hat{T}^N is the kinetic energy of the nuclei, \hat{T}^e is the electron kinetic energy and \hat{V} is the electrostatic potential energy of the electrons and the nuclei. The spatial parameters R and r are the internuclear distance and the coordinates of the electrons, respectively, in the fixed system of the molecule. The angles θ and ϕ are the rotational angles of the internuclear axis, which can be seen in Figure 2.2.

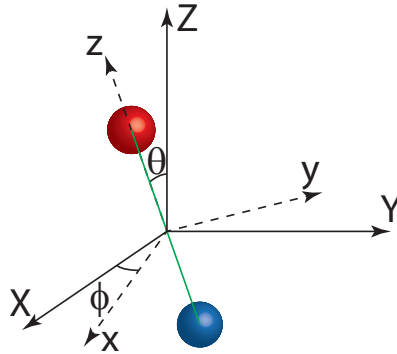


Figure 2.2: *The two angles θ and ϕ describe the rotation of the internuclear axis of the molecule with respect to the spatially fixed coordinate system, ϕ being the rotation around Z , and θ being the rotation around y .*

In order to calculate the discrete energy spectrum for a diatomic molecule, the Hamiltonian, as displayed in Equation 2.5, needs to be solved. To calculate such a solution, all the operators incorporated into the Hamiltonian need to commute, however, which is not the case for a rotating and vibrating diatomic molecule. Accordingly, the three energy contributions are set

as being independent of each other, dividing the problem into three separate parts. This assumption is called the Born-Oppenheimer approximation.

Whereas the electronic contribution is rather tedious to calculate, the vibrational and rotational structures can be modeled quite easily. Note that such modeled spectra are approximations of the eigenvalues of the exact Hamiltonian. For the identification of spectra, for example, and for gaining an understanding of the spectral complexity involved such models serve a purpose. An empirically validated description of the vibrational energy levels (G) at hand can be described by the power series expression

$$G(v) = \omega_e(v + 1/2) - \omega_e x_e(v + 1/2)^2 + \dots \quad (2.6)$$

Here, v is the vibrational quantum number, ω_e is the harmonic vibrational frequency, and $\omega_e x_e$ is the first order anharmonic vibrational constant. In addition, the rotational energy (F) of the molecule can be written as

$$F(J) = B_v J(J + 1) - D_v [J(J + 1)]^2 \dots \quad (2.7)$$

where B_v and D_v are the rotational and the centrifugal distortion constant, respectively, for the v :th vibration. The calculated and the experimentally measured values for the constants mentioned above are listed by Huber and Herzberg in [23].

The work presented in the thesis includes investigations of a number of different molecules, some of them shown in Figure 2.3. Without discussing the molecular energy structure of these particular molecules in detail, it should be noted that the complexity of the energy structure of a molecule grows with the complexity of the molecule. The energy spectra in, acetone and toluene, for example can be considered as nearly continuous as compared with OH and NO . The separation between the energy levels involved plays a very considerable role in the dynamic of the molecule as it interacts with its surroundings.

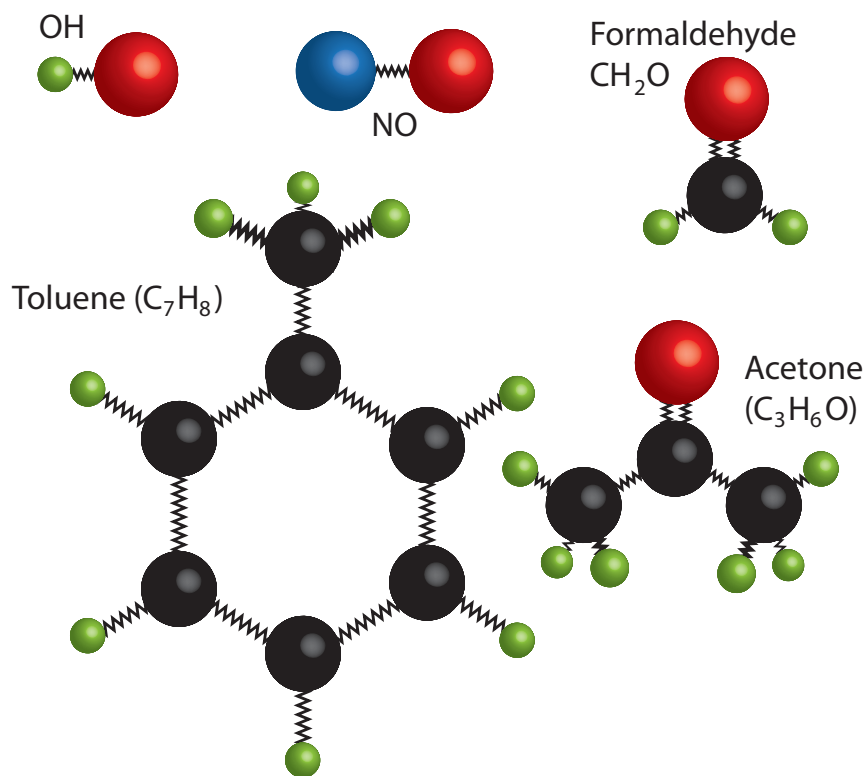


Figure 2.3: A number of molecules that were investigated within the framework of the thesis. Experiments concerning OH and formaldehyde were performed in combustion studies, whereas NO was probed in thermo-neutral chemistry studies. Both acetone and toluene were used as tracer molecules in flow studies.

Chapter 3

Molecular Response to Laser Perturbation

IN laser based measurements, light interacts with matter in the measurement volume. In contrast to continuous lasers, short-pulse lasers provide a natural signal and information flow in the temporal domain. This chapter describes some of the physics behind laser-induced fluorescence (LIF) as well as Raman and Rayleigh scattering in the context of an experiment performed with use of a short-pulse laser. The conception of a basic linear LIF experiment, as presented in the text, is shown in Figure 3.1, where t_0 is the time prior to interaction, and where matter and light can be discussed separately. Since light and matter interact at t_1 , molecular absorption of the electromagnetic radiation occurs. Following absorption, when the laser pulse has left the measurement volume at time t_2 , the molecules relax to their ground state.

3.1 Prior to Light Matter Interaction

In order to understand the interaction between light and matter, the individual components need to be understood. Accordingly, a brief overview both of light and of matter is presented, together with physical and mathematical interpretations of the two.

3.1.1 Light

As in the case of most physical phenomena that occur in a microcosmos, the laser beam that enters the probe volume in a laser experiment can be described by a classical or quantum mechanical model. The classical picture

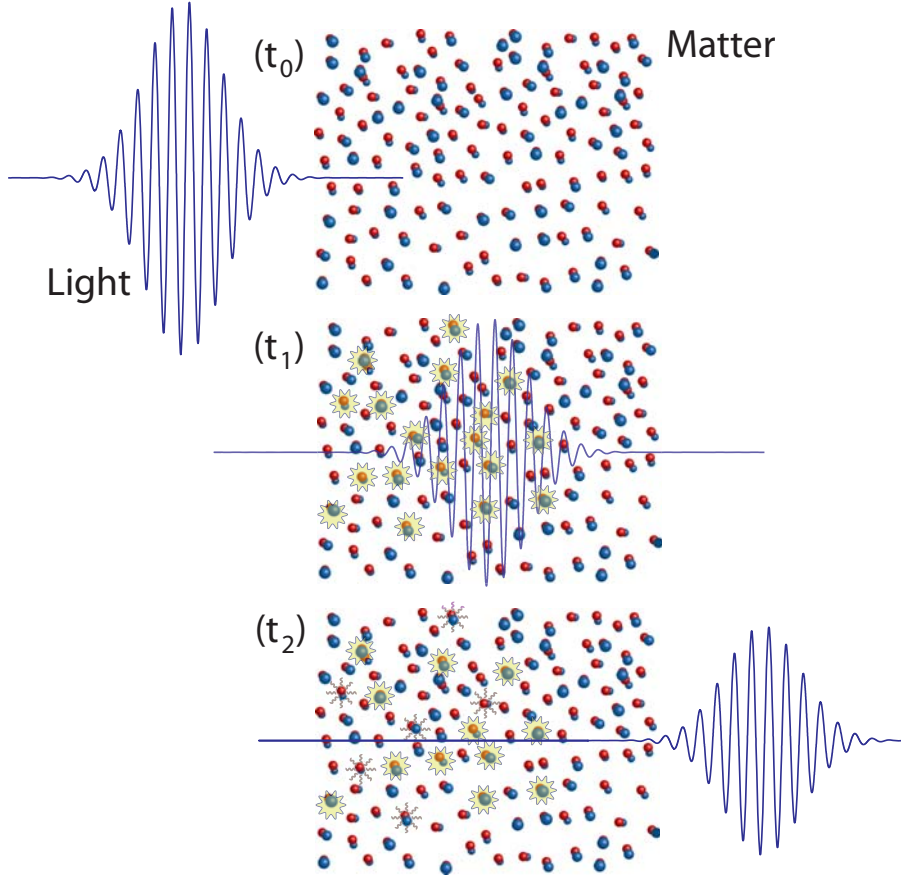


Figure 3.1: A description of the light matter interaction in a basic LIF experiment. Here, (t_0) indicates the time prior to interaction, and (t_1) images of the situation in which light interacts with matter. The molecules that are highlighted excited, and (t_2) displays the molecules as they return to their ground state, in which light is emitted from the molecules.

describes the light as consisting of electromagnetic waves that propagate orthogonally to the oscillating electric and magnetic fields. Such a description is applies when Maxwell equations are solved in free space [24]. The electric field can be written then as

$$\vec{E}(\vec{r}, t) = E_0(\omega) \sin(\vec{k} \cdot \vec{r} - \omega t + \delta_\omega) \vec{\epsilon}. \quad (3.1)$$

Here, \vec{k} is the wave vector, its pointing in the direction of propagation, \vec{r} is the spatial coordinate, ω is the angular frequency, δ_ω is the phase and $\vec{\epsilon}$ is the direction of the polarization of the electric field. The strength of the electric field can be expressed in terms of irradiance. In the present text the

irradiance, I , is defined as the strength of the effect per unit area (W/m^2):

$$I(\omega) = \frac{c}{2}\varepsilon_0 E_0(\omega)^2. \quad (3.2)$$

where c and ε_0 are the speed of light and vacuum permittivity, respectively. In the quantum mechanical concept of this, particles called photons are used to describe light. The irradiance expressed in the photon picture is written as

$$I(\omega) = \frac{N_\gamma \hbar \omega c}{V}. \quad (3.3)$$

where the energy of one photon is $E_\gamma = \hbar\omega$, and where N_γ is the number of photons hitting the area A per second, \hbar is the reduced Planck constant and V is the volume containing the photons that hit the area A every second. The work presented in the thesis was carried out for the most part with use of laser pulses having a duration of tens of picoseconds. To describe a pulse of light, the electric field expressed in Equation (3.1) is multiplied by an envelope function, that describes the shape of the laser pulse. The total description of the electric field of a laser pulse can then be written as

$$\vec{E}_{Pulse} = \vec{E}(\vec{r}, t) E_{Env}(\vec{r}, t). \quad (3.4)$$

For the simulations of fluorescent signals reported in Paper VIII, the envelop function was a hyperbolic secant function, following the recommendation of Settersten and Linne [25]. For simplicity, the direction of light propagation is from hereon defined as the y-direction.

3.1.2 Matter described as Dipoles

The interaction between a rapidly oscillating electric field and matter can be described by considering matter as representing dipoles. In classical physics, a dipole is a description of an electrically polarized body, the negatively and positively charged parts (with charge $|q|$) of which are separated by the distance $|\vec{r}|$. For a body in which the two poles are considered as points, the dipole moment can be written as

$$\vec{\mu} = q\vec{r}, \quad (3.5)$$

where the direction of the vector \vec{r} is defined as extending from the negative to the positive pole [26]. In accordance with this definition, the electronic dipole moment of a molecule corresponds to the imbalance in electric potential of the molecule. In a classical sense, the interaction between a molecule and an electromagnetic wave is described as the dipole response to the electromagnetic field. In a quantum mechanical sense, the operator that describes the interaction between an electromagnetic field, \vec{E} , and the

molecule is called the dipole moment operator, $\hat{\mu}$. The so-called electronic dipole moment, $\hat{\mu}_e$, couples the two electronic energy levels and enables transition between the two states to take place. Photons, the energy of which corresponds to the energy separation between electronic energy levels involved, are generally in the ultraviolet (UV) region. Since the electronic structure is affected by electronic transitions, $\hat{\mu}_e$ is a so-called induced dipole moment.

The dipole moment operator enabling transitions between the vibrational energy levels to occur is often divided into two different parts: the permanent $\hat{\mu}_{p,v}$ and the induced dipole moment, $\hat{\mu}_{i,v}$. The interaction between the permanent dipole moment and the electromagnetic field describes the photon-absorption process, which sets the molecule into an excited vibrational state if the permanent dipole moment is dependent upon the inter-atomic distance within the molecule. The photon energy for such a resonant transition lies in the infrared (IR) domain. Similar to the electric dipole moment, $\hat{\mu}_{i,v}$ is induced by the electromagnetic field. The induced dipole moment is formed as the electromagnetic field polarizes the molecule by affecting the charge distribution of the molecule. The ability of being polarized, called the polarizability, α , is related to the induced dipole moment as

$$\vec{\mu}_{i,v} = \vec{\alpha} \cdot \vec{E}. \quad (3.6)$$

The interaction between the electromagnetic field and the induced dipole moment builds upon the theory behind Rayleigh and Raman scattering.

3.1.3 Molecular Energy Diagram

As stated in Chapter 2, the internal molecular energy is distributed in discrete levels. An example of such molecular energy levels is displayed in Figure 3.2. Prior to perturbation by electromagnetic waves, the population of the molecules in the probe volume is Boltzmann distributed [27]. As molecules are perturbed, either by light or by collisions with other molecules, energy transfer occurs. The most commonly used models for describing energy-transfer phenomena in atoms and in molecules are those of the density matrix and of the rate equation theory. The density matrix approach is a way of employing quantum mechanics to ensembles of systems (molecules or atoms) that have not been prepared identically. This is done by inferring a density matrix that describes the statistical distribution of the ensemble of molecules with respect to their states. The density-matrix formalism is well described in most quantum mechanic books, see e.g. [18], [19] and [28].

The rate equation model is more straightforward, since such quantum mechanical effects as coherence are excluded. Instead, the molecules can only be in one single state at a specific time. An example of a molecular energy

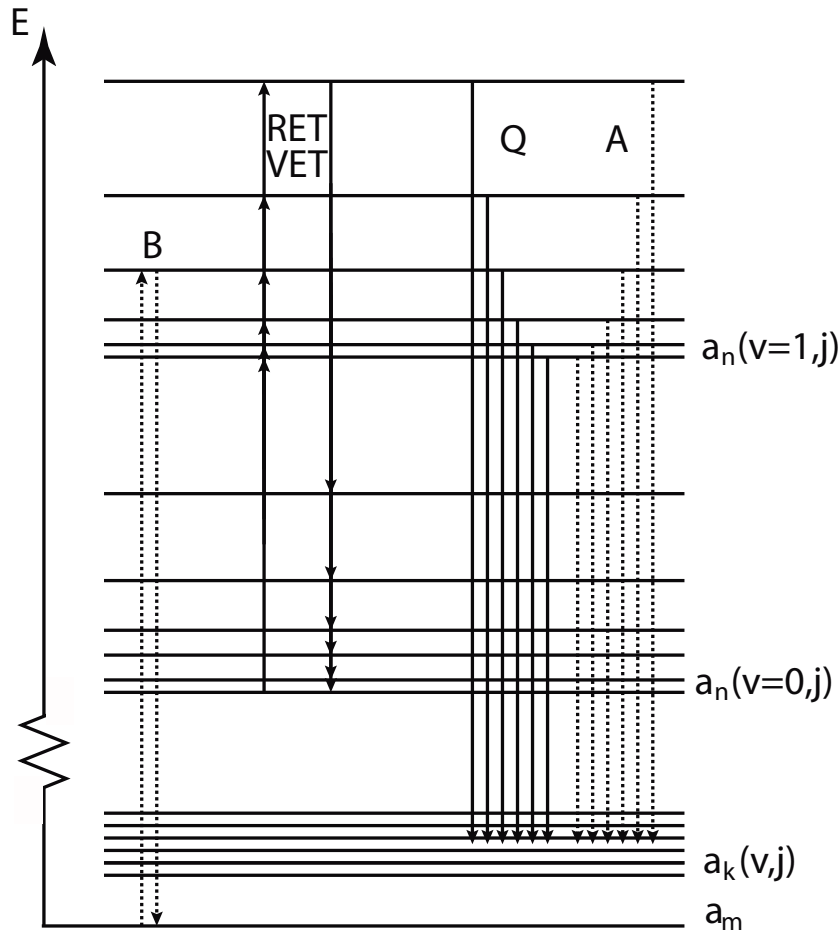


Figure 3.2: *The different energy transition processes in a molecule. The laser wavelength is tuned to match a transition from the ground state, a_m , to an excited state $a_n(v = 1, j = 3)$, from which stimulated emission can occur if the population distribution in the excited state is sufficiently high. The population distribution is divided between the rotational and the vibration energy levels in the electronically excited states by collisionally induced vibrational and rotational energy transfer processes. The molecules end up in the ground state through spontaneous emission or through collisional quenching, the latter being a radiation-free energy transfer process.*

diagram is presented in Figure 3.2, the ground state being denoted there as a_m , and higher rotational and vibrational states at the lower electronic level being termed a_k . The vibrational and rotational energy levels in the excited electronic state are designated as a_n .

3.2 Light-Matter interaction

As a laser pulse propagates (in the y -direction) through a measurement volume, the energy of the electromagnetic wave is transferred to the molecules. In a simple description of this, the absorption that occurs is proportional to the number density of the molecules (N) and their absorption cross-section (σ_0), i.e.

$$\frac{d}{dy}(I(y, \omega)) = -N\sigma_0g(\omega)I(y, \omega). \quad (3.7)$$

Here, (σ_0) is the frequency integrated absorption cross-section. The spectral line-width function, $g(\omega)$, includes line broadening due to collisions, Doppler broadening and the natural linewidth. The spectral linewidth function provides a compact description of the probability of interaction between the laser light (which has a certain linewidth) and the interacting molecules. As can be seen in Equation 3.7, the interaction between the laser light and the molecules depends on the product (overlap) of the line-width functions, $I(\omega)$ and $g(\omega)$. This product describes the probability of an ensemble of molecules interacting with photons having energies described by another statistical probability, namely that of the spectral linewidth of the laser. The absorption cross section, σ_0 , is often given in units of cm^{-2} . The above picture includes an ensemble of molecules that are nonidentical, and which thus cannot be analyzed with use of pure quantum mechanics. Accordingly, the relationship between the electronic dipole moment and the absorption cross-section will be dealt with by analyzing at the start an ensemble of identical molecules and applying the results obtained to a group of molecules having different properties, such as those of polarization.

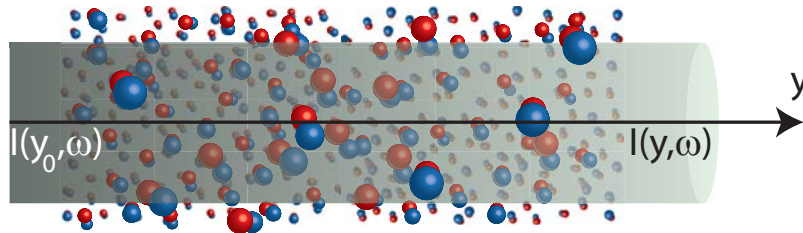


Figure 3.3: When the laser is tuned to a molecular absorption line, the laser irradiance is reduced as it propagates through the measurement volume in accordance with Equation 3.7.

3.2.1 The Dipole Approximation

When a molecule is perturbed by an electromagnetic wave, an additional term, $\hat{H}'(t)$, is added to the Hamiltonian.

$$\hat{H} = \hat{H}_0 + \hat{H}'(t). \quad (3.8)$$

For electronic excitation, the perturbation part of the Hamiltonian can be expressed as the electronic dipole moment operator times the electric field that is applied:

$$\hat{H}'(t) = -\hat{\mu}_e \cdot \vec{E}(t). \quad (3.9)$$

This is the dipole approximation, in which it is assumed that the wavelength of the electromagnetic wave is much longer than the size of a molecule. Note that the dipole approximation does not make the time-dependent electric field equivalent to a time-invariant electric field. An oscillating electromagnetic field is the classical equivalent to the photon as it is conceived, whereas a time invariant field shows a constant perturbation. The photon energy is tuned to match the energy difference between the two states needed to make the molecule undergo a transition.

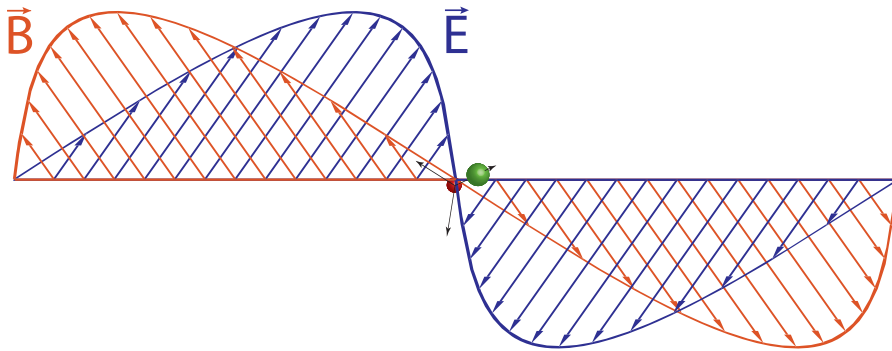


Figure 3.4: A diatomic molecule perturbed by an electromagnetic field. The vector describes the orientation of the molecule (Figure 2.2). Note that the dipole moment and the electrical field components are not aligned.

3.2.2 Absorption

A molecule is perturbed by the applied electric field as the laser wavelength is tuned to match a transition. The wavelength that enables a transition between two electronic states to take place is

$$\lambda = \frac{hc}{\Delta E} = \frac{hc}{E_n - E_m}. \quad (3.10)$$

3. MOLECULAR RESPONSE TO LASER PERTURBATION

Since the electric field is assumed to be uniform across the entire molecule, it can be expressed as

$$\vec{E}(t) = -E_0(\omega)\sin(\omega t - \delta_\omega)\vec{\varepsilon}, \quad (3.11)$$

where δ_ω is the relative phase of the electric field.

The time-dependent probability of finding the molecule in the excited state, $|a_n(t)|^2$ can be calculated using time-dependent perturbation theory. This probability involves two separate terms. The term that dominates when the photon energy is equal to ΔE describes absorption, whereas for the energy $-\Delta E$ the term responsible for stimulated emission dominates. These energy transfer processes are shown in Figure 3.2 as the arrows under *B*. In the case of absorption, the probability of finding the molecule in the upper state can be written as

$$|a_n(t)|^2 = \frac{1}{2} \left(\frac{E_0(\omega)}{\hbar} \right)^2 |\langle a_n | \vec{\varepsilon} \cdot \hat{\mu}_p | a_m \rangle|^2 \frac{1 - \cos[(\omega_{nm} - \omega)t]}{(\omega_{nm} - \omega)^2}. \quad (3.12)$$

The last term is proportional to a quadratic sinc-function.

In order to calculate the transition rate, the laser irradiance is used instead of the electric field. The laser irradiance instead of the electric field is used in calculating the transition rate. At this point, only an ensemble of identically prepared molecules is considered, this satisfying the quantum mechanical postulates. In a laser-based experiment, however, the interacting electromagnetic field is usually of rather good quantity, which means that both the polarization, and the direction are well defined. To get around this problem, the reference system is arranged so that the molecules are perfectly aligned, the laser light showing random polarization and the propagation direction being arbitrary. The randomness of orientation is introduced as a factor of 1/3.

$$|\vec{\varepsilon} \cdot \vec{r}|^2 = \frac{1}{3} |\vec{\varepsilon}_z \cdot \vec{r}|^2 = \frac{1}{3} |\vec{r}|^2. \quad (3.13)$$

This factor is based on the fact that the misalignment with respect to the coordinate system is defined by the internuclear axis being equal throughout: $\langle \vec{\varepsilon}_x \rangle = \langle \vec{\varepsilon}_y \rangle = \langle \vec{\varepsilon}_z \rangle = 1/3 \langle \vec{\varepsilon} \rangle$.

In addition, the linewidth of the laser light is considered to be much broader than the linewidth corresponding to the last factor in Equation 3.12, since the transition probability is integrated over the angular frequency of the laser.

$$|a_n(t)|^2 = P_{nm}^{(1)}(t) = \frac{\pi I(\omega_{nm})}{3\hbar^2 c \varepsilon_0} |\hat{\mu}_{nm}|^2 t. \quad (3.14)$$

The transition probability (W_{nm}) is found for an ensemble of identically prepared molecules by taking the derivative of Equation 3.14. Equation

3.7 is integrated over the angular frequency, as is also done in order to find the transition rate. In the integration, the linewidth function, $g(\omega)$, is assumed to be a delta-peak since only identically prepared particles are considered. In accordance with Equation 3.7, the loss in laser irradiance as the laser propagates through the medium, i.e. $-\frac{d}{dy}I$, is equal to the number density of the molecules, times the energy for each absorbed photon, times the transition probability. Implementing this information into Equation 3.14 enables the following relationship between the absorption cross-section and the permanent dipole moment to be obtained.

$$\sigma_0 = \frac{W_{nm}\hbar\omega_{nm}}{I(\omega_{nm})} = \frac{\omega_{nm}\pi}{3\hbar c\epsilon_0} |\hat{\mu}_{nm}|^2 \quad (3.15)$$

If fluorescence signals are simulated with use of quantum mechanical models, experimentally measured absorption cross-sections can be related to the expectation value of the permanent dipole moment through the relation found in Equation 3.15. Using rate equations based on light-matter interactions as expressed by Einstein rate coefficients enables relations between these parameters to be found by use of [29]. Laser-based combustion studies are typically carried out in environments characterized by steep temperature and concentration gradients, which make the fluorescence signal troublesome to convert into quantitative concentrations. However, the dipole moment, the absorption cross-section and the absorption rate coefficient are constants that all describe the coupling between two molecular quantum states. Hence, these constants are independent of external interferences such as temperature, pressure or collisions with ambient molecules.

3.2.3 Linewidth and broadening effects

The width of an absorption line is dependent upon several physical phenomena, some of which are dependent upon local variations in temperature and on ambient molecules. The linewidth function $g(\omega)$, expressed in terms of angular frequency, can be seen in Equation 3.7. Obviously, the linewidth of the absorption line affects the number of molecules that are excited. Accordingly, the properties of natural, collisional, and Doppler broadening are discussed below.

Natural linewidth

The natural linewidth of an absorption line is dependent upon the uncertainty of the two energy levels involved in the transition. The uncertainty in the energy for a given state is inversely proportional to the lifetime of the state. If no other line broadening effects are present, the spectral line has

the shape

$$g(\omega) = \frac{1}{2\pi} \frac{\Gamma}{(\omega - \omega_{ba})^2 + \left(\frac{\Gamma}{2}\right)^2}. \quad (3.16)$$

This is a Lorentzian function, where ω_{ba} is the center angular frequency of the absorption line, and the FWHM of the linewidth function is Γ , which is the inverse of the lifetime of the excited state (provided the lower state is stable). The integral of the linewidth function, $g(\omega)$, is normalized to unity. The natural linewidth is independent of the ambient conditions, since it describes the stability of an unperturbed state.

Collisional broadening

Natural linewidths cannot be measured at atmospheric pressures or higher due to collision-induced effects. At higher pressures, collisional broadening effects are noticeable. Natural broadening and collisional broadening are both examples of so-called homogeneous broadening, which refers to the fact that all the molecules in the probe volume have the same probability of being affected by the electromagnetic field. In the case of natural broadening, the precision of the energy levels is determined by the stability of the state in question, which at higher pressures is perturbed by molecular collisions. In quantum mechanical terms the electromagnetic field perturbs the molecules, The so-called coherence being formed in the statistical ensemble of molecules. This somewhat abstract entity means that the two states involved are in coherent superposition in the ensemble. In a molecular collision, the coherence can be interrupted, affecting the stability of the state. The line shape of collisionally broadened molecules can thus also described by use of a Lorentzian function (such as Equation 3.16) but one having a larger Γ , since the lifetime is decreased by collisions.

Doppler broadening

The direction of the laser beam in the probe volume is well defined. The velocity of the molecules there is randomly distributed and can be described in terms of a statistical distribution. Since the molecules differ in their velocity components in relation to the laser light propagation, the frequency of the light is Doppler shifted. Such phenomena result in the molecules in the probe volume coming to differ in their excitation probabilities, Doppler broadening thus being termed an inhomogeneous broadening effect. Doppler broadening dominates at low pressures, whereas at higher pressures the contribution of collisional broadening to the linewidth becomes greater. A spectral line that is broadened due to the Doppler effect is written as

$$g_D(\omega) = \frac{1}{\sqrt{\pi}\Delta\omega_D} e^{-\left(\frac{\omega - \omega_{nm}}{\Delta\omega_D}\right)^2}, \quad (3.17)$$

where the FWHM of the Doppler broadened spectral peak is $\Delta\omega_D$. Obviously, Doppler broadening is dependent upon local variations in temperature and pressure just as collisional broadening is under conditions in which where both of the line-broadening effects contribute to the line-shape function, a so called Voigt profile develops [30].

3.3 Laser induced energy transfer effects

Whereas homogeneous broadening is best described by use of semi-classical model, energy transfer processes are better described by use of classical rate equations. Still the discrete energy levels result from quantum mechanics, although coherence is not included here. In the previous sections, absorption was described with use of the absorption cross-section derived from the expectation value of the transition dipole moment (Equation 3.15). In terms of the rate-equation formalism, the absorption that results in a transition from state n to state m is commonly described by use of the coefficient $B_{n,m}$, defined as

$$W_{nm} \equiv \frac{B_{nm}}{c} \int_{\omega} I(\omega)g(\omega)d\omega, \quad (3.18)$$

where W_{nm} is the transition rate. The integration is performed in the frequency domain, providing an account of the spectral overlap between the laser, $I(\omega)$, and the spectral line shape, $g(\omega)$. The left-hand side of Equation 3.7 is the loss in irradiance that occurs as the laser travels the distance dy within the probe volume. This can also be expressed as the product of the number density of the molecules, the transition probability and the energy of for each absorbed photon. Introducing this change on the right-hand side of Equation 3.7 and integrating over the angular frequency allows the transition rate to be expressed in terms of the absorption cross-section.

$$W_{nm} = \frac{\sigma_0}{\hbar\omega_{nm}} \int_{\omega} I(\omega)g(\omega)d\omega, \quad (3.19)$$

which then allows the relationship between the absorption cross-section and B to be determined as

$$B_{ij} = \frac{c}{\hbar\omega} \sigma_0. \quad (3.20)$$

In the energy-level diagram shown in Figure 3.2, the absorption process there under the B constant, starts at state a_m and terminates at a_n ($v = 1, j = 3$). Redistributions between rotational and vibrational states, termed rotational/vibrational energy transfer, are rapid [31] compared to spontaneous emission which is slow [30]. A radiation-free de-excitation channel is that of collisional quenching, Q , which involves, the excited molecule being de-excited through energy transferred to a colliding partner molecule.

There are several other possible energy transfer processes as well, though not shown in Figure 3.2, such as ionization, dissociation and chemical reaction. The population flow in and out of each molecular state is described by means of a rate equation. The rate equation of the excited state ($a_n(v = 1, j = 3)$) at which the laser pumping is directed can be described as

$$\begin{aligned} \frac{d}{dt} (N_{n(1,3)}(t)) = & \left(\begin{array}{l} W_{m \rightarrow n(1,3)} N_m(t) \\ + \sum_{j \neq 3} E_{n(1,j) \rightarrow n(1,3)}^R N_{n(1,j)}(t) \\ + \sum_{v \neq 1} E_{n(v,3) \rightarrow n(1,3)}^V N_{n(v,3)}(t) \end{array} \right) \\ - N_{n(1,3)}(t) & \left(\begin{array}{l} W_{n(1,3) \rightarrow m} \\ + \sum_{j,v} (A_{n(1,3) \rightarrow k(v,j)} + Q_{n(1,3) \rightarrow k(v,j)}) \\ + \sum_{j \neq 3} E_{n(1,3) \rightarrow n(1,j)}^R \\ + \sum_{v \neq 1} E_{n(1,3) \rightarrow n(v,3)}^V \end{array} \right). \end{aligned} \quad (3.21)$$

The top parentheses includes source terms of the states; of absorption and rotational and vibrational energy transfer. The second parentheses contains the sink terms: stimulated and spontaneous emission, collisional quenching and rotational and vibrational energy transfers.

3.3.1 Population distribution

As can be seen in Equation 3.21, the number of molecules that can be pumped from the ground state to the excited states is dependent upon the fraction of the molecules that are in the ground state at the time of excitation. Molecules perturbed by the electromagnetic field are in thermal equilibrium prior to excitation. Thus, the population distribution for the lower state can be calculated using the Maxwell-Boltzmann distribution [32].

$$N_m(t < 0) = N_{tot} \frac{e^{-\frac{E_m}{k_B T}}}{e^{-\frac{E_m}{k_B T}} + \sum_{v,j} e^{-\frac{E_{k(v,j)}}{k_B T}}}. \quad (3.22)$$

The fraction of molecules in state a_m is proportional to the Boltzmann distribution, $e^{-E_m/k_B T}$. In theory, all states should be considered as normalizing the Boltzmann factor and as providing the number density. However, it is often sufficient to include only the energy levels at the lower electronic states in the denominator. Thus, in order to calculate the number density of the molecules in state a_m , the energy structure of the lower electronic state and the temperature in the probe volume need to be determined.

3.3.2 Collisional Quenching

For a fully described system of coupled differential equations for all of the states, the fluorescence signal can be calculated as

$$I_{LIF}(t) = \sum_{v',j'} N_{n(j',v')}(t) \sum_{v,j} A_{n(v',j') \rightarrow k(v,j)}. \quad (3.23)$$

This equation summarizes all the spontaneous emission that occurs between the excited states ($a_{n(v,j)}$) and the lower states ($a_{k(v,j)}$). There are also radiation free energy transfer channels from the excited electronic state to the ground state, however. The most commonly discussed radiation free energy transfer process that has an impact on quantitative fluorescence data is collisional quenching, Q . Collisional quenching is strongly dependent on temperature and on the ambient collisional partner molecules. Since rotational energy transfer processes are quite rapid, the quenching rate can be considered as an average rate for all the states, from the excited states to the ground states [33]. In principle, this means that the rather complex energy diagram shown in Figure 3.2 is reduced to being a two-level model. In such a system, the average quenching rate can be calculated by summing the product of the species-specific quenching rate coefficient, k_{Qi} , and the number density of species N_i .

$$Q = \sum_i k_{Qi} N_i. \quad (3.24)$$

The relative average thermal collision velocity of the colliding species ($\langle v \rangle$) affects the quenching. Accordingly, the quenching rate coefficient can be expressed as

$$k_{Qi} = \sigma_{Qi} \langle v_i \rangle, \quad (3.25)$$

where σ_{Qi} is the quenching cross-section. Hence, the quenching rate coefficient is dependent upon the reduced mass of the colliding molecules, μ_i , and the temperature

$$\langle v_i \rangle = \sqrt{\frac{8k_B T}{\pi \mu_i}}. \quad (3.26)$$

Due to the quenching, only a fraction of the excited molecules contribute to the fluorescence signal by means of spontaneous emission. If an imaged probe volume shows local variations in temperature and in concentrations of the quencher species, the PLIF image does not provide a true image of the concentration. The fraction of the excited molecules that is fluorescing is termed the fluorescence quantum yield. In the two-level system as defined, the fluorescence quantum yield is written as

$$\Phi = \frac{A_{nk}}{A_{nk} + Q_{nk}}. \quad (3.27)$$

Here, A_{nk} is the Einstein coefficient for spontaneous emission and Q_{nk} is the total quenching rate. The sink terms in Equation 3.21 can be studied using a short pulse laser provided the fluorescence signal is studied after the excitation pulse has left the measurement volume. By considering the excited and the ground states as effective energy levels in a two-level system, Equation 3.21 is reduced to

$$\frac{d}{dt}(N_{\bar{n}}(t)) = -N_{\bar{n}}(t)(A_{\bar{n} \rightarrow \bar{k}} + Q_{\bar{n} \rightarrow \bar{k}}), \quad (3.28)$$

and the fluorescence signal given in Equation 3.23 can be written as

$$I_{LIF}(t) = N_{\bar{n}}(t)A_{\bar{n} \rightarrow \bar{k}}. \quad (3.29)$$

The solution to the simple differential Equation 3.28 is a single exponential function having a decay constant of

$$\tau = (A_{\bar{n} \rightarrow \bar{k}} + Q_{\bar{n} \rightarrow \bar{k}})^{-1}. \quad (3.30)$$

The latter means, if $A_{\bar{n} \rightarrow \bar{k}}$ is known, that a short pulse laser can be used for measuring the effective fluorescence quantum yield, by determining the decay rate of the fluorescence signal. It should be pointed out that for some molecules, under certain conditions, the decay curve is not single exponential. The reason for this is that the rates of the de-excitation processes differ from one to another, which results in multi-exponential decays.

3.4 Fluorescence signal

Although the full-rate equation model is needed to describe the fluorescence signal completely, the two-level illustrates the facts that there are components that can be compensated for rather easily if information concerning the temperature and the concentration of colliding species is available. If the two-level rate equation system is solved in time, the fluorescence signal can be expressed as

$$I_{LIF}(t) = N_n(t)A_{nm}. \quad (3.31)$$

Although such an approach usually suffices, it should be pointed out that multi-exponential decays can be understood by modeling with use of a three-level system. The total signal from a three-level system is the sum of the spontaneous emission from levels $|2\rangle$ and $|3\rangle$. The resulting fluorescence signal from such a simulation is shown in Figure 3.5, in which the multi exponential decays can be seen. A multi exponential decay is caused by the difference in transfer rates between the ground state and level $|2\rangle$ vs $|3\rangle$, as well the energy-transfer processes between levels that are excited.

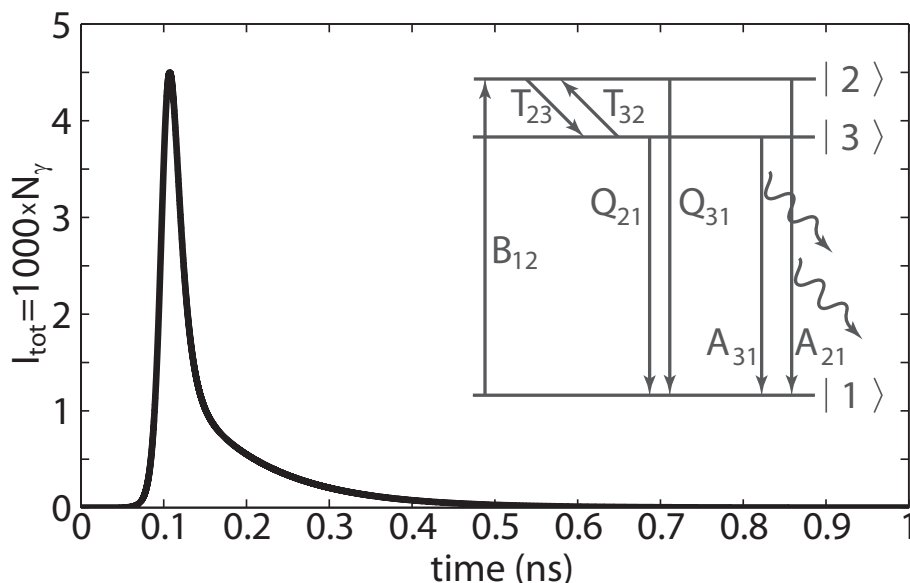


Figure 3.5: *The simulated fluorescence signals from a three-level system. The signals are multi exponential, due to differences in quenching rates between the two states. For the signals studied here, those that were evaluated are very close to being single exponential.*

ICCD cameras can be used to study the fluorescence signal, showing the signal to be integrated in the temporal domain. Such signal detection can in some cases be estimated by use of a box-car integration. If one assumes that the laser pumping is in the linear regime, meaning that the stimulated emission is negligible, molecules are excited by the laser, a fraction of the excited molecules emitting light through spontaneous emission. The fluorescence-signal power here can be expressed as

$$I_{LIF} = \hbar\omega C_{exp} B_{mn} N_n^0 f(T) \frac{A_{nm}}{A_{nm} + Q_{nm}(T, N_c)} \int_{\omega} \frac{I(\omega)}{c} g(\omega, T, N_c) d\omega. \quad (3.32)$$

The experimental collection efficiency involving the detector quantum efficiency, the filter functions and the collection angle, for example, is included in C_{exp} . The number density is denoted as N_n^0 its being weighted by the Boltzmann fraction, $f(T)$. The fraction that involves the Einstein coefficient, A_{nm} , is the fluorescence quantum yield and the integral, is the overlap function. The variable N_c is the number density of the quencher molecules. Quantitative data of fairly high accuracy can be obtained using this simplified expression of the fluorescence signals that are found. For example, formaldehyde PLIF images can be corrected for local differences in fluores-

cence quantum yield as well as for local variations in population distributions on this basis, as taken up further in Chapter 7.

3.5 Scattering processes

The scattering processes involved having molecular specific cross-sections similar to the absorption cross-sections used for excitation of different electronic levels, as described above. The vibrational and the rotational dipole moments can be separated in terms, a permanent and an induced dipole moment, where the induced dipole moment can be written as the product of the polarizability, $\tilde{\alpha}$, and the perturbing electric field. Since the molecular structure is rotationally invariant, the polarizability can be described by use of a 3x3 tensor. The polarizability is a factor that couples two molecular states involved in the scattering process. It can thus be written as

$$\vec{\mu}_i = \langle a_n | \tilde{\alpha}_i | a_m \rangle \cdot \vec{E}. \quad (3.33)$$

Since the work presented in the thesis considers vibrational states, the induced dipole moment is expressed as a Taylor series of the intermolecular distance Q_k between the atoms in the molecule.

$$\vec{\alpha}(Q_k) = \vec{\alpha}(0) + \sum_k \frac{\partial \vec{\alpha}}{\partial Q_k} \Big|_0 Q_k + \dots \quad (3.34)$$

Inserting Equation 3.33 into 3.34 yields

$$\vec{\mu}_i = \langle a_n | \vec{\alpha}(0) | a_m \rangle \cdot \vec{E} + \langle a_n | \sum_k \frac{\partial \vec{\alpha}}{\partial Q_k} \Big|_0 Q_k | a_m \rangle \cdot \vec{E} + \dots \quad (3.35)$$

The first term here is the induced dipole moment associated with elastic scattering, its thus not including a transition between different molecular states. Accordingly, the energy of the photon that scatters off the molecule has the same energy. Such scattering termed Rayleigh scattering, can be utilized, for example, for temperature measurements in combustion studies if the Rayleigh cross-sections of the scattering molecules are known. In such an approach, the dependence of the temperature on the number density is used for determining the temperature in the measurement volume. A ratio of two images is formed, the one image being of known temperature.

$$T_0 = \frac{I_0(x, y) \sigma_1^{Ray}}{I_1(x, y) \sigma_0^{Ray}} T_1. \quad (3.36)$$

Here, T , $I(x, y)$ and σ^{Ray} are the temperature, the image data and the Rayleigh cross-section, respectively, associated with the two images. Rayleigh

cross-sections for a number of combustion-related molecules are listed in [34]. The second term in Equation 3.35 involves the inter atomic distance which makes the scattering process inelastic, since it introduces coupling terms between different states. This means that the energy of the photon that is scattered off the molecule is shifted. Accordingly, a Raman scattering term is employed, this differing from the Rayleigh signal, since it includes species-specific information, and involves energy transfer within the molecule. Either the scattered photon gain energy in the process or energy is transferred to the molecules in question. If the energy of the photons is decreased, the conventionally used term assumes the photon to be Stokes shifted, and if the scattered photon has increased in energy, it is said to be anti-Stokes shifted.

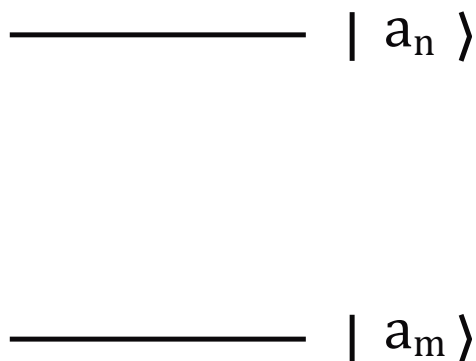


Figure 3.6: *Two-level molecule with state $|a_m\rangle$ and $|a_n\rangle$ that are separated by ΔE .*

Since Raman signals stem from a scattering process, they possess favorable features for use as a species-specific laser diagnostic tool. In contrast to fluorescence signals, Raman signals have a linewidth, but since a scattering process is involved, no absorption occurs, there thus being no overlap function to consider in the process. Also, Raman scattering is quenching-independent, since no resonant transition occurs, which means in principle that any laser wavelength can be used. At the same time, the Raman spectrum is affected by the temperature-dependent Boltzmann distribution. A simplified molecule having only two energy states; $|a_m\rangle$ and $|a_n\rangle$, the energy difference ΔE being considered, is shown in Figure 3.6. Since the induced dipole moment of Raman scattering results in an energy transfer process within the molecule, molecules that are in state $|a_m\rangle$ have to change state to $|a_n\rangle$ and vice versa. Thus, the signal strength ratio of the Stokes to the

anti-Stokes components contains temperature information:

$$T = \frac{\Delta E}{k_B \ln\left(\frac{I_S}{I_A}\right)}. \quad (3.37)$$

The Stokes and the anti-Stokes Raman peak intensities are denoted as I_S and I_A , respectively. Unfortunately, the Raman process is very weak: the cross-section of the Raman scattering for molecular nitrogen, for example, is about three orders of magnitude lower than the Rayleigh scattering for it [30]. Therefore rather high laser powers are needed, in combination averaged acquisition, especially in case of gas-phase measurements. A spectrally and temporally resolved Raman signal of nitromethane is shown in Figure 3.7, accompanied by an interfering fluorescence signal from Rhodamine 590. The difference in temporal characteristics between the Raman and fluorescence signals not only reveals different features of the signals, but it can also be used to distinguish the two signals. Such a scheme, presented in Paper VIII, can be utilized for laser studies in chemistry and medicine, as well as in physics.

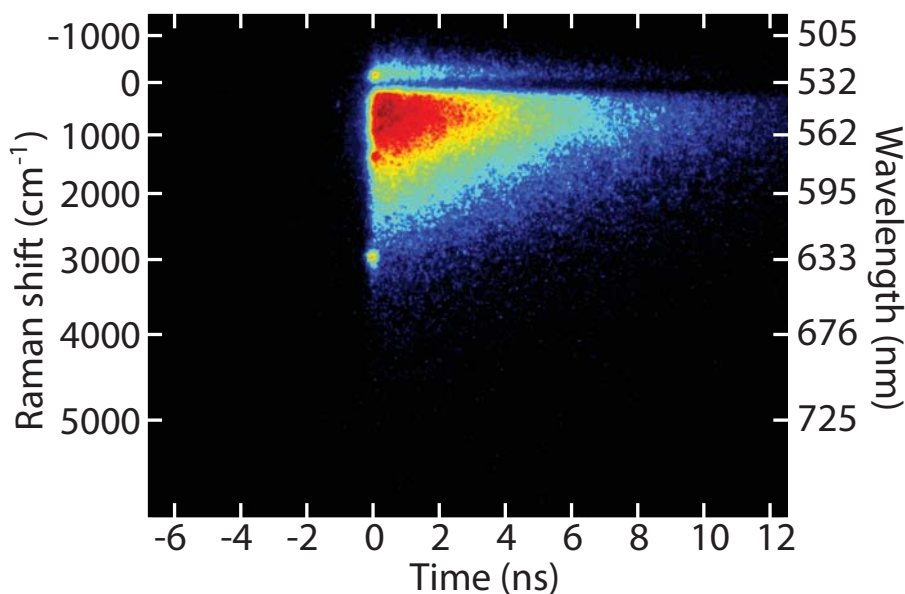


Figure 3.7: Temporally as well as spectrally resolved Stokes shifted Raman signatures of nitromethane together with fluorescence from Rhodamine 590. A streak camera having a spectrometer was used to resolve the signals in the two domains, the excitation being performed by a picosecond laser.

Chapter 4

Experimental Equipment

THIS is a brief overview of the equipment used in conduct the experimental work presented in the thesis. Emphasis has been placed on describing the parts of the equipment that had a major influence on the results and that also had a significant impact on development of the work carried out.

4.1 Lasers

Basically, a laser consists of two highly reflective mirrors (M_1 and M_2) that form a cavity, as can be seen in Figure 4.1a. One of these mirrors is of slightly lower reflectance than the other, the light exiting the cavity through this less reflective mirror. An active medium, found between the two mirrors. In some lasers it is pumped by flash lamps so as to excite the active medium. For an active medium in a laser cavity there need to be balanced transition rates between the energy levels involved. Ideally, for four level lasers, such as Nd:YAG lasers (shown in Figure 4.1b), absorption transfers molecules from the ground state, A, to an upper state, B. Since, the transition rate from state B to a lower state (C) is rapid (W_{CB}), which makes state B readily depleted, stimulated emission from state B to state A is very improbable. Also, since the transition rate from state C to a lower state D, (W_{DC}), is much slower than the transition rate (W_{CB}), a population inversion between state C and state D develops. However, if the transition from state C and D is stimulated level C is emptied and the photons in the cavity all have the same energy and are in phase, which is characteristic of laser light. The final transition from state D to the state A is also very rapid. Such a simplified transition scheme is shown in Figure 4.1b.

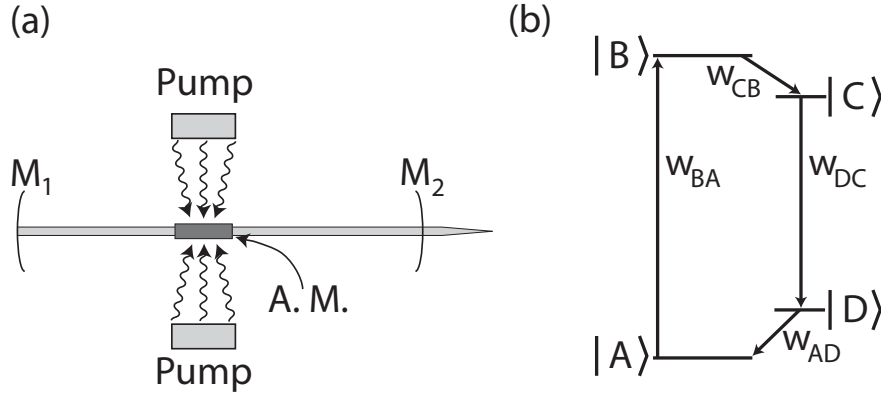


Figure 4.1: (a) A schematic image of the building blocks of a laser, where M_1 and M_2 are cavity mirrors and A.M. is an active medium which is pumped by flash lamps. (b) A simplified view of the energy diagram in a 4-level laser. The spontaneous transition rates W_{CB} and W_{AD} are much faster than W_{DC} results in a population inversion of states $|D\rangle$ and $|C\rangle$.

The work presented in the thesis was carried out with use of Nd:YAG lasers. The active medium was a $Y_3Al_5O_{12}$ crystal in which about 1% of the Y^{3+} ions were replaced by Nd^{3+} ions. A standard pulsed Nd:YAG laser used in combustion-related research is pumped by flash lamps, the Nd^{3+} -ions absorbing 0.7-0.8 μm light. This absorption corresponds to the BA transition shown in Figure 4.1b, whereas the CD-transition corresponds to a wavelength of about 1064 nm. Note that the transition scheme shown in Figure 4.1b is a simplification of the molecular structure of the Nd^{3+} ions in the YAG crystal. For a more detailed picture, see the book "Principles of Lasers" by Svelto [35] for example.

4.1.1 Q-switched lasers

In order to obtain a single laser pulse from a pulsed Nd:YAG laser, a loss factor needs to be introduced into the cavity, one that can be switched on and off very rapidly. Without such a loss factor, stimulated emission would occur as soon as population inversion is established, leading to a photons traveling in of the cavity modes. Since the pulse duration of the flash lamps is much greater than the pulse duration of such a pulse, a pulse train would be formed. Thus, a Q-switch, which can consist of two Pockel cells and a glass plate oriented at the Brewster angle relative to the laser cavity, is introduced into the cavity. When the Pockel cells are switched on, a photon can never make a complete passage through the cavity, since it is prevented from doing so by the glass plate. Since no stimulated emission in the cavity

is brought about, a pronounced population inversion is built up. When the Pockel cell is turned off, stimulated emission occurs and the upper state ($|C\rangle$) is depleted. Since a typical laser pulse from a Q-switched Nd:YAG resonator has a pulse duration of about 5-10 ns, letting the pulse run through several amplification steps leads to the pulse energy at 1064 nm becoming as high as 2 J. Often such pulses are used to pump dye lasers after being frequency doubled through second harmonic generation (SHG).

4.1.2 Mode-locked lasers

To obtain laser pulses with pulse durations as short as tens of picoseconds, use is made of a scheme termed mode-locking. In order for mode-locking to occur, the emission by the active medium needs to be spectrally broad. For an Nd:YAG crystal, the spectral width of the emission at room temperature is about 4 cm^{-1} [35]. For light to match the laser cavity, the length of the cavity must be an integer number of wavelengths in order to fulfill the standing wave condition. Such matches, which are termed longitudinal modes, are fulfilled for a number of wavelengths. The frequency separation between these modes is

$$\Delta\nu = \frac{c}{2L}, \quad (4.1)$$

where c is the speed of light and L is the length of the cavity. If the emission of the active medium is spectrally broad, the spectral dispersion of the light in the laser cavity is a frequency comb for which the envelope is set by the emission spectrum of the active medium, as can be seen in Figure 4.2.

The superposition of these frequency components results in features that are of very short temporal duration. Also, if the phases of these components are locked with each other, well-separated peaks are displayed. Simulations were performed for random (red) as well as locked (blue) phases as shown in Figure 4.3. Two different schemes, called passive and active mode-locking, are used in mode-locked laser systems to lock the phases.

Most of the work presented in the thesis was conducted using a picosecond laser with a repetition rate of 10 Hz, enabling high-power pulses to be produced. Two different pulse durations, 30 and 80 ps, were created that are ideal for temporal studies in the order of hundreds of picoseconds. Note that the temporal resolution of the experiments was set not only by the pulse duration of the laser but also by the detector response. Different detectors that were used with high temporal resolution are listed in Section 4.2.

Active Mode-Locking

The scheme for active mode-locking that is implemented in the picosecond laser system involves use of an electro-optic modulator (EOM). An EOM is

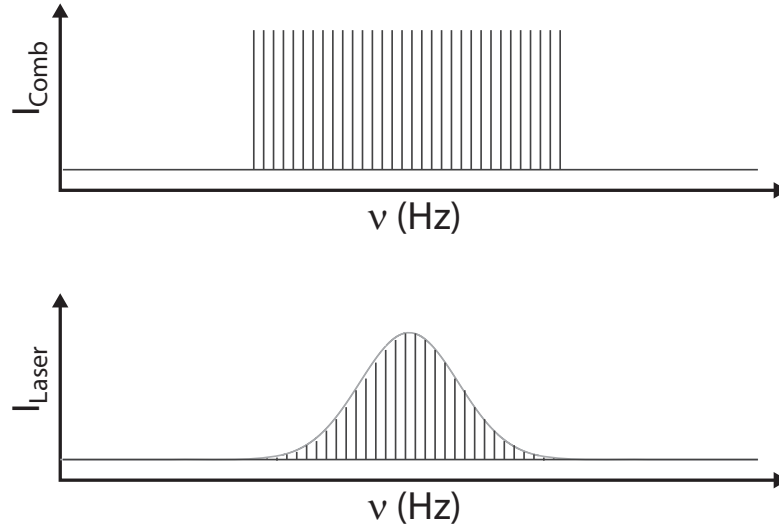


Figure 4.2: The upper image shows a frequency comb, every spike of which represents a frequency of a longitudinal mode within a laser cavity. The lower image shows the spectral shape of the emission in a laser cavity having longitudinal modes and an envelope function set by the frequency profile of the active medium.

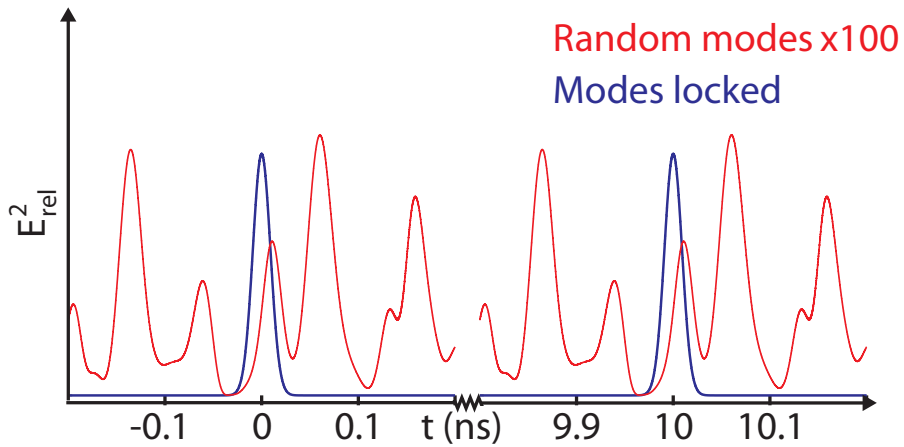


Figure 4.3: Simulated modes in a laser system similar to what was used in the experimental work presented in the thesis. The cavity length(L) is 1.5 m, the spectral width of the gain medium (ν_{FWHM}) is about 1 cm^{-1} and the wavelength is 1064 nm. The blue curve corresponds to the intensity related mode-locked laser pulse train, whereas the red curve describes the result for random modes. Note that the intensity of the red curve has been multiplied by a factor of 100. The temporal duration of the simulated laser pulse is roughly 20 ps.

basically a device having signal-controlled optical transmission. When an EOM is used in an amplitude-modulated active model-locking mode, the

driver signal is periodic. The periodicity of the electric driver signal of the EOM is matched to the time required for a round trip through the cavity. This matching enables a burst of pulses to be enhanced in the pumped active medium.

Passive Mode-Locking

The laser of interest in the work reported here has a solid state nonlinear absorber which is placed directly in front of one of the cavity mirrors. The absorber is bleached (saturated) as a laser pulse in which a sufficiently high level of energy is absorbed. For a sufficiently intense pulse, the major fraction of the pulse is transmitted, whereas a smaller part of it is strongly reduced. After a few round trips through the cavity the stronger pulses have been amplified by considerably more than they have been reduced, the lower pulses having vanished. In order for the passive mode-locking to be as effective as possible, the relaxation time for the absorbing medium should ideally be on the order of the pulse duration, but in all cases not be longer than one round trip through the cavity.

4.1.3 Characterization of pulse duration and time jitter

The simplest way of characterizing the pulse duration of a laser is to monitor the laser pulse by use of a detector of sufficiently high temporal resolution. When the detector is triggered by a laser pulse, the effect of time jitter is canceled. Time jitter are statistical fluctuations of the time difference between the arrival of the laser pulse and of the trigger pulse to the detector. The effect of time jitter can also be canceled by using built-in software in the detectors or by performing single-shot measurements and accumulating the results after temporal correction by use auto correlation. The probability density function (PDF) of time jitter is measured by monitoring the laser pulse without use of the time jitter correction. The resulting profile is not the PDF of the time jitter alone, since it is convolved with the temporal shape of the laser pulse. Since both the laser pulse and the jitter distribution are close to Gaussian, the jitter can be derived, since the shape of the laser is known. Another way of measuring the time jitter would be to use the auto-correlation correction statistics to build up the time jitter PDF.

4.2 Detectors

As the laser interacts with matter contained in the probe volume, a signal response is scattered or emitted and can be investigated by use of various detectors. A brief account of three detector types that were used for zero-, one-, two- and up to three-dimensional measurements, in which time is the

third dimension, is presented below. These are all detectors that provide high temporal resolution, which is of the essence of short-pulse studies.

4.2.1 MCP-PMT

An MCP-PMT (Micro Channel Plate Photo Multiplier Tube) is a detector used for temporally resolved point measurements. By focusing the laser to a single point high spatial resolution is achieved. However, since the photo-sensitive area is rather large, there may be interest in performing measurements with use of a 2-dimensional laser sheet or even with the laser unfocused. The detector consists of two parts: the photo cathode (PC) and a multi-channel plate (MCP). A schematic diagram of the MCP-PMT is shown in Figure 4.4.

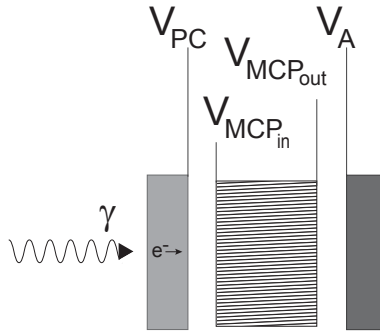


Figure 4.4: A block image of the MCP-PMT, which consists of a PC (left), MCP (middle) and an anode (right). The four voltages employed increase from left to right in order to accelerate the electrons. The difference in potential between the anode and ground is the final signal.

The PC is a metal plate coated with a photosensitive compound. Free photoelectrons are produced by the photoelectric effect produced as the photons impinge upon coating. These electrons are accelerated in an electric field between the PC and the MCP. The MCP consist of metal-coated capillaries that are cut in the form of a disk, an electric field further accelerating the electrons. As the photoelectrons generated at the PC enter the MCP, they collide with the metal walls wall, generating further electrons. Finally, the electrons are registered at the anode located behind the MCP, the voltage of the anode representing the output signal.

The thin MCP plate with its tiny channels provides higher temporal resolution than a conventional PMT in which the electron avalanche is created by use of a dynode chain. The MCP-PMT employed in the studies here had a signal-response function ($G(t)$) with a rise time of 150 ps, a fall time of 360 ps and a full width at half maximum (FWHM) of 300 ps. Evaluation

of the data acquired ($I_{det}(t)$) using such a detector should be carried out with the response function in mind, since the signal response detected is a convolution of the signal ($S(t)$) and the response function [25], such that

$$I_{det}(t) = G(t) \otimes S(t) \quad (4.2)$$

The MCP-PMT that was used in the studies was ideal for investigating signals with temporal features of around 1 ns and weak signal intensities, since the detector is very sensitive and it has a rapid signal response.

4.2.2 Streak Camera

A streak camera is a two-dimensional detector in the default mode, one of the dimensions involved being time. The other dimension can be spatial if measurements are conducted along a line, or be spectral if the streak camera is mounted on a spectrometer. If measurements are conducted along a line, a spherical lens with a long focal length can be employed to focus the laser beam. For spectroscopy, a point measurement is preferable. Note, however, that a streak camera can be used as a regular ICCD camera for two-dimensional imaging, if the streak unit is turned off. This non-streak mode of operation, frequently called focus mode, is often used to set the gain parameter properly and to optimize the focusing optics. A block scheme of a streak camera is shown in Figure 4.5.

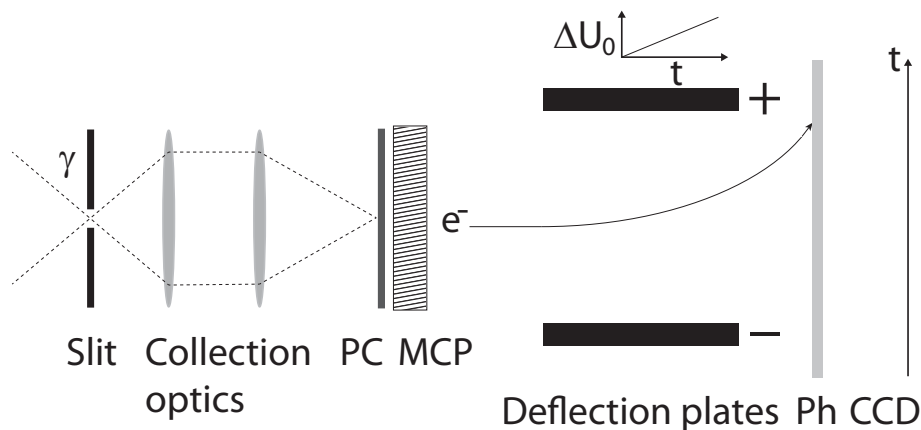


Figure 4.5: *The temporal resolution of a streak camera is primarily set by streak rate, but the width of the entrance slit also contributes to the overall temporal resolution.*

The photons captured by a streak camera enter the device through a slit. The temporal resolution of a streak camera can be controlled by the slit width. A wide slit allows more light to be detected but the temporal

resolution attained is limited. The slit is imaged on the photocathode/MCP-unit by use of built-in quartz collection optics. After the photoelectrons have been multiplied by the MCP, they enter the streak unit, where two deflection plates link the electron beam with a fast ramping voltage, ΔU_0 . When the streak unit is turned off (meaning that no voltage is applied across the deflection plates), the electrons image the slit at the phosphorous plate (Ph), the image being integrated then on the CCD chip. When the streak unit is turned on, the electrons that arrive early are deflected slightly, since the voltage is low, whereas the electrons that arrive later are deflected to a greater extent, allowing the arrival time of the electrons to be distinguished in one dimension. The deflection voltage can be ramped with different streak rates, so as to provide variation in the temporal resolution. However, a higher level of temporal resolution results in a smaller time window. The streak camera used in the thesis provided a temporal resolution of 2 ps and a streak rate of 10 ps/mm (the chip size is a little less than 2 cm). The slowest streak rate is 1 ns/mm, which provides a resolution of 200 ps and a time window of about 20 ns. A typical streak-camera image is shown in Figure 4.6.

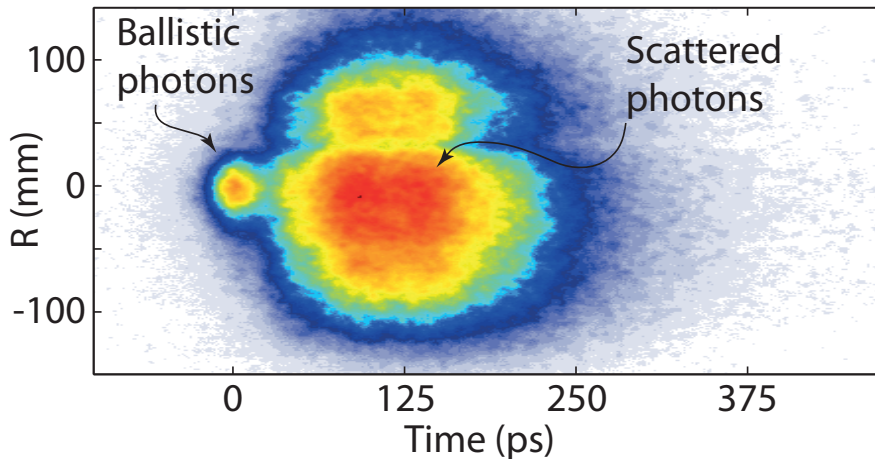


Figure 4.6: A streak camera image of an experiment in which photons are transmitted through a highly scattering medium. Photons that pass through the optically dense medium without being scattered are called ballistic photons. These photons arrive early and are well collimated, the multiple scattered photons arriving later and having lost their precise direction.

The vertical R-axis provides a spatial resolution along the slit, whereas the time axis appears in the figure as a horizontal line. The data acquired is from a transmission experiment through a dense scattering medium of water and polystyrene spheres. The signal arriving early are the ballistic photons that travel through the scattering solution without being scattered, whereas those arriving later has been multiply scattered. Also, since the

ballistic photons are not scattered, they retain the spatial shape of the laser pulse, whereas the scattered photons are diffuse in appearance, the spatial profile being broadened. A nice feature of a streak camera is that it does not have any response function such as that of the MCP-PMT, making it ideal for studies of phenomena in a temporal range close to that of the laser pulse duration. On the other hand, a streak camera is triggered by the laser and thus shows time jitter. There are jitter correction routines implemented in the software of the streak camera, which makes the PDF of the jitter function very narrow in temporal terms. The accumulated detection of the signal $S(t)$ using a streak camera can be described mathematically as

$$I_{det}(t) = J(t) \otimes S(t). \quad (4.3)$$

Here, $J(t)$ is the time jitter.

4.2.3 ICCD camera

An ICCD camera is a PC/MCP/P (photocathode/multi channel plate /phosphorous plate) intensifier unit mounted on a CCD camera. The building blocks of an ICCD camera are displayed in Figure 4.7. The obvious advantage of an ICCD camera, in comparison to a regular CCD camera, is the intensifier that opens up for the imaging of weakly irradiating objects. In addition, an ICCD camera is sensitive to light in the UV region. The downside of the intensifier is that its spatial resolution is very much reduced, since the capillary density of the MCP-surface is very small compared with the pixel density that can be manufactured for a CCD camera. Another feature that makes the ICCD camera attractive is that the camera can be gated, which means that the intensifier can be either open or shut. This feature is extremely attractive if a strong continuous background is present, such as flame luminescence. Thus, pulsed lasers in combination with gated ICCD cameras provide sensitive detection suitable for obtaining measurements in luminescent environments. In addition, ICCD cameras mounted on spectrometers provide the same advantages in spectroscopy, in which the one dimension provides spectral dispersion and the other spatial. A mathematical description of ICCD-camera detection of signal $S(t)$, using a gate function $G(t)$, with a time jitter $J(t)$ can be written as

$$I_{det}(t) = \int J(t) \otimes S(t) \cdot G(t) dt. \quad (4.4)$$

Measuring the gate characteristics

The most accurate registering of the temporal characteristics of a gate function can be obtained by performing accumulated picosecond Rayleigh measurements as the delay time of the camera is reduced. As described in Paper

4. EXPERIMENTAL EQUIPMENT

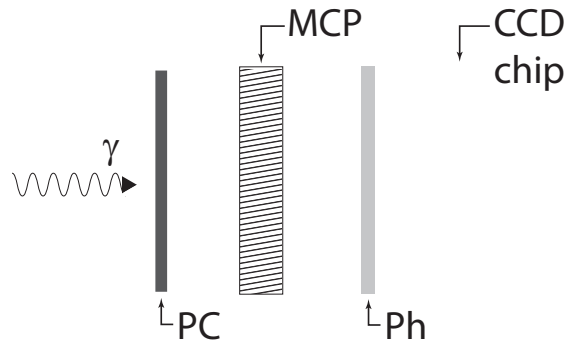


Figure 4.7: *The photons first hit the photo cathode, where photoelectrons are created through the photoelectric effect. These photons are accelerated to the MCP where the electronic signal is amplified. The electrons then hit the phosphorous plate, where photons are created, these being integrated on the CCD chip.*

I, the results do not indicate the shape of the gate function itself, but rather of the gate function convolved with the laser pulse and the PDF of the time jitter. Triggering the intensifier by use of only a fraction of the laser pulse intensity, allows the time jitter to be disregarded. The broadening effect on the gate function can be neglected in case of very short laser pulse duration and small time jitter. In principle, it would be possible to account for time jitter if single-shot measurements were performed and the jitter was logged by an additional detector. The gate function could then be reconstructed from the corrected single-shot data. If two cameras are to be compared, the wavelength dependence of the transmission and the relative quantum efficiency of the photocathode need to be determined for both cameras.

Chapter 5

Temporal Filtering

THIS chapter describes temporal filtering techniques used in fluorescence and Raman scattering studies. The approach of discriminating interfering signals in the temporal domain has been of increasing interest due to development of more robust pico- and femtosecond laser systems recently having a reasonable price range. Such developments result in better detection schemes for studies of linear signals, such as Raman scattering and fluorescence signals, and also in studies of non linear signals in which the high peak powers result in efficient multi-photon interaction processes. However, fast detectors are needed in order to utilize the temporal domain for the discrimination of interfering signals. The rapid development of fast gated ICCD cameras in recent years has made it possible to develop detection schemes utilizing the temporal domain for use in imaging studies.

5.1 Picosecond laser diagnostics

The basic idea of laser-based imaging is to illuminate the measurement object with a laser sheet and to detect the signal response with use of a detector. Pulsed laser imaging can be seen as analogous to photography, in which a short flash is synchronized to operation of the camera shutter so as to capture moving targets for which the naturally occurring light is insufficient. However, lasers have the advantages not possible to achieve in photography, since the laser beam is coherent, allowing it to be converted into focal points or into a laser sheet. The selective illumination of measurement objects under such conditions enables investigations of a cross-sectional nature to be carried out. The pulse duration sets the temporal resolution of the signal in a laser experiment. Traditionally, Q-switched, nanosecond lasers have been used in experimental work in applied science due to their robustness and high

pulse power and their reasonable price range. In addition, pulse widths of 5-20 ns are sufficient for capturing transient events, such as turbulence and, in combination with gated detection, enables continuous background luminescence to be discriminated effectively. However, nanosecond laser sources cannot resolve physical phenomena involving dynamics having very short time scales, such as collisionally induced energy transfer processes, such as quenching, rotational and vibration energy transfer and the like. Such phenomena are themselves of great interest to study in order to gain knowledge of energy transfer dynamics. It is also important to understand how these processes affect signals used for the determination of quantitative, or at least of qualitative, species concentrations. Simulations of laser-induced fluorescence signals are shown in Figure 5.1, to illustrate the difference between pico- and nanosecond excitation. Obviously, the 2 ns decay rate of the signal cannot be determined in a straight forward way when a 5 ns laser pulse is employed, as compared with when a 30 ps laser pulse is involved.

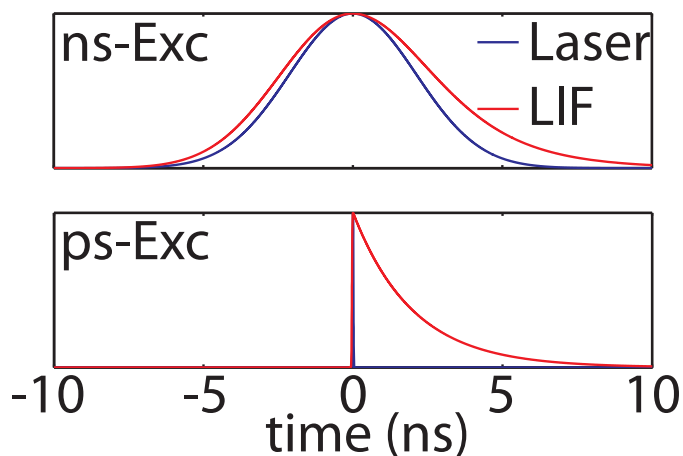


Figure 5.1: An illustration of pico- and nanosecond excitation. The fluorescence response function; a single exponential function with 2 ns decay is convolved with two Gaussian functions, representing laser pulses with different pulse widths. The full-width at half maximum (FWHM) of these functions are 5 ns (top) and 30 ps (bottom).

5.2 Temporal Filtering

The fundamental idea of a temporal filter is to use the different time characteristics of the signal that is studied and of the interfering signal so as to be able to discriminate the interference so as to capture adequately the signal that is of interest. Temporal filtering can be employed in fluorescence studies in which short lived interfering signals are present, achieving the result

desired by detecting simply the latter part of the signal. In the opposite situation, in which short-lived signals are of major interest, such as in the case of Raman signals, temporal filtering can be used to suppress any fluorescence that interferes through capturing only the early part of the signals. If point measurements provide sufficient information, a PMT, MCP-PMT or a fast photo diode can be used together with a short-pulse laser, in which the early part of the signal is cut out as the data is analyzed. Such an approach is also favorable in measurements obtained by use of a streak camera, which has the ability to spatially resolve data in one dimension (along a line) or, with a spectrometer attached to the streak camera, for spectroscopic investigations. A typical result of a streak-camera investigation is shown in Figure 5.2, in which the Raman signal of the CH-stretch from liquid N-decane is embedded in an interfering fluorescence spectrum. By integrating the temporally resolved spectrum, $S(t, \lambda)$ over the different time scales involved, as

$$I(\lambda) = \int_{t_0}^{t_i} S(t, \lambda) dt, \quad (5.1)$$

where $i = 1, 2, 3, 4$, the amounts of interfering fluorescence that are present when the Raman peak is detected is differing.

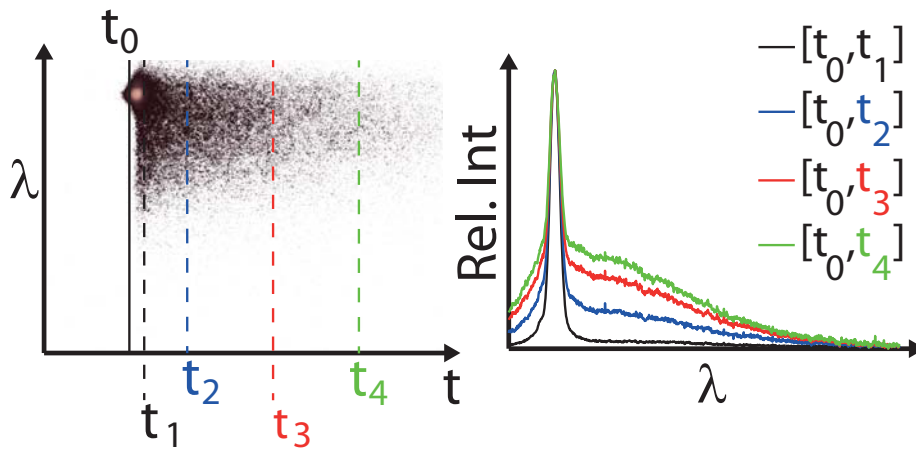


Figure 5.2: The picture at the left represents a spectrally and temporally resolved streak camera image of Raman measurement in the presence of interfering background fluorescence, obtained using 266 nm excitation. The image at the right shows a spectrum in which different time intervals have been integrated, in accordance with Equation 5.1. The initial value of the integration is t_0 , the final integration limits being $t_1 - t_4$, these values being marked on the time scale, in corresponding color, in the image at the left.

The temporal filtering is performed with the help of ICCD cameras, the filtering process taking place while the experiment is being conducted, the

temporal information being lost when the signal is recorded on the CCD chip. In the filtering, the ICCD-camera gate functions as a temporal filter, such that only photons that reach the photocathode as the voltage of the photo cathode is turned on are detected. Although modern ICCD cameras are equipped with fast electronic devices able to create gate functions having short rise and fall times, the gate has a certain well-defined shape. A typical gate function of an ICCD camera is shown in Figure 5.3 by the dashed black line there. The shape of the gate function can be simplified through describing the gate as being trapezoid in shape, as shown by the solid red curve in Figure 5.3, its agreeing reasonably well with the measured gate function. A mathematical description of such a camera gate function could be as follows:

$$G(t, \Delta_F) = G_0 \left(\begin{array}{l} \frac{1}{t_r}(t - \Delta_F)[\theta(t - \Delta_F) - \theta(t - \Delta_F - t_r)] \\ +[\theta(t - \Delta_F - t_r) - \theta(t - \Delta_F - t_r - t_t)] \\ -\frac{1}{t_f}(t - \Delta_F - t_r - t_t - t_f)[\theta(t - \Delta_F - t_r - t_t) \\ -\theta(t - \Delta_F - t_r - t_t - t_f)] \end{array} \right). \quad (5.2)$$

Here, t_r is the rise time, t_f the fall time and t_t the time spent at the maximum of the gate function, θ is the Heaviside step function and Δ_F is the gate delay time, i.e. the time between excitation and start of the gate function. Note that the gate delay time of the camera can be defined in various ways. Four different ways of defining it can be seen at the bottom of the time scale shown in Figure 5.3. In fluorescence studies, in which a rising edge is employed, either Δ_F or Δ'_F is appropriate to use as the gate delay. The falling edge of the gate function is employed in Raman studies, making it suitable to use either Δ_R or Δ'_R as the delay time. Primed values are set when the gate reaches 10 % of the maximum value. This is a convenient definition to use if account is taken for the experimentally determined gate function. In somewhat simplified terms, therefore, ICCD camera delay times can be related in any of the following ways:

$$\Delta_F = \Delta'_F - 0.1 \cdot \tau_r \quad (5.3)$$

$$\Delta_R = \Delta'_R + 0.1 \cdot \tau_f \quad (5.4)$$

$$\Delta_F = \Delta_R - t_r - t_t - t_f \quad (5.5)$$

$$\Delta'_F = \Delta'_R - 0.9t_r - t_t - 0.9t_f \quad (5.6)$$

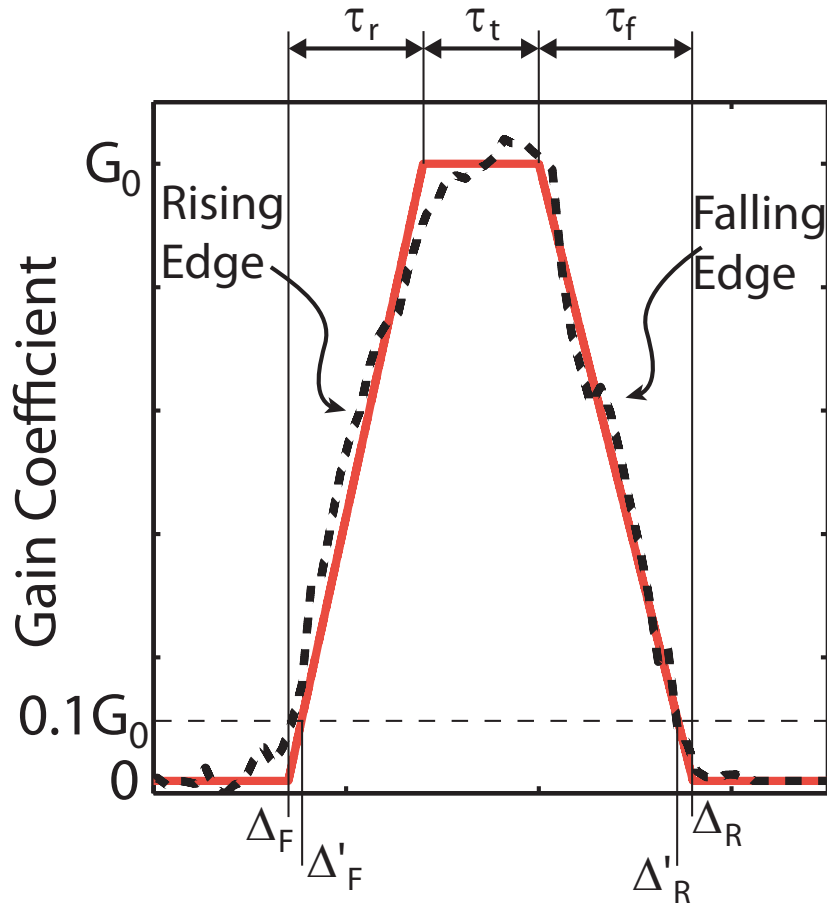


Figure 5.3: A measured ICCD camera gate function used for temporal filtering in the experimental work temporal filtering is shown by the black dashed curve. The red curve is a simplified ideal gate function used in the simulations and described by Equation 5.2. The four separate camera gate delays, in the excitation are shown at the bottom, Δ_R and Δ'_R being the delay times that are particularly convenient to use in Raman studies, since it is the falling edge of the gate function which is utilized there, whereas in fluorescence studies Δ_F and Δ'_F are more convenient to use. In making use of the real gate functions, the primed delays are more conventional to use, since the exact point in time when the gate starts or stops is difficult to define.

In Raman and in fluorescence studies, the gate function can be simplified still further through use of only the rising and falling edges. The effectiveness of the temporal filter is dependent upon the following:

1. The signals of interest (their intensity and duration), $S(x, y, t)$
2. The interfering signals (their intensity and duration), $P(x, y, t)$
3. The shape of the laser pulse, $L(t)$

4. The characteristics of the detector-gate function, $G(x, y, t)$
5. The jitter occurring between the laser pulse and the trigger pulse of the laser, δ . The statistics of this variable can be described in terms of the probability density function $J(t)$, which can be assumed to have a Gaussian distribution.
6. The delay time of the camera gate function, Δ_i .

Two parameters tend to be of primary interest in describing a filter. One of them is the fraction of the signal in question which is detected. In case of spectral filtering this is termed the degree of transmission, T . In mathematical terms T can be defined as

$$T(x, y, t) = \frac{I_{TF}^S(x, y, t)}{I_{Ref}^S(x, y, t)} \quad (5.7)$$

where I_{TF}^S is the intensity of the signal in question when temporal filtering is employed, and I_{Ref}^S is the intensity of the signal when no temporal filtering is carried out. The other parameter of interest is the fraction of the detected signal which is of interest. This parameter is called the signal-to-signal and interference ratio $SSIR$, being defined as

$$SSIR(x, y, t) = \frac{I_{TF}^S(x, y, t)}{I_{TF}^S(x, y, t) + I_{TF}^I(x, y, t)} \quad (5.8)$$

where I_{TF}^I is the intensity of the interfering signal when it is temporally filtered. The intensity that is detected in a pixel, (x, y) , in averaged measurement of it can be expressed mathematically as

$$I_{acc.}(x, y) = N_{acc.} \int_{-\infty}^{\infty} S(x, y, t)[G \otimes J](x, y, t - \Delta_i) dt \quad (5.9)$$

Since the photoelectrons are gated and are amplified by the intensifier the signal, $S(x, y, t)$, is multiplied by the gate function, $G(x, y, t)$. The timing of the gate function is dependent upon the delay of the camera, Δ_i and the time jitter, δ . The statistics of the time jitter are described by the probability density function $J(t)$. When several images of different time delay due to the time jitter the original level of detection is smeared out. This smearing effect can be described as representing a convolution involving the probability density function of the time jitter and the gate function of the detector. Note that not only the signal but also the gate function is dependent upon the physical location on the intensifier that corresponds to the pixel (x, y) values in question. The effect this brings out is termed irising. It takes place because of the voltage pulse that controls the intensifier gate

function propagating from the edges of the photo cathode to the center of it, the outer part of the intensifier thus being turned on and turned off earlier than the central part is.

In the two sections that follows, results of temporal filtering in fluorescence studies and Raman studies that were carried out, involving use of ICCD cameras, are presented and discussed. Note that a temporal filter can be combined with virtually any other type of filtering techniques available. One drawback in the use of mode-locked ultra short laser pulses, however, is that the spectral profile of the laser pulse produced tends to be relatively broad. Since, as mentioned in Chapter 4, the time duration and the spectral profile of the laser pulse are linked in case of mode-locked laser systems, there are limitations there in terms of single line excitation, or in the ability tuning on and off spectral lines in order to suppress interferences having broad emission and absorption. On the other hand, temporal filtering techniques can be performed in connection with single-shot measurements, or in combination with other background subtraction schemes, so as to maximize use of the dynamic range of the detector.

5.2.1 Temporal Filtering in Fluorescence Measurements

The idea of temporal filtering as it is used in fluorescence studies to discriminate elastic scattering is presented schematically in Figure 5.4. The scheme described there utilizes the different temporal characteristics of the interfering radiation and the signal of interest. In such measurement situations in which the interference is due to scattering, which essentially is an instantaneous process, the signal of interest being that of fluorescence, the fluorescence in question, which has a finite lifetime, can only be distinguished from scattering if it is only the decay tail of the fluorescence that is recorded. As indicated above, excitation needs to be performed there with use of a laser pulse of significantly shorter duration than the fluorescence lifetime, and the signal must be detected with high temporal resolution. For this reason, picosecond excitation along with use of ICCD cameras having a camera-gate function possessing a rise time shorter than the fluorescence lifetime are ideal for temporal filtering in two dimensions.

The efficiency of a temporal filter by use of a particular laser and ICCD camera can be calculated for a given set of signals, by use of the entire expression contained in Equation 5.9. Somewhat simplified analytical expressions can be obtained, however, through the time jitter and the laser pulse duration being neglected, and the ICCD camera gate being considered to have a trapezoidal shaped function, together with a linearly increasing rising edge having a rise time of t_r . A mathematical description of the rising

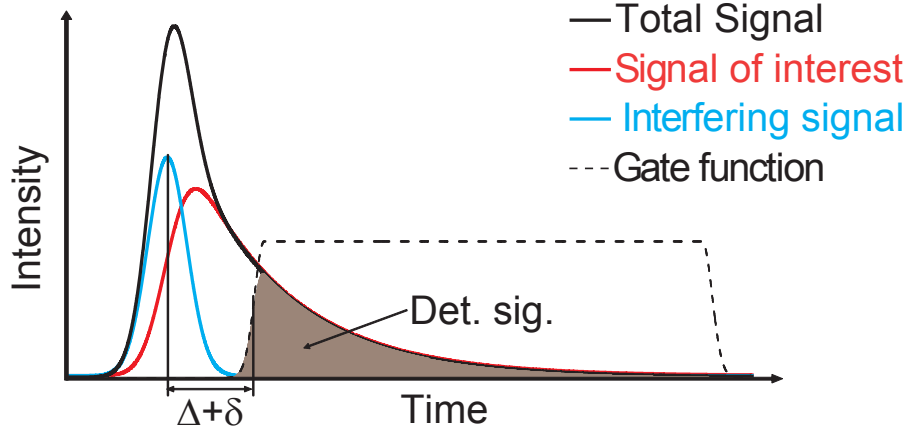


Figure 5.4: A graphic presentation of temporal filtering as performed in an LIF measurement in which elastic scattering is suppressed. The gate function of the ICCD camera is delayed in order to detect only the decay tail of the fluorescence signal. The gray marked area is the integrated signal that is detected.

edge of the camera gate function could be formulated as follows:

$$G(t, \Delta_F) = G_0 \begin{pmatrix} \frac{1}{t_r}(t - \Delta_F)[\theta(t - \Delta_F) \\ -\theta(t - \Delta_F - t_r)] \\ +\theta(t - \Delta_F - t_r), \end{pmatrix} \quad (5.10)$$

where G_0 is a constant and details concerning the level of detection are included, such as its quantum efficiency, for example. The signal $S(x, y, t)$ can be detected with use of such a camera-gate function, its being possible to calculate $I(x, y, \Delta_F)$ as

$$I(x, y, \Delta_F) = G_0 \begin{pmatrix} \frac{1}{t_r} \int_{\Delta_F}^{\Delta_F+t_r} tS(t, x, y)dt \\ -\frac{\Delta_F}{t_r} \int_{\Delta_F}^{\Delta_F+t_r} S(t, x, y)dt \\ + \int_{\Delta_F+t_r}^{\infty} S(t, x, y)dt, \end{pmatrix} \quad (5.11)$$

Ideally, fluorescence signals can be considered as representing single-exponential functions, such as

$$S_i(x, y, t) = S_i^0 e^{-\frac{t}{\tau_i}} \theta(t). \quad (5.12)$$

The detected signal can be calculated for cases of three types, depending upon the length of the delay. If the camera gate function is delayed so much that it is turned on after excitation has taken place, i.e. $\Delta_F > 0$, the strength of the fluorescence signal that is detected can be calculated as

$$I_i(x, y, \Delta_F)|_{\Delta_F > 0} = \frac{G_0 \tau_i^2 S_i^0}{t_r} e^{-\frac{\Delta_F}{\tau_i}} \left(1 - e^{-\frac{t_r}{\tau_i}}\right) \quad (5.13)$$

If the gate is delayed so long that excitation occurs as the ICCD camera gate function is rising, i.e. $-t_r < \Delta_F < 0$, the signal can be calculated as

$$I_i(x, y, \Delta_F)|_{-t_r < \Delta_F < 0} = \frac{G_0 \tau_i S_i^0}{t_r} \left(\tau \left(1 - e^{-\frac{\Delta_F + t_r}{\tau_i}} \right) - \Delta_F \right) \quad (5.14)$$

Finally, for $\Delta_F < -t_r$, which basically means that temporal filtering is not performed, and that only the last term in Equation 5.11 is non-zero, the lower integration boundary is set to zero. Here the expression that applies is

$$I_i(x, y, \Delta_F)|_{\Delta_F < -t_r} = G_0 S_0 \tau \quad (5.15)$$

Regarding the assumptions made in deriving the analytical equations just referred to, it is recommended that Equation 5.14 be used with caution, since the shape of the laser pulse, the time jitter, and the current shape of the rising edge of the fluorescence signals plays a stronger role in that interval. In addition, in order to suppress the short-lived fluorescence as much as possible, the camera-delay time should be as long as possible, provided the signal level of the detected signal of interest is acceptable, its being thus assumed that the ICCD camera gate delay is greater than zero, which means that when the camera gate is turned on it only collects the tails of the fluorescence signals. Such a situation is illustrated in Figure 5.5, in which

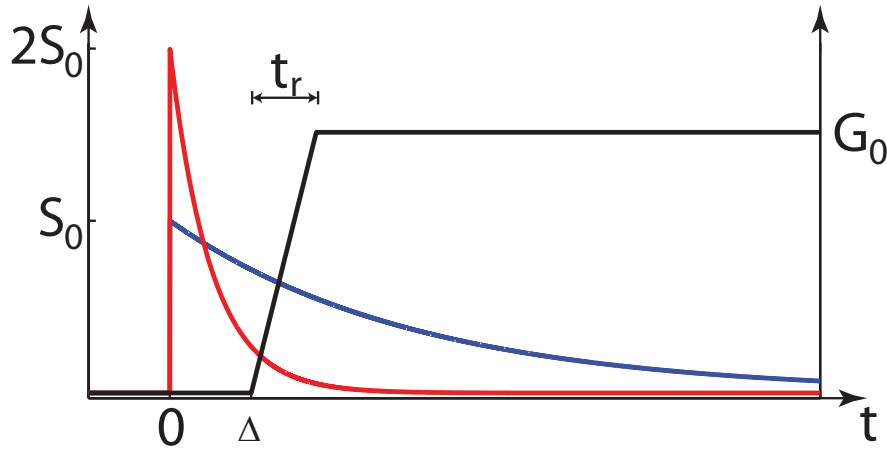


Figure 5.5: A simple sketch of the two LIF signals and of the ICCD camera gate function. The red and the blue curves are the interference signal and the signal of interest, respectively. The lifetime of this latter signal is six times as long as the lifetime of the interference signal, whereas the initial intensity of the signal of interest is half the value of the corresponding interference signal. The black curve represents the ICCD camera gate function, which is delayed Δ_F and has a rise time of t_r . When the delay lies within this range, the detection of the two LIF signals can be described satisfactorily by Equation 5.13.

two fluorescence signals of differing time characteristics are displayed. Here, $S_1(t, x, y)$ is the signal of interest and $S_2(t, x, y)$ is the interfering signal. In such a measurement situation, the parameter T can be expressed as

$$T(x, y, \Delta_F) = \frac{\tau_1}{t_r} e^{-\frac{\Delta_F}{\tau_1}} (1 - e^{-\frac{t_r}{\tau_1}}) \quad (5.16)$$

and $SSIR$ would be

$$SSIR(x, y, \Delta_F) = \left[1 + \left(\frac{\tau_2}{\tau_1} \right)^2 \frac{S_2^0}{S_1^0} e^{-\Delta_F \left(\frac{1}{\tau_2} - \frac{1}{\tau_1} \right)} \frac{1 - e^{-\frac{t_r}{\tau_2}}}{1 - e^{-\frac{t_r}{\tau_1}}} \right]^{-1} \quad (5.17)$$

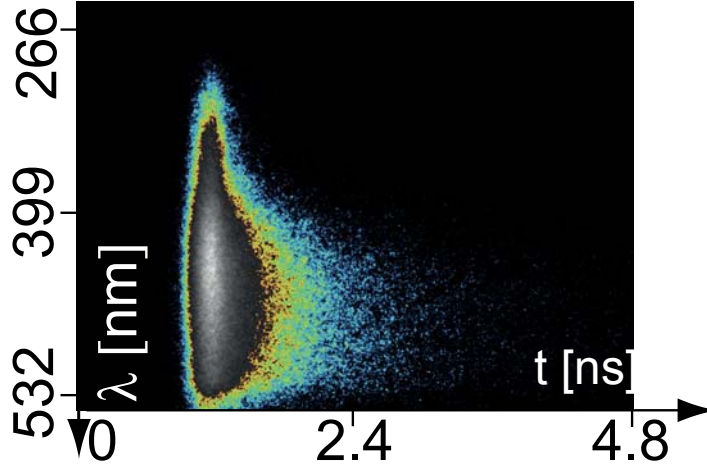


Figure 5.6: Temporally and spectrally resolved luminescence signals of a wooden pellet, using 266 nm excitation.

Laser-induced fluorescence carried out on different species in the pyrolysis of wooden pellets would be an example of temporal filtering performed in connection with fluorescence measurements. Pyrolysis is a form of thermochemical decomposition that takes place at elevated temperatures in the absence of oxygen. The lack of oxygen is ideal for temporal filtering since oxygen is an important collisional quenching partner, and since without the presence of ambient oxygen molecules the fluorescence lifetimes would be longer. Accordingly, the luminescence of a wooden pellet itself was investigated, both spectrally, and temporally, as shown in Figure 5.6. The luminescence signal covers a broad spectral range, 300-550 nm, the time duration of the signal being from a few hundred picoseconds up to a about two nanoseconds, depending on the wavelength. In studies of wood pyrolysis, conventional nanosecond laser excitation has been performed for a number of excitation wavelengths [36]. In that work, carried out by Brackmann et al., interfering fluorescence was not a major issue, possibly due to the fact

that the measurements were first performed after at least 80 seconds of pyrolysis of the wooden piece. By that time the luminescent constituents may well have been decomposed already, so that the fluorescence was reduced. Temporal filtering might thus be useful for studying the initial phase of pyrolysis, especially since the luminescent background changes over time, making background subtraction rather complicated. Even if a background subtraction scheme could be performed, employing a temporal filtering technique would make better use of the dynamic range of the detector.

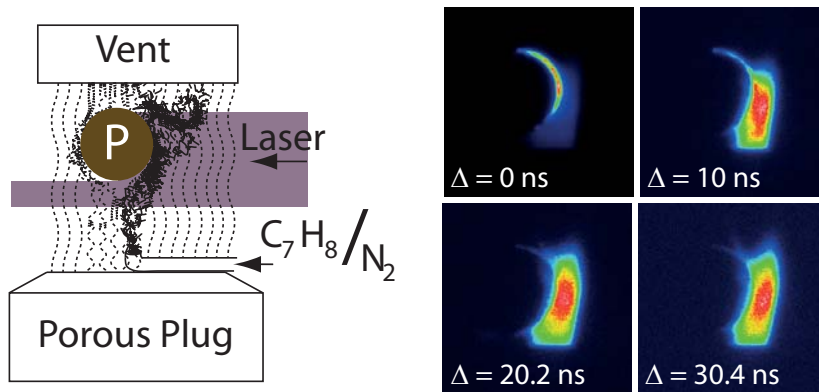


Figure 5.7: To the left, a schematic image of the measurement volume is displayed, where a porous plug ejects nitrogen in the measurement volume to shield off oxygen from the ambient air. In the middle of the porous plug, a vertically directed gas jet ejects toluene seeded nitrogen onto the wooden pellet. To the right, PLIF images are shown that was captured at different time delay. At delay times longer than 20 ns the pellet luminescent has died off, imaging only the toluene seeded gas.

To simulate such a study, a test experiment was performed involving the visualization of toluene-seeded nitrogen of a surface of a wooden pellet. The experimental volume is shown in Figure 5.7, where as can be seen the toluene-seeded gas jet is ejected onto the surface of the wooden pellet. The oxygen concentration was kept low by using nitrogen as the seeding gas and inserting a porous plug that ejected additional nitrogen into the measurement volume. PLIF images (the four panels at the right in Figure 5.7) showed that the initially dominant surface luminescence was substantially lower after about a 10 ns delay, this enabling images to be obtained in which with gas fluorescence was the dominant signal.

If Δ_F is set to 10 ns and t_r to 800 ps, which describes fairly well the detector gating of the camera used in the experiment in question. T can be plotted as a function of τ_1 . Such a plot is shown in Figure 5.8, accompanied there by a 2D plot of $SSIR$ as a function of the initial intensity ratio of the

one signal to the other, $\frac{S_2^0}{S_1^0}$ and τ_1 . The lifetime of the interfering signal is set to 2.0 ns. For rather short lifetimes of the fluorescence signal investigated, T is obviously low, since the initial portion of the fluorescence arrives at the detector before the intensifier has been gated on. For longer lifetimes T , increases and for fluorescence lifetimes longer than 10 ns roughly one third of the fluorescence signal can be detected. For the fraction of the fluorescence signal of interest that is detected, $SSIR$, the values obtained tend to be high for long fluorescence lifetimes and for low intensities of the interfering fluorescence signals. For fluorescence lifetimes longer than 10 ns, however, $SSIR$ is between 80 - 100 %, despite the initial intensity, S_2^0 , being 100 times as great as S_1^0 . In a measurement situation in which laser-induced signals of this magnitude and temporal shape interfere with the fluorescence signal, the effects of temporal filtering can be evaluated, through use of Equations 5.16 and 5.17, prior to conducting the experiments.

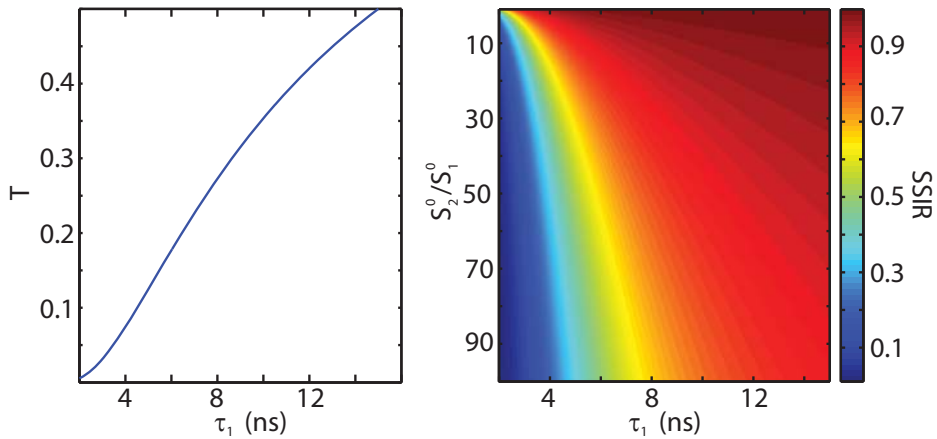


Figure 5.8: Evaluation of temporal filtering in which luminescence from a wooden pellet provides interfering signal. The fluorescence lifetime of the signal of interest, as well as the relative intensities of the initial signals are varied as T and $SSIR$ are calculated from Equations 5.16 and 5.17, respectively. The lifetime of the interfering signal is approximated to 2 ns, the rise time of the gate function being 800 ps, the delay, Δ_F , being set to 10 ns.

5.2.2 Temporal Filtering in Raman Scattering Measurements

As indicated in the previous section, the situation is more delicate if gating is performed close to the time of excitation. For measurements in which temporal filtering is performed so as to suppress interfering fluorescence when Raman signals are studied, the gating needs to be performed early so as to

reduce the fluorescence as much as possible. Still, since the Raman signature is weak there, T should be kept as high as possible. In order to evaluate the two parameters simultaneously, which is necessary since they are closely linked, detection has to be simulated.

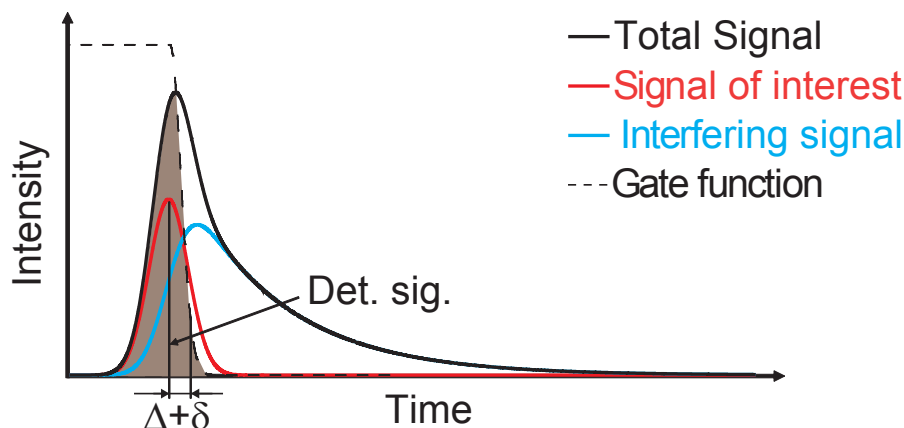


Figure 5.9: A temporally resolved schematic image of temporal filtering of interfering fluorescence in Raman measurements using an ICCD camera gate.

The full expression in Equation 5.9 needs to be used in order to describe the filter efficiency as accurate as possible. Whereas a Raman signal has essentially the same shape as a picosecond laser pulse, since it stems from a scattering process, a fluorescence emission has a temporally more complex shape. The temporal shape of the fluorescence signal was modeled, in order to be able to better understand the effects of temporal filtering for a variety of measurement situations and specifications of the equipment available. Three approaches to simulating the rising edge of the fluorescence signal were tested, convolution being by far the easiest approach. The physical system in question is reduced to a black box where the optical response from an excitation pulse is modeled as a convolution of the laser pulse and a physical response function. Such an approach could provide a certain basic understanding of how the shape of the molecular response depends on the laser-pulse width, but since it fails to include any physics, some other approach could be taken instead. A second approach that would be possible would be to model the population distribution of the molecular energy levels through use of coupled differential equations. This is a very useful approach if several energy levels are interacting. Such an approach was adopted by Kienle et al. [37], who developed a detailed rate-equation code for simulation of the energy transfer in LIF of OH radicals. The rate-equation approach allows for temporal and spectral modeling of molecular dynamics, which is of interest when temporal filtering is performed in the vicinity of laser exci-

tation. A third possible approach was one based on density matrix theory. The results for the latter approach are presented in VIII.

The fluorescence that is discriminated in real measurement situations often stems from rather complicated molecules capable of broadband absorption and emission. In applied medical or combustion-related measurements, an unknown mixture of unidentified fluorescing molecules would tend to interfere. If molecular-specific data on all the molecules that contribute to the interference in question were known, the total signal would still be impossible to model since the mixture of these molecules is unknown. Accordingly, a two-level model is employed, one in which it could be thought that rotational and vibrational energy transfer processes would need to be neglected in predicting the rising edge of the fluorescence signal. Testing of the approximation that this is the case was performed in investigating toluene, which is a rather complex molecule having broadband absorption and emission. A comparison of the simulated and the experimentally measured signals is shown in Figure 5.10.

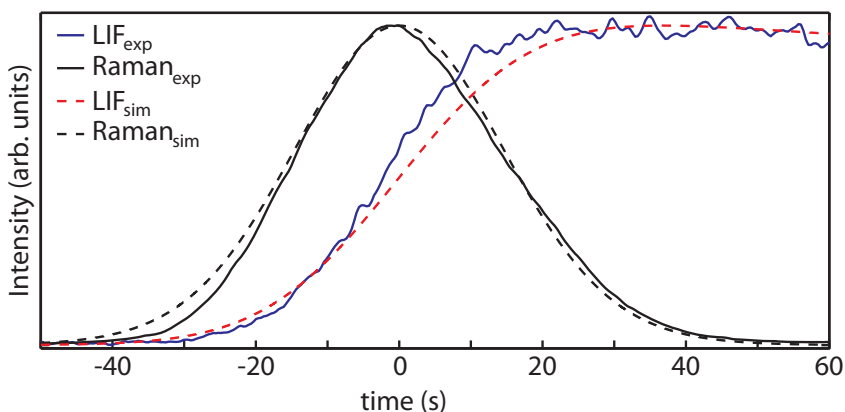


Figure 5.10: *Simulated and measured fluorescence signals of toluene are displayed as a dashed red and a solid blue curve, respectively. The laser pulse used in the simulation appears as a dashed black curve, whereas the solid black curve is the measured laser pulse. In the simulation of detection, the Raman signal is considered to have the same temporal shape as the laser pulse.*

A series of simulations was performed for a number of different laser pulse widths and quenching rates, acceptable agreement between the simulated and experimental results being obtained. Note, however, that the validation measurements performed used fairly short pulse durations (around 20 ps). Thus, the simulations for pulse durations around and longer than 500 ps should be interpreted with care.

Simulated detection with use of an ICCD camera was performed for cal-

culated Raman and fluorescence signals. To obtain results as general as possible, the ideal ICCD camera gate function was employed here, as shown in Figure 5.3. In principle, this gate function can be simplified by neglecting the rising flank, since the camera gate is closed at the point of excitation. The ideal ICCD camera gate function for use in temporal filtering in Raman studies can be described mathematically as

$$G(t, \Delta) = G_0 \left(\begin{array}{l} +[1 - \theta(t - \Delta_R + t_f)] \\ -\frac{1}{t_f}(t - \Delta_R)[\theta(t - \Delta_R + t_f) - \theta(t - \Delta_R)] \end{array} \right) \quad (5.18)$$

The aim in simulating temporal filtering for suppressing fluorescence is to obtain knowledge useful for evaluating the potential of using temporal filtering in a Raman study involving use of particular equipment. Two parameters of importance in a laser system are those of time jitter and laser pulse width. Time jitter and the shape of the ICCD camera gate function are of clear importance in connection with use of an ICCD camera. However, it is not simply the shape but also the relative transmission efficiency of the gate function which is of importance here. As the intensifier in a ICCD camera is gated with use of fast pulses, the T -value of the detection achieved is lowered substantially. This is one reason for T being a particularly important parameter to take into account. An example of the loss in collection efficiency as the gate becomes shortened has been shown by Efremov et al. [38]. The total signal strength of the Raman and the fluorescence signals are likewise of importance. The relative intensity of the two signals as they are integrated to form parameter β is

$$\beta = \frac{I_{LIF}^0}{I_{Raman}^0}. \quad (5.19)$$

As indicated above, the two signal intensities are integrated values, their being related as follows:

$$\frac{\int_{-\infty}^{\infty} I_{Raman} dt}{I_{Raman}^0} = \frac{\int_{-\infty}^{\infty} I_{LIF} dt}{I_{LIF}^0} = 1. \quad (5.20)$$

Note that β is the relative signal intensity after all possible basic filter schemes have been used to reduce the interfering fluorescence. When both a picosecond laser and a gated ICCD camera are to be used, several different filtering techniques are applicable, each of them much cheaper than a temporal filter. It is important to point out that a temporal filter is a filter that can be used to complement both spectral and polarization filters, as well as wavelength shifting schemes [39].

Similar to temporal filtering of fluorescence signals the same filter parameters (T and $SSIR$) are of interest for Raman scattering. It is highly

important to take account of all of the parameters referred to in Section 5.2 and to bear in mind that *SSIR* is problematical, since it does not scale linearly with β . A signal ratio function P of the following type can be formed:

$$P(t_{FWHM}, \Delta_R, \tau) = \tau \frac{\int_{-\infty}^{\infty} S_{LIF}(t_{FWHM}, \Delta_R, \tau) G(t, \Delta_R) dt}{\int_{-\infty}^{\infty} S_{Raman}(t_{FWHM}, \Delta_R, \tau) G(t, \Delta_R) dt}. \quad (5.21)$$

Combining Equations 5.8, 5.19 and 5.21 enables *SSIR* to be written as

$$SSIR(t_{FWHM}, \Delta_R, \tau) = \frac{1}{1 + \frac{\beta}{\tau} P(t_{FWHM}, \Delta_R, \tau)}. \quad (5.22)$$

The simulated results showed P to be fairly independent on the fluorescence lifetime as long as the lifetime is longer than 2 ns. In earlier studies of interfering fluorescence, the lifetimes of the interference signals were found to be in the range of 2-4 ns, [40], [41] and [42]. Fluorescence studies performed in our laboratories show that various combustion related interferences have fluorescence lifetimes that are longer than 2 ns, such as diesel oil, which has a lifetime of more than 5 ns after 266 nm of excitation. The simulations carried out, involved use of a fluorescence lifetime of 3 ns for the interfering signal, since this could provide data particularly useful for experimentation in this field of applied science. Simulated detection results for seven different fall times of the ICCD camera gate function are shown in Figures 5.11 and 5.12. P and T values are presented there as a function of laser pulse duration and of gate delay time.

The image at the top in Figure 5.11 concerns temporal filtering with use of a streak camera that could be considered as a detector having zero fall time. Obviously, this is a special case for which the filtering is very effective. At the same time, the streak camera is rather insensitive as compared with an ICCD camera, since in the former the spectrometer slit is perpendicular to the streak camera slit. A streak camera also spreads out the Raman signal over several pixels so as to obtain a high level of temporal resolution, which leads to the signal-to-noise ratio being rather low. The two-dimensional plots shown in Figure 5.12 displays P and T values for longer fall times of the gate function, the shapes and gradients in the plots there being smoother. Obviously, the signal is cleaner for shorter delays, since the fluorescence signal peaks later than the Raman signal does, as can be seen in Figure 5.10.

For shorter fall times, the laser pulse width has a rather strong impact on the results, whereas for longer fall times of the gate function the impact is lower, especially in case of long delay times. Thus far, the role of time jitter in the model has not been discussed. For purposes of simplicity, time jitter, or temporal broadening effects of other types, can in case of accumulated data be included in the duration of the laser pulse, which has a broadening

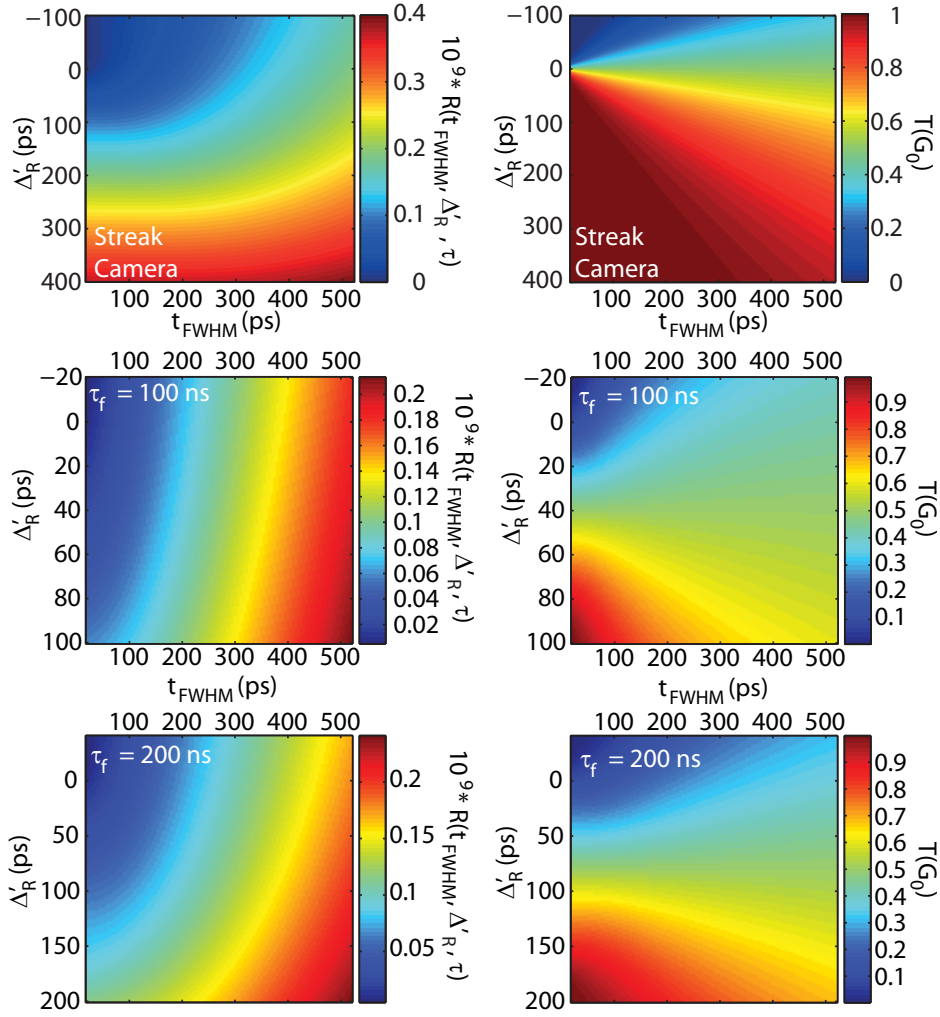


Figure 5.11: P and T values for different fall times of the camera gate function, involving different delay times and laser pulse widths. In the two images at the top, a zero fall time of the camera gate is employed, this correspond to use of a sharp integration limit, one that could be used for the temporal filtering of streak-camera data.

effect on the fluorescence signal. Single shot measurements can be performed here within the span of a variety of different delay times.

In evaluating the temporal filtering of interfering fluorescence in Raman spectroscopy, several of the parameters are fixed, which means that such dimensions as those of pulse width, time jitter and fluorescence lifetime for example, may be known. The graphs shown in Figure 5.11 and 5.12 can be useful in helping one determine what type of camera to employ and how best to use it, which laser system is preferable over another, what potential the equipment at hand has for performing temporal filtering. In paper VIII,

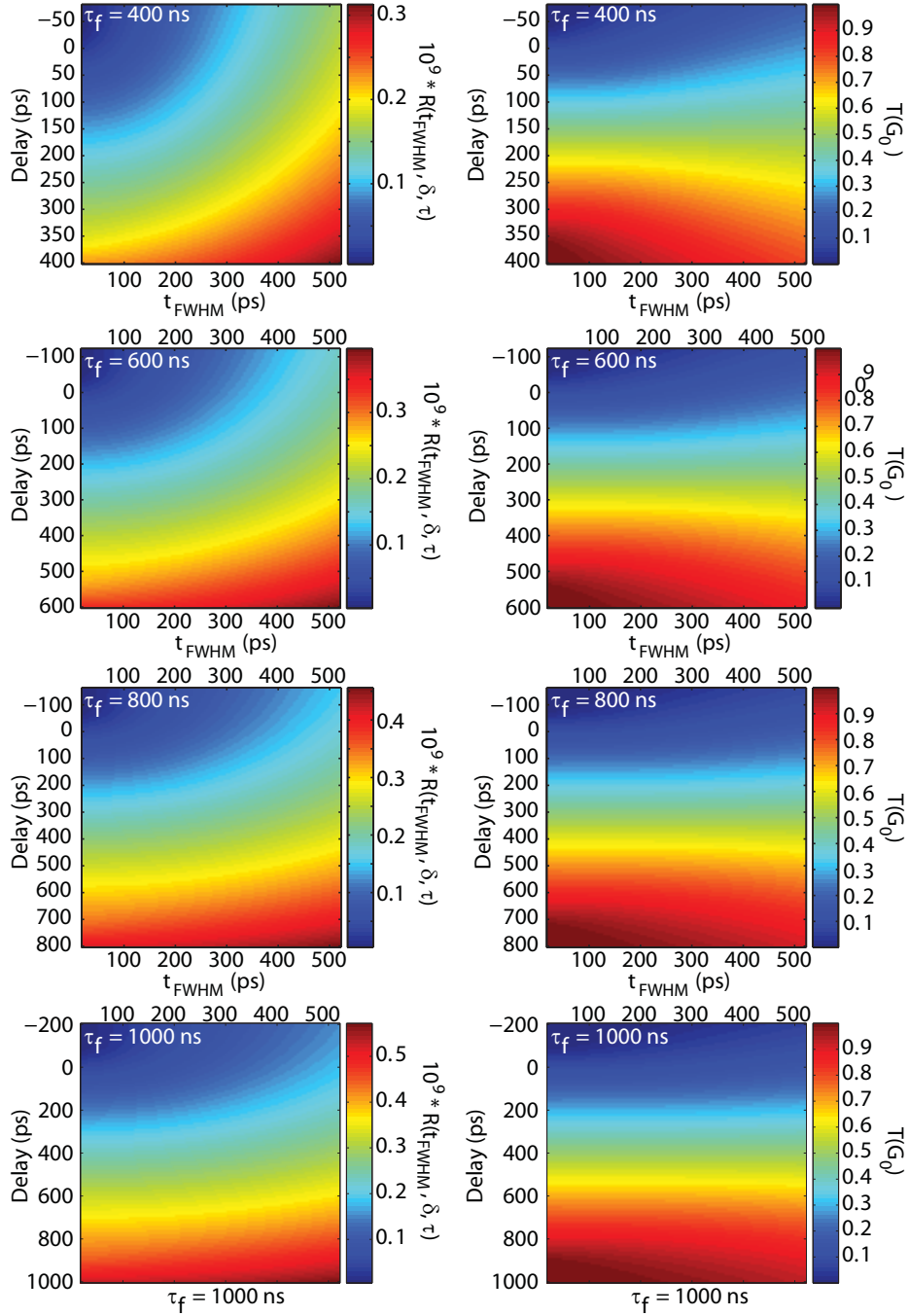


Figure 5.12: R and T values shown as functions of the laser pulse duration and of the camera delay time for full times of the camera gate function of 400 -1000 ns.

the type of scheme used in Raman imaging is demonstrated and an example is presented of how an evaluation algorithm can be used to evaluate the

effectiveness of temporal filtering in a particular experiment.

A demonstration example of how temporal filtering of fluorescence in Raman spectroscopy takes place is shown in Figure 5.13. The slowly varying fluorescence signal is Rhodamine 590, dissolved in nitromethane in which the Raman peaks can be seen. A reference spectrum, obtained without temporal filtering, is displayed as a dashed line in the plot at the left in Figure 5.13, where only faint indications of Raman peaks are discernible. In performing temporal filtering, a camera-gate function having a gate width of roughly 2 ns was delayed at three different delay times (Δ_R). Three spectra, acquired using different camera-delay times and thus containing different fractions of Raman and fluorescence signatures, are displayed as three solid lines in the image at the right in Figure 5.13. By obtaining clean Raman spectra from nitromethane using different camera delay times enabled the Raman signals to be analyzed separately. T , plotted as a black solid line connected to filled circles, as shown at the right in Figure 5.13, could be evaluated on the basis of this these data. The $SSIR$ -values for two integrated Raman peaks, located at around 575 and 630 nm and marked out by (x) and (+) symbols, are plotted for different camera delay times Δ'_R in the plot at the right in Figure 5.13. $SSIR$ was analyzed with the integration intervals marked as pink areas in the plot at the left. The $SSIR$ -values of the two peaks for the three temporally filtered spectra that are shown in the image at the left are highlighted by rings of corresponding colors. Obviously, the Raman spectrum that appears is clearer seen if the gate has advanced in time, although the strength of the Raman signal is then reduced substantially. The $SSIR$ -values depend upon the amount of fluorescence present as compared with the intensity of the Raman signals, the two peaks, (x) and (+), differing in these respects. Clearly, there is no point in using a camera-delay time longer than the fall time of the camera gate function, since $SSIR$ becomes progressively lower and T is close to its maximum value. A delay time of 0.7 ns, corresponding to the spectra represented by the blue line in Figure 5.13, yields the highest signal-to-noise ratio for the Raman signal and still provides a fairly clean spectrum (i.e. a high $SSIR$ value). Camera-delay times of less than 0.7 ns, however, result in lower signal-to-noise ratios, although the Raman spectrum recorded is clearer.

With this in mind, it is important to clearly identify what kind of information that is important in various applications. If Raman imaging is performed it might only be of interest to obtain some kind of signature of the object in question. In contrast, in a spectroscopic investigation the fluorescence background can be subtracted in some cases. Increasing the delay sufficiently results in the Raman signal vanishing and only the fluorescence signal being detectable. If the shape of the fluorescence spectrum is independent of the time at which it was acquired, all of the spectra can be assumed to have the same fluorescence lifetime. If this assumption is valid,

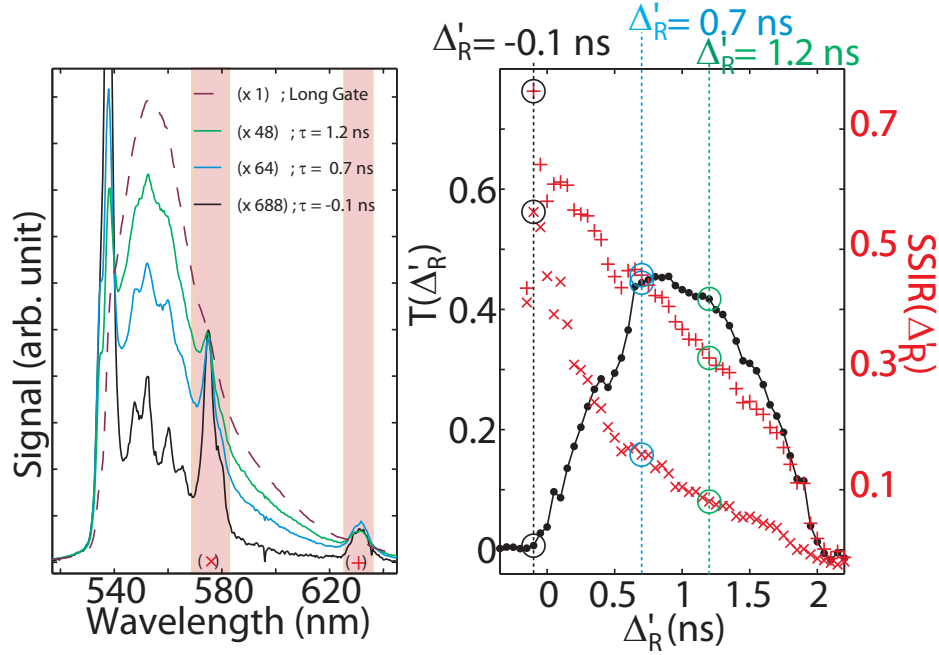


Figure 5.13: *Left)* The dashed line represents the spectrum acquired without use of temporal filtering. Only weak signs of Raman peaks are to be seen. The solid lines denote acquired Raman spectra having an interfering fluorescence background, as obtained for different camera delay times. The strength of the interfering fluorescence is reduced as the delay times are shortened, this leading to the Raman spectra appearing. *(Right)* The interval of integration of two Raman peaks, marked with (x) and (+) symbols appear as pink-colored areas. The black line with filled circles represents the total signal strength of the Raman spectrum, shown as a function of camera-delay time normalized to a reference Raman spectrum acquired with the help of a long camera-gate function, defined as T in Equation 5.7. The red (x) and (+) values are the evaluated SSIR-values of the Raman signals as integrated within the pink-colored intervals shown in the image at the left. The black, blue and green rings are the evaluated results from the spectra, the colors of which correspond to the spectra in the image to the left.

the fluorescence background can be acquired separately. If there is a spectral window in which no Raman peaks are present the relative strength of the fluorescence spectrum background can be found and then be subtracted from the spectrum. This is illustrated in Figure 5.14, in which a very pure Raman signature is obtained after subtraction of the background.

5.2.3 Signal-to-noise limits in filtering and background subtraction schemes

In dealing with filters and interfering signals, the limitations on detection are important to define. If no interfering signals are present or if they are very

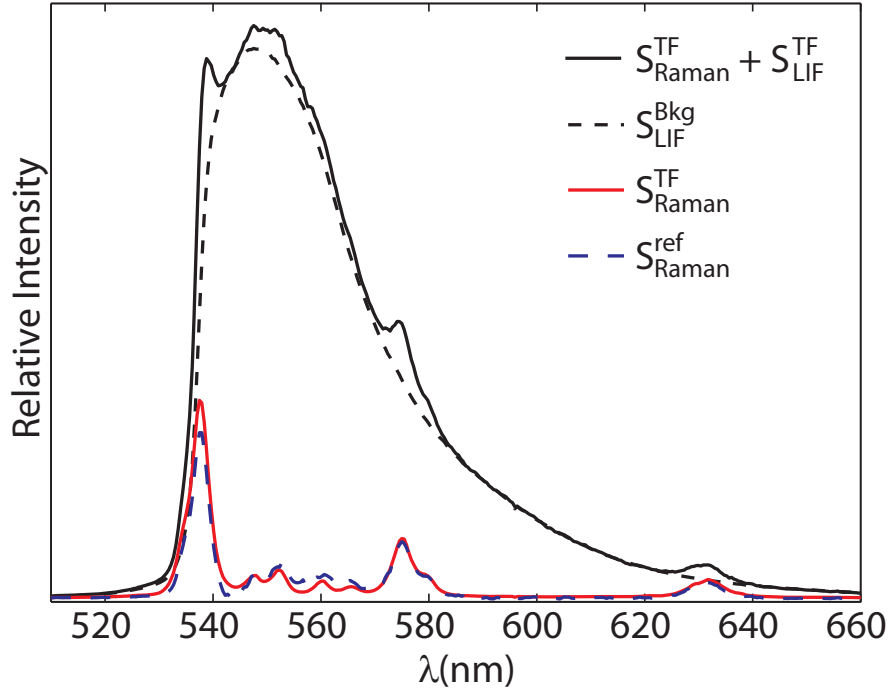


Figure 5.14: The black solid line represents the mixture of Raman and fluorescence spectra after temporal filtering ($S_{Raman}^{TF} + S_{LIF}^{TF}$) has been performed, the Raman peaks appearing as small bumps on the fluorescent background. The green dashed line is the background fluorescence, S_{LIF}^{Bkg} , acquired under conditions in which the camera gate is only delayed so as to capture the fluorescence decay. The background spectrum here has been normalized in relation to the mixed spectrum (the solid black line) within a spectral range in which no Raman peaks are located, within the interval of 594-619 nm. The red line represents temporally filtered data after background subtraction, its displaying a clear Raman spectrum (S_{Raman}^{TF}). The background-subtracted temporally filtered Raman spectrum shows close agreement with the dashed black line, which is a references Raman spectrum of nitromethane (S_{Raman}^{ref}).

small, the signal of interest has to compete with CCD-noise. Such could be the case for fluorescence signals that are perturbed by shorter signals, such as those of elastic scattering, or in the very early parts of the Raman signal, as shown by the black solid curve in the plot at the left in Figure 5.13.

For an ICCD camera the noise sources are dark-current and read-out noise. The dark current part is a signal contribution that originates from

thermally generated electrons in the CCD chip. As for all signals, this signal displays a statistical fluctuation, termed dark-current noise. The dark current can be reduced by cooling down the CCD chip, this obviously also reducing the noise. Readout noise is noise associated with the readout process of the CCD chip. It is dependent upon the frame rate but is independent of the integration time. To be able to detect a signal, it has to be at least twice as strong as the noise that the CCD camera produces, if one disregards interferences of other types that may be produced. In the case of weak signals, the CCD noise can be reduced by accumulating the signals on the CCD chip and only performing one read-out per image. There is a drawback, however, in accumulation by use of a temporal filter due to the time jitter produced, especially in the case of Raman measurements, in which the interfering fluorescence signals have rather steep gradients in the temporal domain. Since a time jitter is a statistical variable an accumulated frame of several laser excitations has a rather high probability of being ruined if the time jitter adds time to the delay and the signal is buried in fluorescence. On the other hand, one may be able to circumvent problems of the CCD noise through extending the delay involved though this may increase the strength of the interference signal, it may also increase the strength of the signal of interest, doing so to an extent that the latter is clearly stronger than the level of the CCD noise. However, if one performs background subtraction, the signal of interest has to compete with the shot noise of the interfering signals. Shot noise reflects the imperfection of the occurrence of single events in the sense of their occurrence readily deviating from what one could expect on average values for the occurrence. In the detection of optical signals, the detecting of photons is one such event. The shot noise could be manifested spatially, where on the CCD matrix the photons are integrated, or temporally, concerning where the photons are integrated in terms of small time boxes, when the samples obtained are displayed over time. Shot noise follows Poisson statistics, which means that the standard deviation can be found as the square root of the number of events involved. When the signal is detected by a detector, in this particular case an ICCD camera, the total noise obtained is a combination of several different terms. In a paper by MacGinty et al. [43], the strength of the signals detected by an ICCD camera (I) is described as

$$I = kS_{Ph} \tag{5.23}$$

where k is the conversion constant and S_{Ph} is the number of photons detected. The noise of an ICCD camera can be characterized, and the total noise be described, as

$$\nabla_I^2 = S_{Ph}^2 \nabla_k^2 + k^2 \nabla_{S_{Ph}}^2 + \nabla_{CCD}^2 \tag{5.24}$$

Here, ∇_k^2 , ∇_{Ph}^2 and ∇_{CCD}^2 are the standard deviation of the conversion con-

stant, the detected number of photons and the sum of the detector noise, respectively. Since the statistics of the detected photon signals can be described in terms of Poisson statistics, a more general expression of the noise can be written as

$$\nabla_I^2 = AS_{Ph}^2 + k^2ES_{Ph} + \nabla_{CCD}^2 \quad (5.25)$$

The constants A , E and k were measured by McGinty et al. [43] for a given detector at different gain voltages of the intensifier, these values being listed in the paper. In a situation in which the background can be subtracted, as shown in Figure 5.14, the signal of interest that is extracted has to be at least twice as strong as the noise of the total signal. By neglecting both the CCD noise and the first term in Equation 5.25 through assuming A to be zero, which according to the values presented by McGinty et al. seem to be a rather sound assumption in the case of a single MCP under conditions of moderate voltage, the relation between the two signals can be written as

$$I_{Raman} \geq 2\nabla_{I_{tot}} = 2k\sqrt{ES_{Ph}} \quad (5.26)$$

This relationship can then be inserted into the expression for $SSIR$ in Equation 5.8 to yield

$$SSIR = \frac{I_{Raman}}{I_{Tot}} = 2\sqrt{\frac{E}{S_{Ph}}} \quad (5.27)$$

By regarding the camera used by McGinty as a typical ICCD camera, the lowest $SSIR$ value can be calculated for a Raman signal that it would still be possible to detect. Under the assumption that the total number of detected photons is optimized with respect to the voltage of the intensifier, the lowest $SSIR$ value can be evaluated in terms of Equation 5.27 for the values listed in [43]. For voltages of below 600 V, $SSIR$ is less than 8 %. This means that if the Raman signals represent less than 8 % of the total signals provided, the delay has reduced in length. If this is impossible because of the Raman signals being too weak, an additional filtering technique needs to be employed in order to be able to determine the Raman peaks.

Chapter 6

Fluorescence Lifetime Imaging (FLI)

THIS chapter provides a brief review of different lifetime evaluation schemes for single exponential decays. In light of the importance of being able to apply conceptions of this sort to the use of experimental hardware, the evaluation scheme DIME (Dual Imaging with Modeling Evaluation) is presented. Note that DIME can also be used in connection with non-single exponential signals. The DIME conception was here used in fluorescence lifetime imaging (FLI). FLI techniques basically comprise all measurement techniques that can generate a two-dimensional image of the fluorescence lifetime. The scheme was developed originally for assessing the fluorescence quantum yield in two-dimensional terms in single-shot measurements, as a step towards quantitative fluorescence imaging.

6.1 Lifetime Determination

For simplicity, only single exponential decays, or signals that can be approximated as being single exponential in character, will be considered here. The signal then has the temporal response function

$$R(t) = R_0 e^{-t/\tau} \theta(t), \quad (6.1)$$

where $\theta(t)$ is the Heaviside step function, R_0 is the initial intensity and τ the fluorescence lifetime decay constant.

6.1.1 Lifetime determination in the frequency domain

There are a number of ways of determining fluorescence lifetimes. Basically, the fluorescence lifetime can be determined either in the frequency or in the

6. FLUORESCENCE LIFETIME IMAGING (FLI)

temporal domain. There are a number of well-written review articles and textbooks on lifetime determination in the frequency domain that can be consulted for details [44], [45], [46]. The basic idea of lifetime determination in the frequency domain is to modulate the laser light sinusoidally:

$$L(t) = L_0(1 + M_L \sin(\omega t)). \quad (6.2)$$

The average excitation intensity is denoted as L_0 and the modulation depth as M_L . The modulation depth is the ratio of the AC component, i.e. the amplitude, to the DC component, i.e. the offset, of the signal. Since fluorescence has a lifetime, the signal is delayed in comparison to the excitation frequency, this introducing a phase shift (ϕ) between the laser and fluorescence signal as well as a new modulation depth, M_F .

$$F(t) = F_0(1 + M_F \sin(\omega t + \phi)). \quad (6.3)$$

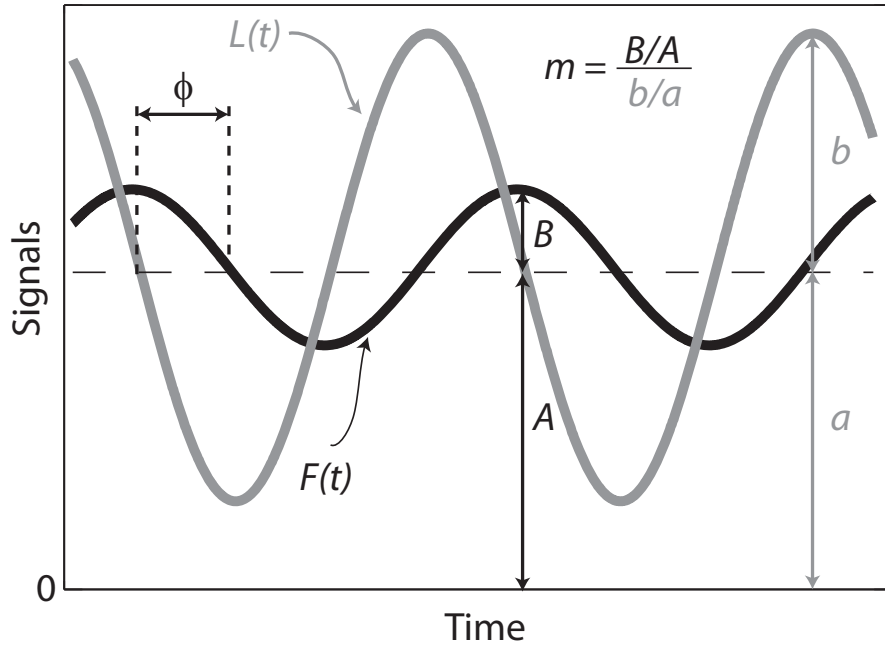


Figure 6.1: The gray solid curve represents the modulated excitation source, the black curve representing the modulated fluorescence signal. The lifetime is found on the basis of the phase shift ϕ or of the relative modulation depth m , as shown in the image.

A schematic of the signals in question is presented in Figure 6.1. The two parameters that can be evaluated in order to determine the fluorescence lifetime are the relative modulation depths of the excitation light and the modulated fluorescence signal, this being related to the modulation fre-

quency, ω , and the fluorescence lifetime, τ , as follows:

$$m = \frac{M_F}{M_L} = \frac{1}{\sqrt{1 + \omega^2 \tau^2}}, \quad (6.4)$$

and to the phase shift,

$$\phi = \tan^{-1}(\omega\tau). \quad (6.5)$$

Fluorescence lifetime determination within the frequency domain can be performed both by imaging and by modulating the intensifier of the ICCD camera [47]. In an investigation by Elder et al. [48] fluorescence lifetime imaging schemes that utilize the frequency domain were evaluated using Monte Carlo simulations to determine the sensitivity of the evaluation algorithms. The value used to evaluate a detection scheme is that of the figure of merit, F , defined [49] as

$$F = \frac{\sigma_\tau}{\tau} \left(\frac{\sigma_{N_{tot}}}{N_{tot}} \right)^{-1}. \quad (6.6)$$

In principle, the figure of merit is a measure of how much the signal-to-noise ratio is degraded in the evaluation algorithm. High sensitivity corresponds to low figure of merit and vice versa. For example, if the detected signal has a signal-to-noise ratio of 30, the F-value is 3 if τ/σ_τ has a value of 10. On the basis of simulations they performed, Elder et al. [48] found both the F-value of sinusoidally modulated excitation and the intensifier to have an F value of more than 8, which is rather high compared with evaluation schemes applying to the time domain.

6.1.2 Lifetime determination in the temporal domain

FLI in the temporal domain is a bit more intuitive and straightforward. The excitation source used for FLI in the temporal domain is pulsed. As illustrated in Figure 5.1, the pulse duration has to be sufficiently short compared with the lifetime of the signal if one is to be able to evaluate the lifetime of the signal adequately. The signal shape can be calculated as the convolution of the shape of the excitation pulse, $L(t)$, with the signal response function, $R(t)$, the calculations performed here for analyses in the frequency domain. To simplify the analysis, it was assumed that the excitation pulse is a Dirac pulse. The most straightforward method for analysing decay curves is to perform temporally resolved pulse excitation measurements as point measurements. Since the signals are represented by two vectors, those of intensity and of time, the data can be arranged in form of a linear curve, the derivative of which is the inverse of the lifetime,

$$\ln(R(t)) = -\tau^{-1}t + \ln(R_0). \quad (6.7)$$

The decay, τ can then be found by evaluating the data with use of least square fitting. Although the idea is rather intuitive, the results are strongly dependent upon accurate background subtraction, its being based on signal data that are unaffected by the signal response functions of the detectors or by duration of the excitation pulse. This procedure can only be applied to temporally resolved data, either through one-dimensional measurements were obtained using a streak camera, or through scanning an area with the excitation and detector equipment.

Time Correlated Single Photon Counting

A detector scheme called time correlated single photon counting (TCSPC) is advantageous to use in measuring short fluorescence lifetimes [50]. In TCSPC point measurements are performed with use of a pulsed excitation source. The detection is governed by a fast point detector, such as a PMT or a MCP. The temporal shape that develops is built up by mapping the probability density function (PDF) of the times of arrival of the photons as registered by the detector. It involves measuring successively the difference in time between the laser pulse and the first photon that arrives at the detector. The time differences measured in this way are stored in a histogram memory in which the statistics are collected. Since only one statistical event is sampled following each laser excitation, several laser excitations are needed to build up the statistics. The final result is a histogram that describes the temporal shape of the fluorescence signal. The obvious advantage of this technique is that it enables multiple fluorescence lifetimes of a signal to be evaluated. Also, the temporal resolution can be as low as tens of picoseconds [51]. A high-repetition-rate laser system needs to be used, however, since only one photon per excitation is acquired. Furthermore, it is a point measurement technique in which a scanning procedure needs to be performed in order for a fluorescence lifetime image to be obtained.

Box-car integration techniques

Box-car integration is a lifetime determination approach that does not involve sophisticated fitting routines or ultra-high temporal resolution. The best known form of it is one that was presented by Ashworth and co-workers [52]. This scheme involves performing three box car integrations, the lifetime being obtained by use of an analytic expression. When experiments are carried out the number of integrations is kept at a minimum. This simplifies the scheme, reduces the algorithm to its involving only two box-car integrations. The evaluation routine employed here is termed the standard rapid lifetime determination algorithm (SRLD). The idea behind it is presented in Figure 6.2.

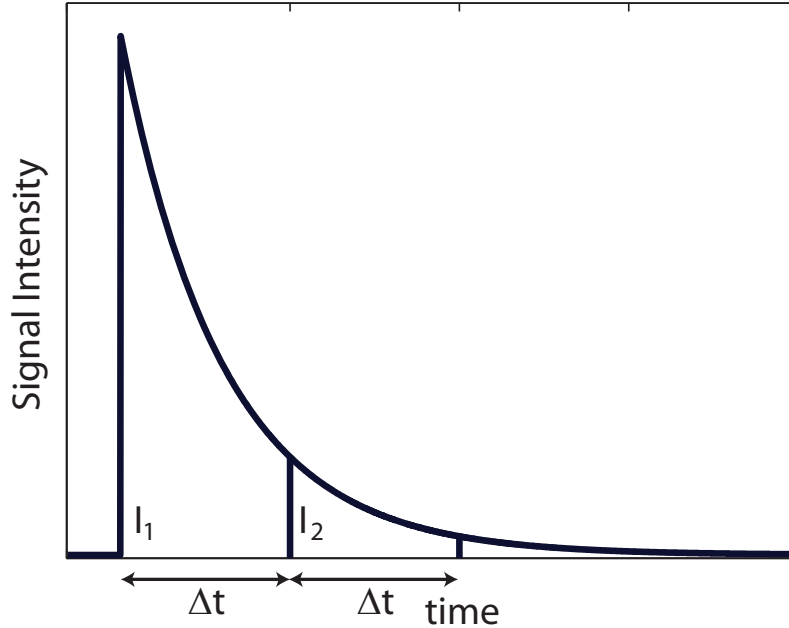


Figure 6.2: *Box-car integration using the SRLD algorithm proposed by [52]. The two areas; I_1 and I_2 are used in Equation 6.8 to determine the lifetime of the curve. A second parameter could be introduced to reduce the width of the integration boxes. For simplicity this parameter is not included here, partly because a smaller integration interval would make the algorithm rejecting a larger number of photons, which would result in worse signal-to-noise ratio.*

The integrated values I_1 and I_2 and the time separation between them, Δt , can be used to form the following analytical expression of the lifetime, τ .

$$\tau = -\frac{\Delta t}{\ln\left(\frac{I_2}{I_1}\right)}. \quad (6.8)$$

The evaluations to be made are easily performed, with use of such a compact formula, by means either of point measurements or of imaging. The SRLD evaluation formula has been used in a number of publications for determining fluorescence lifetimes, e.g. [53], [54], [55]. When use is made of ICCD cameras, the gate function is assumed to correspond to a square integration box, one that enables a fluorescence lifetime image to be produced. This involves using the camera delay time, Δt , for performing gated imaging, in a manner similar to the integration scheme shown in Figure 6.2. The two PLIF images are used to form a ratio image in which every pixel value can serve as input data to Equation 6.8, enabling a fluorescence lifetime image to be produced. Despite the many advantages of RLD, the

sensitivity of the scheme is strongly dependent on the fluorescence lifetime that is being determined. To overcome this difficulty, another approach was developed by Chan et al. [56], that of the optimized rapid lifetime determination algorithm, as it is called, which is likewise based on box-car integration, but with the box widths and the locations optimized so as to enable the lifetime obtained to have as low a standard deviation as possible. The integration boundaries are shown in Figure 6.3. The two integrals can

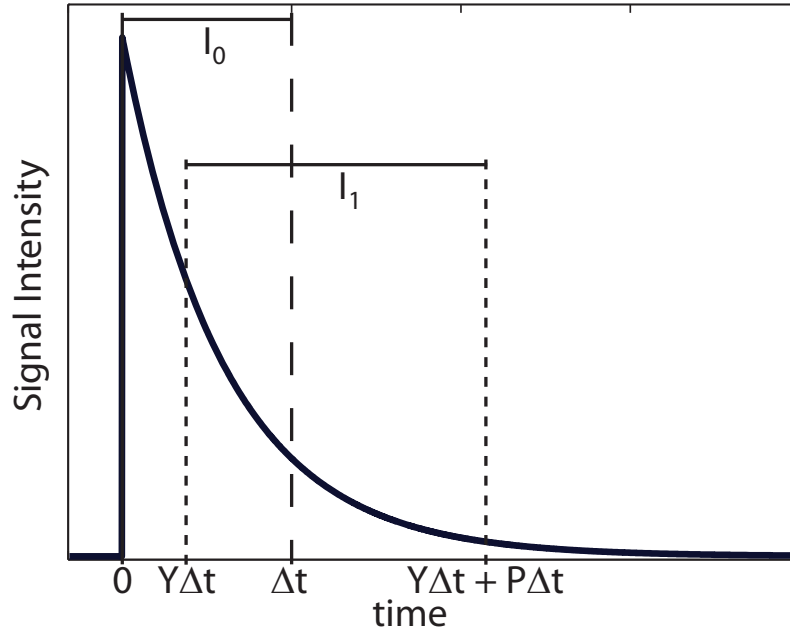


Figure 6.3: The box car integration algorithm called ORLD, proposed by Chan et al. [56]. The value I_0 is integrated in the interval $[0 : \Delta t]$, and I_1 in the interval $[Y\Delta t : Y\Delta t + P\Delta t]$.

be formulated as

$$I_0 = \int_0^{\Delta t} R_0 e^{-t/\tau} dt \quad (6.9)$$

and

$$I_1 = \int_{Y\Delta t}^{Y\Delta t + P\Delta t} R_0 e^{-t/\tau} dt. \quad (6.10)$$

The variables Y and P are adjustable coefficients for the integration intervals. The ratio of the one integration to the other is formed, yielding the following expression:

$$\frac{I_1}{I_0} = \frac{e^{-R(P+Y)} - e^{-RY}}{e^{-R} - 1}, \quad (6.11)$$

where

$$R = \frac{\Delta t}{\tau}. \quad (6.12)$$

In contrast to SRLD, the optimized version has no analytic solution, but can be solved by use of an iterative Newton-Rhapson method. The optimum choice of the parameters Y and P was determined as being $4/\tau$ and $8/\tau$, respectively. The ORDL algorithm, which has been employed in sensors [57], is advantageous for use in lifetime determination by employing ICCD cameras. The fact that this scheme is not used routinely may be due to the change in detector efficiency that occurs when the width of the camera gate function is changed [38].

Ramped Gain Profile Lifetime Determination

In Paper VI a lifetime determination algorithm termed RGPLD, short for ramped gain profile lifetime determination algorithm, is proposed. This is an evaluation algorithm which is not based on box-car integration but rather is an intensification of the signals, using ramped profiles prior to integration. In the other two algorithms mentioned above, use is made of the ratio of two separate values. These are intensification functions, that either are two ramped gain profiles having derivatives that are of differing signs but have the same absolute value, or consist of one ramped profile and one box-car integration, are shown in Figure 6.4. The same result can be achieved by forming ratios of different types.

If one ramped gain profile and one constant intensification is employed prior to integration, a ratio similar to the algorithms presented earlier is used in Equations 6.8 and 6.11. If in selecting t_1 it is assumed that the exponential function is zero, the gain profiles, the integration and the ratio can be written as

$$G_{RGP}(t) = \frac{G_0}{t_1 - t_0}(t - t_0)[\theta(t - t_0) - \theta(t - t_1)] \quad (6.13)$$

$$G_C(t) = G_0[\theta(t - t_0) - \theta(t - t_1)] \quad (6.14)$$

$$I_{RGP} = \frac{R_0 G_0}{t_1 - t_0} \int_{t_0}^{t_1} (t - t_0) e^{-t/\tau} dt \approx \frac{R_0 G_0}{t_1 - t_0} e^{-\frac{t_0}{\tau}} \tau^2 \quad (6.15)$$

$$I_C = R_0 G_0 \int_{t_0}^{t_1} e^{-t/\tau} dt \approx R_0 G_0 e^{-\frac{t_0}{\tau}} \tau \quad (6.16)$$

$$D = \frac{I_{RGP}}{I_C} \approx \frac{\tau}{t_1 - t_0} \quad (6.17)$$

6.1.3 Comparisons between the lifetime determination algorithms

The fact that D is proportional to the lifetime is advantageous for reasons that will be taken up in connection with the results of random sampling

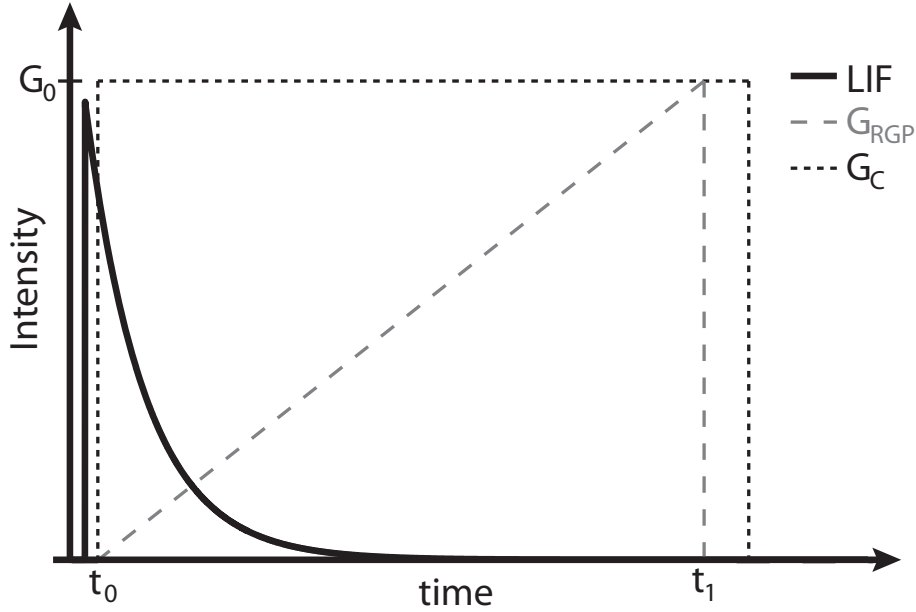


Figure 6.4: A schematic of the RGP lifetime determination using one ramped gain profile before integration and one simple box car integration with continuous intensification. Obviously, the efficiency is optimal if t_0 coincide with the time of excitation, but if the instrumental function of the system is sufficiently long, a delay of the intensification is possible

simulations in which SRLD, ORLD and RGPLD are used as detector schemes for lifetime determinations based on the use of two identical detectors. The scheme is shown graphically in Figure 6.5. The simulations are fairly simple, involving three random samplings:

1. The number of photons collected that form an image in a pixel that is governed by Poisson statistics. The mean value of this Poisson distribution determines the signal strength of the simulated measurement situation involved.
2. The probability of a photon being directed at either of the two detectors.
3. The arrival time of the photoelectron at the intensifier.

The methods used for these simulations follow certain ideas reported by Elder et al. [48] and by Carlsson et al. [58]. The results of the simulations are presented in three separate plots. The parameters involved are listed in Table 6.1.

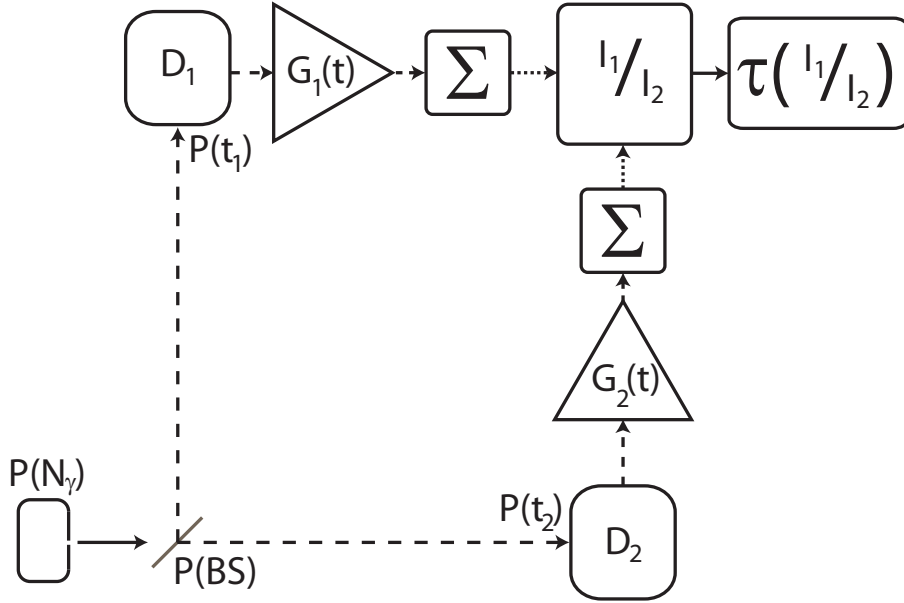


Figure 6.5: A schematic of the random sampling model used to evaluate lifetime determination algorithms. A number of photons is directed at one of two detectors by use of a beam splitter. The arrival time at the detector is sampled and the event is multiplied by a gain function, $G_i(t)$, its being integrated thereafter. The output parameter, τ is found by use of the evaluation algorithm.

Table 6.1: Parameters used in the random sampling simulation

System parameters	SRLD	ORLD	RGPLD
$N_\gamma = 350$	$\Delta t = 3 \text{ ns}$	$t_0 = 0$	$\Delta t = 3 \text{ ns}$
$T_{BS} = 50/50$	$Y = 0.25$	$t_1 = 70$	
$N_{meas.} = 1000$	$P = 12$		

The figure of merit, defined in Equation 6.6, is the first parameter that is analyzed, the results being shown in Figure 6.6. The SRLD algorithm has a very low F-value and applies to a narrow interval, its being strongly dependent on the fluorescence lifetime. For very short lifetimes, the detector that acquires the signal in a later interval (through use of SRLD) simply fails to detect a signal. This makes SRLD ineffective in determining very short lifetimes. For longer lifetimes, the difference between the two detected values, I_1 and I_2 , is very small, making SRLD insensitive for the detection of longer lifetimes.

An optimized RLD was developed so as to avoid these imperfections, its providing a figure of merit result that is more stable in the interval which is

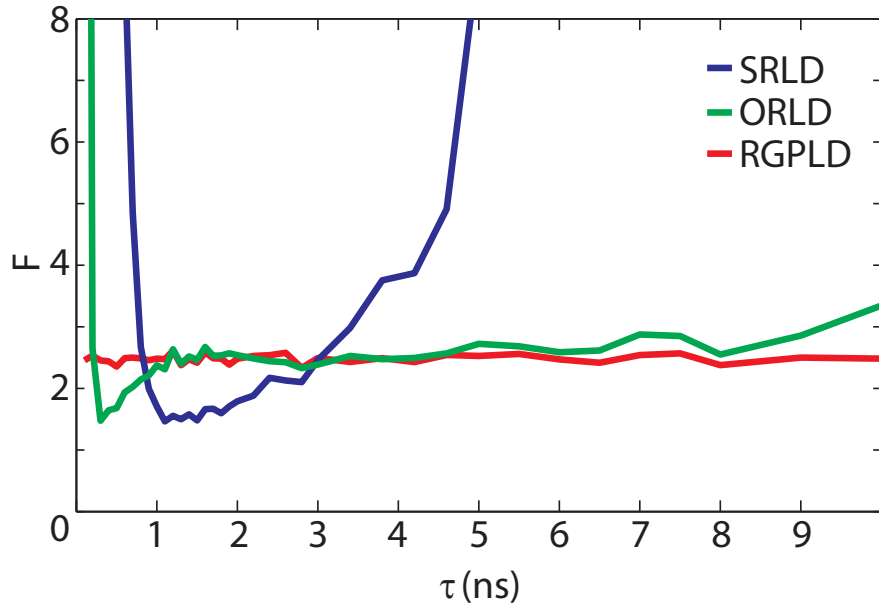


Figure 6.6: *The figure of merit values obtained lifetime determination algorithms that were evaluated. The RGPLD and ORLD algorithms were found to be independent of the fluorescence lifetime, and the SRLD algorithm to be optimized at around 1.5 ns.*

investigated. The values of F , however, is still dependent upon the fluorescence lifetime. The RGPLD algorithm, in contrast, is virtually independent of the lifetime, but at the same time it is not optimized for any specific range of lifetimes.

The second parameter evaluated was the degree of misprediction of the lifetime, due to the low signal-to-noise ratio of the signal, that the different algorithms showed. Since the specific values of the error in question are strongly dependent upon the number of photons used in the simulations, the absolute error is of no general interest. Experimental measurement schemes should be able to provide as accurate predictions as possible at low signal-to-noise ratios. Since RGPLD ideally shows a linear relationship between this ratio and the lifetime of the signal, the algorithm has a very low degree of error in predicting the lifetime. Again, the systematic error of determination that the optimized RLD shows is much less than 4 % in the interval in question which is rather good performance as compared with SRLD.

The third parameter that was evaluated was the mean-to-standard deviation ratio for the lifetime that was obtained. For fluorescence lifetimes of around 1 ns, the three algorithms provided quite similar ratios. For the other parameters that were evaluated, the SRLD algorithm resulted in a ratio that varied strongly with the lifetime of the signal, whereas the RGPLD

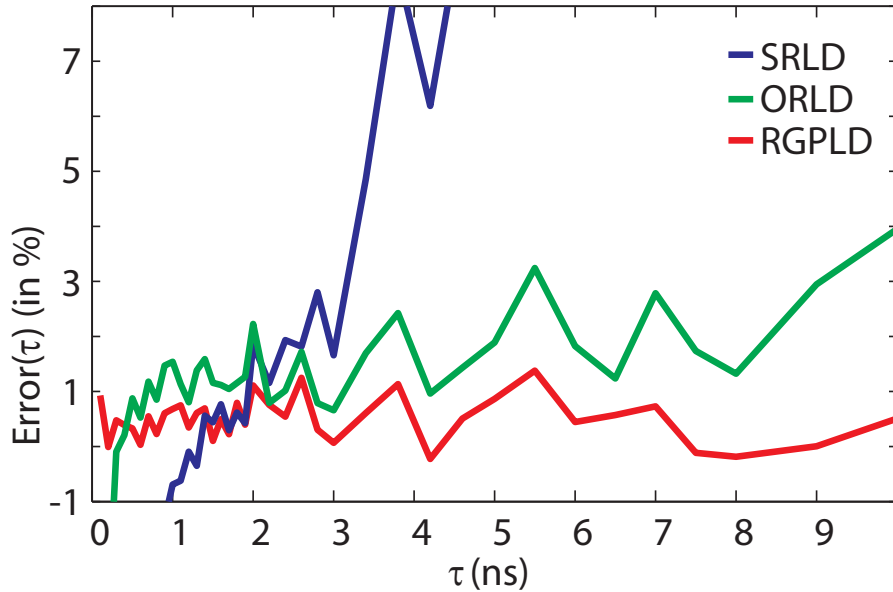


Figure 6.7: The error in determining the lifetime for each of the three different schemes. The mean value of the lifetime using SRLD is within $\pm 1\%$ in the interval of 1-2 ns, and RGPLD and ORLD can predict the lifetimes rather accurately in this interval. Note that the error is that of the mean value, which is a systematic error.

and ORLD algorithms showed more desirable features.

These results showed ORLD and RGPLD to possess much better features for performing fluorescence lifetime imaging than SRLD did. However, the temporal shapes of a real ICCD-camera gate function are not a perfect top-hat function, and are not triangular either. Thus, these theoretical schemes should be considered merely as guidelines for a more detailed algorithm that can compensate for the imperfections found in the gate functions. Such a detection scheme is presented in the chapter that follows.

6.2 Dual Imaging with Modeling Evaluation

Two integrated values can be obtained by performing dual acquisitions of a measurement object. If the temporal characteristics of the gate functions in the two acquisitions differ, the integrated values, I_1^{Exp} and I_2^{Exp} , can also differ. If the measurement conditions (object and excitation) are the same, the differences between the integrated values can be assumed to be due to differences in the temporal time characteristics of the respective gate functions. In theory, this can be investigated by use of the lifetime determination

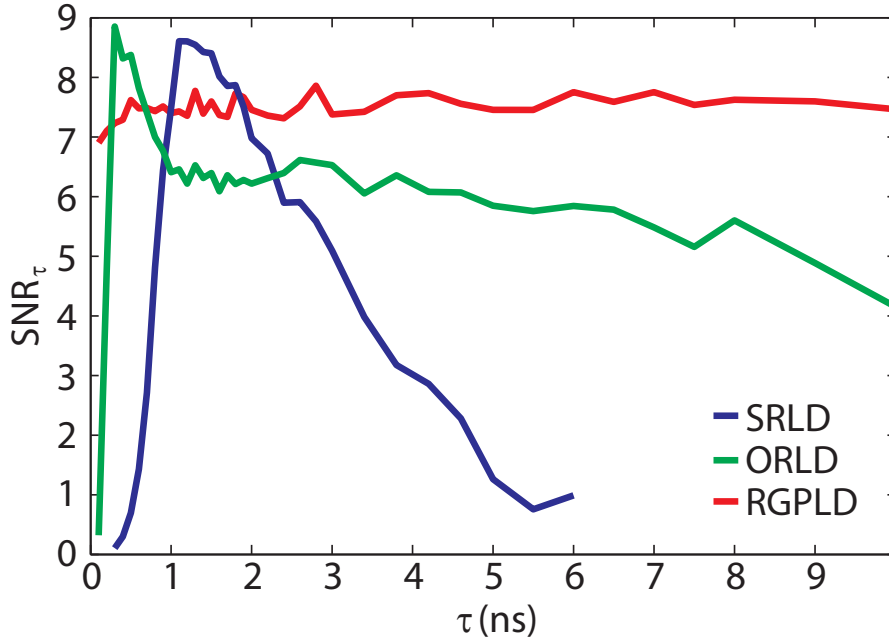


Figure 6.8: *The ratio of the mean to the standard deviation of the lifetime, which for simplicity's sake is referred to as SNR_{τ} . Again, SRLD is optimized for lifetimes of around 1 ns, whereas both RGPLD and ORLD predict lifetimes on the basis of SNR_{τ} , which is largely independent on the lifetime.*

algorithms discussed earlier. If ICCD cameras are used as detectors the results have spatial dimensions. A single camera can be used for acquiring both images if the variations in the excitation employed and the measurement object involved as the two images are acquired are insignificant. If two cameras are used, the images need to be matched pixel-by-pixel. A ratio of the two images is obtained so as to cancel out the initial signal intensities contained in each pixel. The two images are then arranged so as to form a ratio, $D_{12}^{Exp}(x, y)$, such that

$$D_{12}^{Exp}(x, y) = \frac{I_1^{Exp}(x, y)}{I_1^{Exp}(x, y) + I_2^{Exp}(x, y)}. \quad (6.18)$$

If the signals that are integrated in each pixel have the same temporal shape, the ratio image is a flat one involving noise. On the other hand, if the temporal shape of the signals is dependent upon their spatial location, the ratio image displays variations in intensity. A pixel value for $D_{12}^{Exp}(x, y)$ can be described mathematically, by use of Equation 4.4 as

$$D_{12}^{Sim} = \frac{\int S(t) \cdot G_1(t - \Delta t_1 - \delta) dt}{\int S(t) \cdot \left[\begin{array}{c} G_1(t - \Delta t_1 - \delta) \\ + G_2(t - \Delta t_2 - \delta) \end{array} \right] dt}. \quad (6.19)$$

If the measurement system is characterized carefully enough, all the parameters in Equation 6.19 are known except for the signal, $S(t)$. Although it is obviously not possible to determine the full temporal shape of the signal by use of Equation 6.19, if the signal is characterized by a single parameter this parameter can be determined under certain circumstances, provided the relationship between this parameter and the ratio is unambiguous.

In order to use Equation 6.19 in its complete form, the following characteristics of the system need to be determined:

- The temporal shapes of the gate functions of the ICCD cameras
- The delay time of the camera in relation to the time of excitation
- The duration of the laser pulse
- The time jitter between the laser pulse and the trigger pulse
- The expected temporal shapes of the signals stemming from the measurement volume

If the temporal shape of the gate functions and their delay times are known, and the time jitter has been determined, or the jitter is very slight and can thus be neglected, the ratio D_{12}^{Sim} can be used for simulations, provided the signal is also known. The ratio can then be calculated by using a library of signals, $(S_1(t), S_2(t), \dots, S_n(t))$ that includes all signal shapes that are expected to be detected

$$\begin{pmatrix} D_{12}^{Sim}(S_1(t)) \\ D_{12}^{Sim}(S_2(t)) \\ \vdots \\ D_{12}^{Sim}(S_n(t)) \end{pmatrix} = \begin{pmatrix} \frac{\int S_1(t) \cdot G_1(t - \Delta t_1 - \delta) dt}{\int S_1(t) \cdot \left[\begin{array}{c} G_1(t - \Delta t_1 - \delta) \\ + G_2(t - \Delta t_1 - \delta) \end{array} \right] dt} \\ \frac{\int S_2(t) \cdot G_1(t - \Delta t_1 - \delta) dt}{\int S_2(t) \cdot \left[\begin{array}{c} G_1(t - \Delta t_1 - \delta) \\ + G_2(t - \Delta t_1 - \delta) \end{array} \right] dt} \\ \vdots \\ \frac{\int S_n(t) \cdot G_1(t - \Delta t_1 - \delta) dt}{\int S_n(t) \cdot \left[\begin{array}{c} G_1(t - \Delta t_1 - \delta) \\ + G_2(t - \Delta t_1 - \delta) \end{array} \right] dt} \end{pmatrix}. \quad (6.20)$$

When there is an unambiguous relationship between D_{12}^{Sim} and τ , which is the parameter that characterizes the signal, a function, $T(D_{12}^{Sim})$ can be formed. If each pixel value in the ratio image is used as input data to the function $T(D_{12}^{Exp}(x, y))$, an image of the parameter of interest, τ , can be formed. In the work presented in the thesis, this parameter is the fluorescence lifetime, but other entities could instead have been used to this end, such as temperature, pressure, etc., as long as the unambiguity requirement is fulfilled.

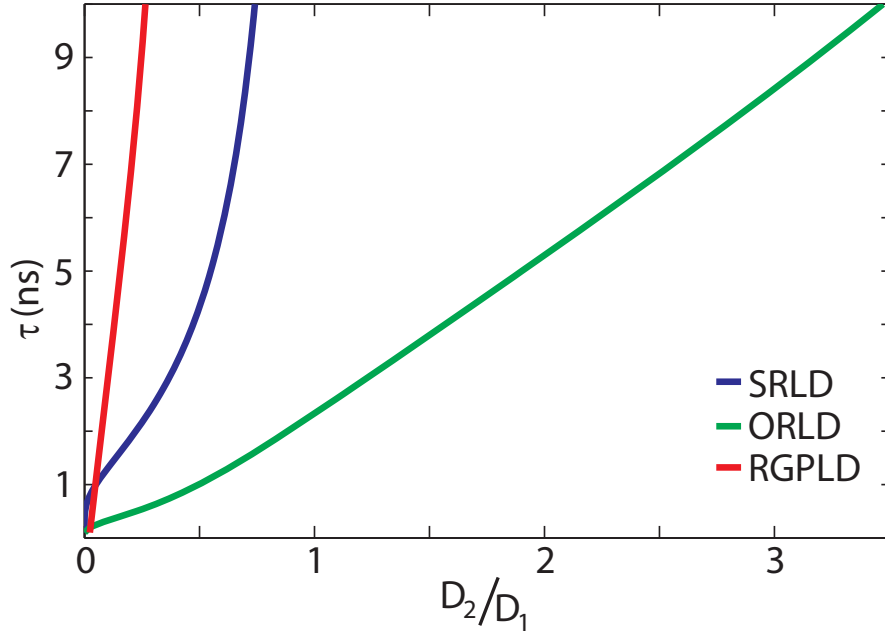


Figure 6.9: *The relationship between τ and the image ratio for each of the three theoretical algorithms. For each of the three algorithms, there is only one ratio value that corresponds to one and only one τ , this indicating that each of them can be used within the interval of question.*

For example, the relation between the lifetime and the ratios of the three algorithms to one another shown in Figure 6.9, in which each of the three algorithms fulfills the requirements referred to above, can in theory serve as models for basing the fluorescence lifetime scheme on. An analysis of the ideal lifetime determination schemes can provide guidelines for performing lifetime imaging, this being done best with use of real ICCD cameras. Since the DIME algorithm can be used not only to account for imperfections in the camera gate profiles, but also to utilize the current shape for these functions, other more sensitive detector schemes can be used for performing fluorescence lifetime imaging. In Papers V, VI and VII, the use of DIME for accumulated and single-shot measurements was demonstrated.

Some work has been initiated to extend this to multiple parameter determination. However, there are reasons to doubt that the very challenging task carrying on such work to its completion would not be worth the effort, at the moment, at least, since simpler schemes, such as that of the camera gate function being delayed sequentially across the signals as a whole in equidistant steps [59], [60] can be expected to provide the same information. Such a sequential stepping procedure places strong demands on the intensifier, which should best have a narrow gate and a well controlled delay. Also, narrow gates have the drawback of possessing poor photon economy, this making the detector scheme very ineffective. Therefore, a more effective measurement scheme based on Multiple Imaging and Modeling Evaluation, can be fruitful to use here if the improvement this provides is found to be sufficiently great compared with other schemes.

6.2.1 Single shot accuracy and precision

Single-shot results obtained in a toluene-seeded gas jet with a surrounding co-flow for the determination of fluorescence lifetimes were tested. The same gas mixture of nitrogen and oxygen was used for both the jet and the co-flow, except that in the case of the jet the gas mixture was sent through a bubble bottle containing liquid toluene before it was ejected.

The experimental setup shown in Figure 6.10, consisted in parts of a quadrupled picosecond Nd:YAG laser that generated laser pulses having a pulse width of 30 ps and a wavelength of 266 nm, and two ICCD cameras, the one being a typical camera of this sort and the other being one with a short gate option, the gate having a temporal width of roughly 2 ns. The jitter was logged for every laser shot. Validation measurements were conducted using a streak camera for measuring the temporally and spatially resolved fluorescence signals along a vertical line across the jet structure. The jet flow was run under laminar conditions so as to minimize fluctuations in the single shot data used to determine the mean and the standard deviation of the fluorescence lifetimes that were registered. The results obtained are shown in Figure 6.11 which shows there to have close agreement between the evaluated data acquired by the streak camera and by the ICCD cameras.

In order to separate the shot-to-shot fluctuations from fluctuations in the image noise, a well-defined area ($n \times m$) in the center of the jet flow was analyzed for an N number of single-shot images, $\tau_i(x, y)$. The standard deviation of the image noise, as well as of the noise of the shot-to-shot

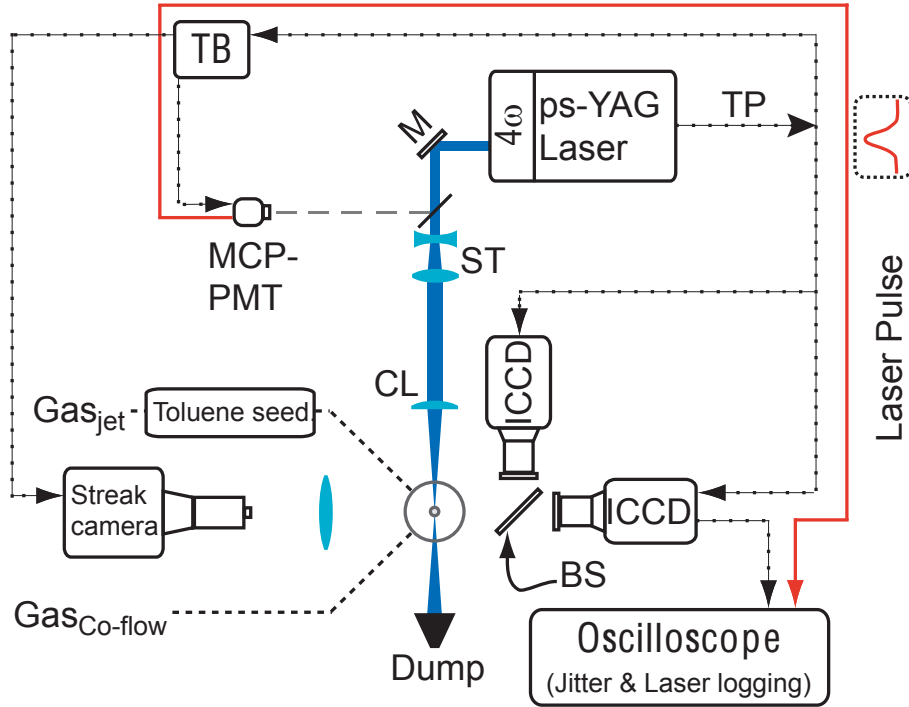


Figure 6.10: The experimental setup employed for measuring the accuracy and precision of fluorescence lifetime determination, by use of DIME.

fluctuations for one pixel was determined for each of the single frames:

$$\mu_{\tau}(x, y) = \frac{1}{N} \sum_{i=1}^N \tau_i(x, y) \quad (6.21)$$

$$\sigma_{tot}^2(x, y) = \frac{1}{N} \sum_{i=1}^N (\tau_i(x, y) - \mu_{\tau}(x, y))^2. \quad (6.22)$$

The mean value of the pixels in the area was obtained to assess the image noise. The mean background had to be subtracted first, however, since there was a systematic error in the images:

$$\mu_{\tau_i} = \frac{1}{n \times m} \sum_{(x,y)=(1,1)}^{(n,m)} \tau_i(x, y) \quad (6.23)$$

$$\sigma_{image,i}^2 = \frac{1}{n \times m} \sum_{(x,y)=(1,1)}^{(n,m)} (\tau_i(x, y) - \mu_{\tau}(x, y) - \mu_{\tau_i})^2. \quad (6.24)$$

The mean values for the image statistics could then be calculated from the set of single-shot images. Since the image noise and the shot-to-shot fluctu-

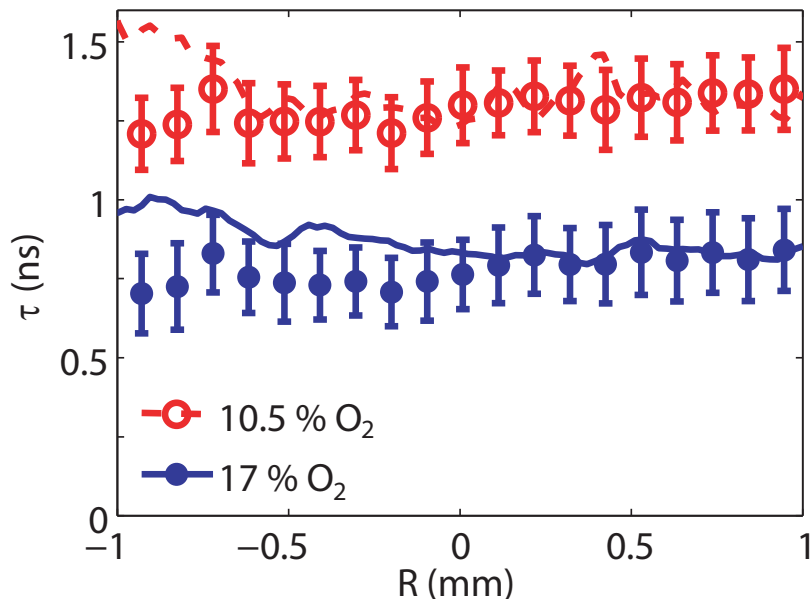


Figure 6.11: Evaluated lifetimes of toluene fluorescence along a line that goes across the toluene seeded gas jet. Data for two different N_2/O_2 mixtures was collected with use of a streak camera and of dual ICCD cameras. The accumulated streak camera data was evaluated by means of line fitting, this being displayed as lines, whereas the data acquired by use of the two streak cameras were analyzed using the DIME algorithm, as shown by the circles.

ations were independent of one another, the shot-to-shot fluctuations could be calculated as

$$\sigma_{s-s}(x, y) = \sqrt{\sigma_{tot}(x, y)^2 - \bar{\sigma}_{image}^2}. \quad (6.25)$$

In Paper VI the total noise was found to be at a level of around 120 ps, the image noise at around 100 ps and the shot-to-shot noise at around 70 ps, which was less than 10 % of the mean values obtained.

Chapter 7

Quantitative imaging

THIS chapter includes some of the experimental results reported in the papers that the thesis is built up around. The first result to be considered represents an example of absorption being used to perform quantitative concentration measurements using Light Detection And Ranging (LIDAR). In the two sections that follow, laser-induced fluorescence signals were used for determining both quantitative and qualitative PLIF images. For a more detailed account of the results, the individual papers should be consulted (Papers II, III, V, VI, VII, IX).

7.1 Differential Absorption LIDAR (DIAL)

LIDAR (LIght Detection And Ranging) involving use of nanosecond laser pulses has been successfully demonstrated earlier and been applied in atmospheric research [61], for example. For LIDAR investigations inside combustion devices, such as in power plants, boilers and the like, higher spatial resolution is needed, since the measurement objects involved have relatively small geometries. Such spatial resolution can be achieved by use of picosecond laser pulses and fast detectors, such as streak cameras or MCP-PMTs. In performing LIDAR, the optical axis of the propagating laser beam and the collection optics are usually aligned. The detection optics collects the light that is scattered, emitted or reflected, in the backward direction in reference to the direction of laser propagation. For measurements of this sort, a picosecond laser was used as the laser source, the detector being a streak camera, the latter having the ability to temporally resolve the signal. The elastically backscattered signal was studied as a function of time, providing information about the scattered intensity versus distance from the detector. Through tuning the wavelength of the laser to an absorption line of a

given molecule as the backscattered signal was being acquired, the decrease in laser intensity as the laser was being absorbed by the molecule could be detected. Yet the backscattered signal is dependent upon a considerable number of additional parameters, making the absorption dip extremely difficult to evaluate. Obtaining a reference measurement when the wavelength was tuned off the absorption line, however, enabled a ratio to be formed allowing the number density of the absorbing species to be expressed as

$$N(R) = \frac{1}{2(\sigma(\lambda_1) - \sigma(\lambda_2))} \frac{d P_{\nu_1}(R)}{dR P_{\nu_2}(R)}. \quad (7.1)$$

Here, $\sigma(\lambda_i)$ is the absorption cross-section of the two different wavelengths of the absorbing species, the last part in the expression being the derivative of the ratio of the one signal to the other with respect to the distance, R . This experimental scheme is commonly referred to as DIAL (Differential Absorption LIDAR).

7.1.1 DIAL Experimental Arrangement

The near-field LIDAR approach was demonstrated for the quantitative concentration determination of acetone using 266 nm light, for which the absorption cross-section of acetone is rather high ($4.36 \cdot 10^{-20}$ cm²), one which is insignificant in case of 532 nm. Since both 532 and 266 nm laser wavelengths were used, dual pathways aligned with mirrors coated for 266 and 532 nm, respectively, were formed. The measurement setup in this particular experiment is shown in Figure 7.1. The laser light was collected by an achromatic quartz lens. Such a lens enables the light to be focused onto an entrance slit of a spectrometer, independent of the wavelength. The spectrometer as the role of effectively separating the acetone fluorescence signal that is induced from the scattered laser light before it hits the entrance slit of the streak camera. The measurement objects are two bubbler bottles filled with acetone that direct acetone-seeded gas flows vertically into the measurement volume. The opening of each bottle is 2 cm in diameter, the internal distance between the bottles being 40 cm.

7.1.2 DIAL Results

The accumulated data were acquired by the streak camera, Equation 7.1 being employed here. LIDAR signals recorded for 266 and 532 nm excitation are shown in Figure 7.2a. The ratio of the two signals ($\frac{P_{\nu_1}(R)}{P_{\nu_2}(R)}$) can be seen in the plot below (7.2b), in which the effects of absorption appear as abrupt steps. The number density of acetone molecules above the bubbler bottles could be determined by use of Equation 7.1. The results obtained were

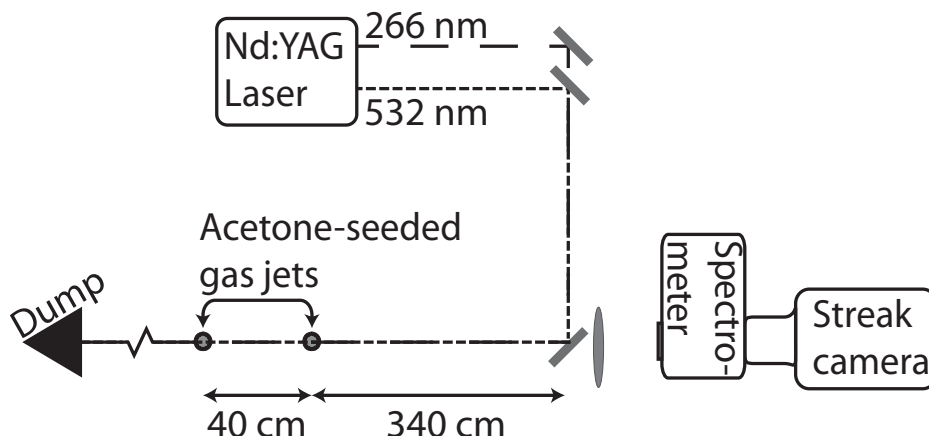


Figure 7.1: *The experimental setup of DIAL. Two laser beams overlap and are aligned to the optical axis of the collector lens and to the entrance slit of the spectrometer. Two vertically directed acetone-seeded gas flows are located in the laser path, the 266 nm laser beam being absorbed, whereas the 532 nm laser beam is not. The number density of the acetone above the jets could be determined on the basis of Equation 7.1.*

$1.7 \cdot 10^{18}$ molecules/cm³ at a distance of 340 cm and $2.5 \cdot 10^{18}$ molecules/cm³ at 380 cm, as shown in Figure 7.2c. The 30% difference in number density might well be due to differences in the two acetone vaporization channels, but it could also be an effect of a low signal-to-noise ratio for the signal peak furthest away from the collector lens. The number density obtained seems a bit low as compared with the vapor pressure of acetone in air at room temperature, which is $6.6 \cdot 10^{18}$ molecules/cm³ [62]. Nevertheless, the probe volume is located well above the flask opening, this most likely producing a flow possessing turbulent characteristics. Such turbulence lowers the average number density in the probe volume.

7.2 Visualization of nitric oxide concentration using Planar Laser Induced Fluorescence

NO is a molecule which has been investigated by use of lasers for various reasons over the years. *NO* is of interest first and foremost because of its being a rather simple molecule, which is attractive in the work of theoretical modeling. Such modeling work has provided experimentalists software packages for data evaluation [63], [64]. These software tools have been used for multi-line fitting for determining temperatures [65], for example. *NO* is a toxic product in combustion processes, one that could be taken care of by means of flue gas treatment. It is not possible, however, to reduce the presence of *NO* by use of scrubbing processes, but ozone molecules (*O*₃) are

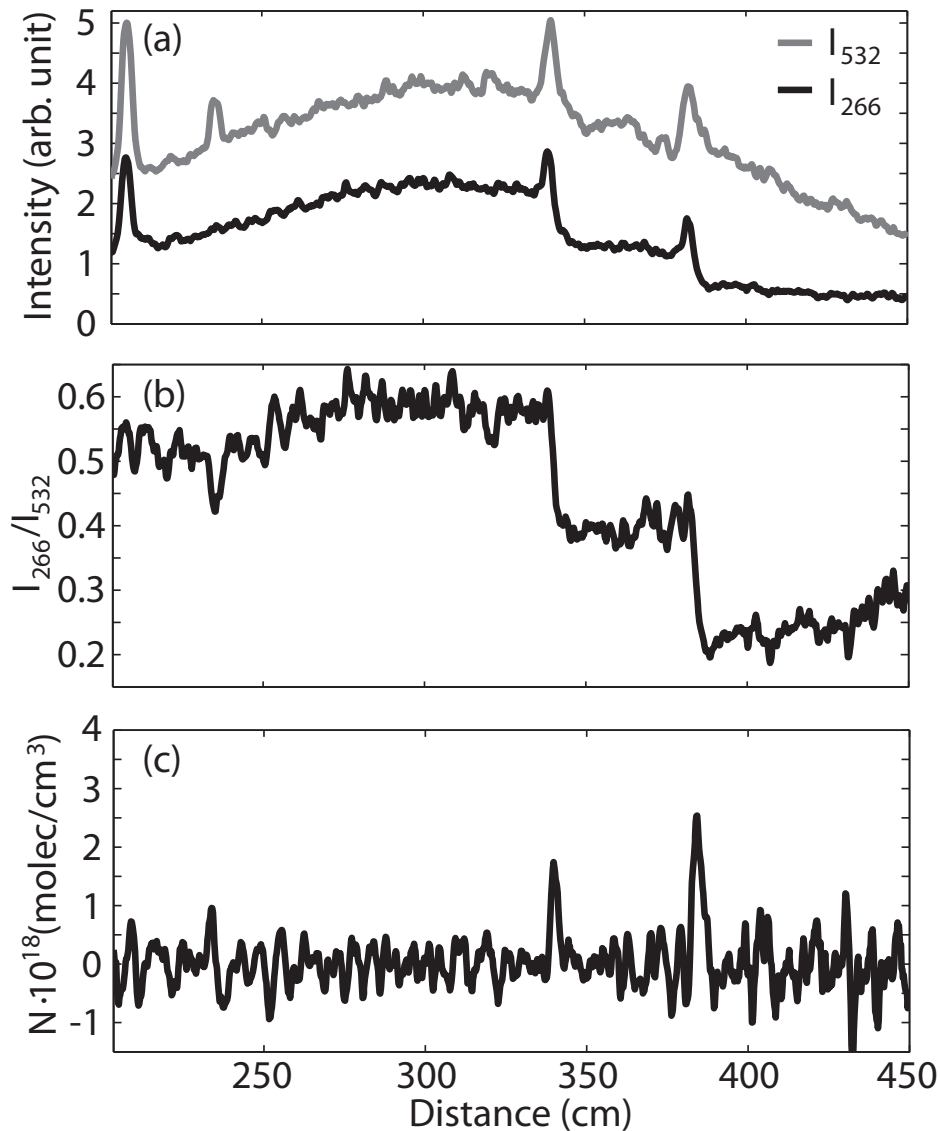


Figure 7.2: Spatially resolved determination of the acetone concentration, using DIAL. (a) The two backscattered signals from 266 nm and 532 nm are shown as a function of distance. (b) the signal ratio of the two signals in (a), the absorption by the two acetone sources being shown by the abrupt steps in the curve. (c) through use of Equation 7.1, the spatially resolved number density of the acetone could be determined for each of the two acetone sources, which are visible here as the two clear peaks located at ~ 340 cm and ~ 380 cm.

known for oxidizing NO molecules into NO_2 [66]. In contrast to NO , NO_2 is effectively removed by wet scrubbing systems.

7.2.1 NO-PLIF Experimental Arrangement

In order to test whether the injection of ozone facilitates the oxidation of NO into NO_2 , use was made of a concentric flow system in which the surrounding co-flow was synthetic flue gas and the jet flow in the center was air containing varying amounts of ozone. A schematic image of the experimental setup is shown in Figure 7.3. The excitation wavelength of NO -PLIF was generated from the fundamental beam (1064nm) by means of a Q- switched Nd:YAG laser and a dye laser having LDS 698 dye. The output of the dye laser (pumped by 532 nm) was tuned and was frequency doubled so as to generate 339.38 nm laser light. A retardation plate (RP) was used to optimize phase matching of the doubled dye laser beam and the fundamental Nd:YAG (1064 nm) in a third harmonic generation (THG) crystal, which provided a wavelength of 226.25 nm. A Pellin-Broca (PB) prism was used to separate the beams. A laser sheet was formed using two quartz lenses (CL and SL) that provided PLIF images of NO in the measurement volume.

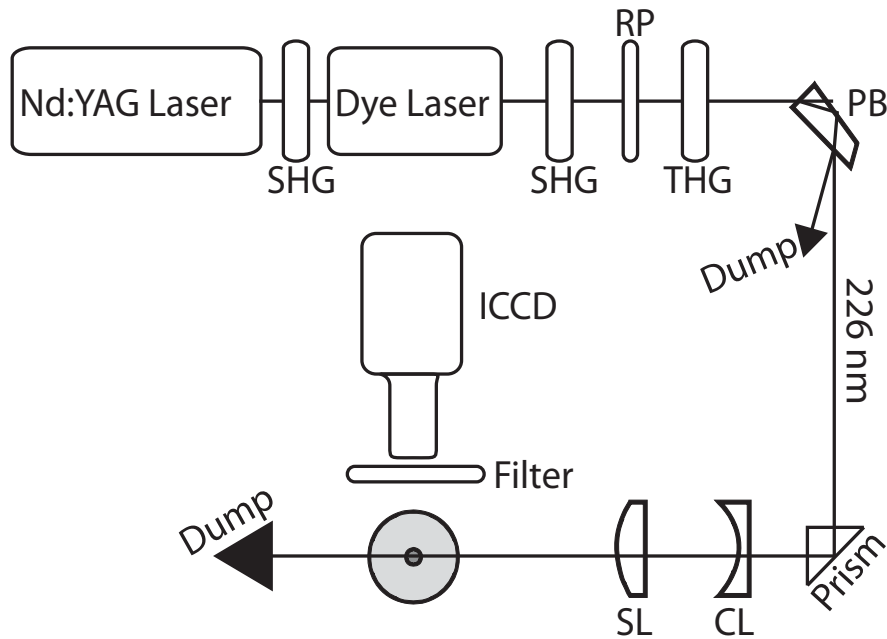


Figure 7.3: *Experimental setup used in NO PLIF. SHG is second harmonic generation, RP is retardation plate, THG is third harmonic generation, PB is the Pellin Broca prism, and CL and SL are a cylindrical and a spherical lens, respectively.*

7.2.2 NO-PLIF Results

The measurement volume was imaged at three different heights by adjusting the height of the flow system with respect to the position of the laser beam.

Three such images are shown in Figure 7.4, the left image being of data from acquisition without ozone being present in the jet flow, so that the oxidation of NO to NO_2 by ozone did not occur. As ozone was seeded into the flow, the signal was reduced in the interface between the jet and the co-flow, as shown in the figure in the middle. The difference between the two images can be seen at the right, where a clear signal shows where the reaction zone would be. Since the concentration of NO as it enters the probe volume (at the bottom) is known the concentration of NO can be determined in the image as a whole by simply relating the signal intensity to the concentration. A few assumptions need to be made, however.

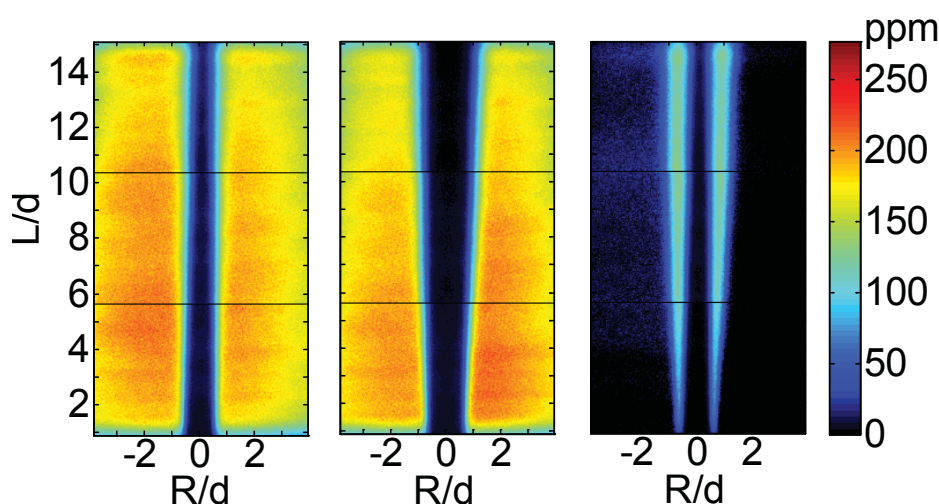


Figure 7.4: Concentration images of NO . The left image shows the NO concentration in the center flow without the presence of ozone, whereas in the image in the middle ozone has been injected into the center flow. The image at the right shows the difference, evident in the reaction zone when NO has been oxidized to NO_2 .

First, it needs to be assumed that the fluence of laser is sufficiently low for saturation effects to be avoided. This was arranged for by using a lens of rather long focal length, providing excitation in the linear regime across the entire laser sheet. Second, the number density of NO needs to be sufficiently low for absorption effects as the laser propagates across the measurement volume to be avoided and to prevent signal trapping from occurring. Assuming this to be the case appears justified since there is no obvious absorption gradient to be seen in the images. Third, variations both in temperature and in quenching are neglected. Temperature variations affect the absorption linewidth, which makes the spectral overlap function temperature-dependent. Also, the population distribution of the NO molecules is affected by the temperature. In the measurements con-

ducted here, the temperature variations within the image of about 25-150°C at the most are rather small. Thus, temperature effects on the linewidths and on the population distributions of the *NO* molecules are only minimal. Finally, any appreciable differences in collisional quenching in the reaction zone would be due to additional ozone being seeded into the co-flow. The quenching rates for ozone were not found in the literature, but with the very modest concentrations of it at around 0.2 %, as compared with ~20 % for oxygen, it appeared that errors due to differences in quenching could be neglected. Based on the assumptions made, the two-dimensional concentration images shown in Figure 7.4 can be considered to be fairly accurate. The major sources of uncertainty regarding the absolute values of the concentrations of *NO* would be fluctuations in the gas compositions, the laser pulse energies and the spatial profile of the laser sheet.

7.3 Fluorescence Lifetime Imaging Measurements

As mentioned in Chapter 3, fluorescence signals have a temporal decay which in many cases is due to collisional quenching. The evaluation scheme DIME, presented in Chapter 6, was used for measuring fluorescence lifetimes in two dimensions. The oxygen concentrations can be determined on the basis of the lifetime of the toluene fluorescence, fluorescence lifetime imaging being performed in flows having controlled colliding partners. The aim of such measurements was to be able to study the mixing occurring in model flows in order to validate simulations, such as studies in [70].

7.3.1 Single-shot FLI of sub-nanosecond lifetimes

The measurement setup used to determine fluorescence lifetimes in two dimensions is shown in Figure 6.10. Dual images could be obtained using a dual camera setup to perform fluorescence lifetime imaging, two cameras being employed to extract a fluorescence lifetime image in a single-shot measurement. The measurement object was a toluene-seeded gas jet (N_2/O_2) having a nitrogen co-flow surrounding it. Two images captured from a single laser excitation are shown in Figure 7.5, along with a fluorescence lifetime image. Even though the PLIF images may at a first glance look similar, there are clear differences, which are accentuated in the outer turbulent structures downstream. There, the nitrogen is mixed with the toluene-seeded gas flow. The mixing dilutes the oxygen concentration, resulting in longer fluorescence lifetimes.

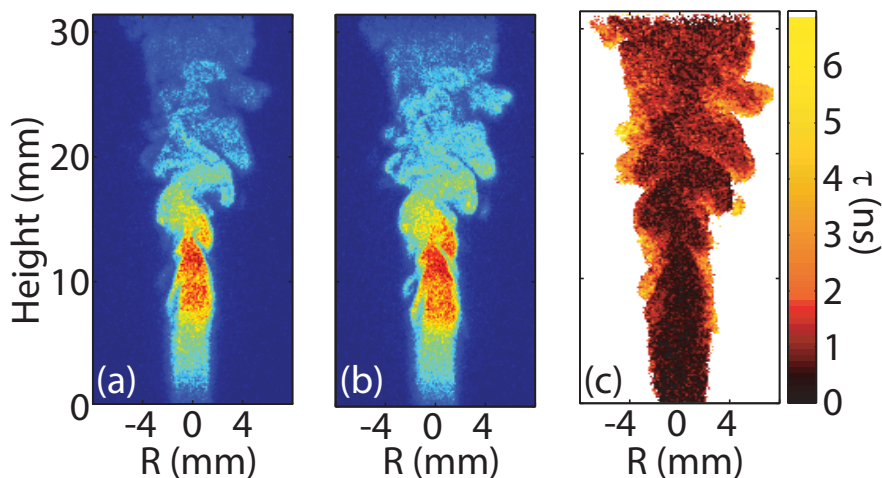


Figure 7.5: Images (a) and (b) are single-shot images acquired by the two cameras. (c) The fluorescence lifetime image determined by use of the DIME algorithm.

7.3.2 Quenching corrected PLIF of formaldehyde in a flame

Formaldehyde (CH_2O) is an intermediate species in hydrocarbon combustion [67]. PLIF imaging of formaldehyde in a flame displaying a well defined signal since formaldehyde is formed at temperatures of around 750 K, whereas it is consumed at higher temperatures [68]. Still, formaldehyde is to be found in regions in which the temperature and species concentration gradients are fairly steep. It might be advantageous, therefore, to correct the formaldehyde PLIF images for differences in the population distribution as well as for variations in the fluorescence quantum yield.

Experimental Arrangement for CH_2O PLIF

Quenching corrections of LIF were performed using the DIME approach presented in Chapter 6. The experimental setup employed is shown in Figure 7.6. A tripled Nd:YAG laser (355 nm) was used for performing the PLIF of CH_2O in a rich methane/oxygen flame. Two ICCD cameras were used for acquiring dual images that could be evaluated using the DIME algorithm, so as to form fluorescence lifetime images of the formaldehyde found in the flame. A beam splitter was used to split the signal and direct them towards the two cameras. Averaged measurements were performed, yet since dual cameras were employed to acquire images from the same laser excitations the fluctuations in laser energies cancel out.

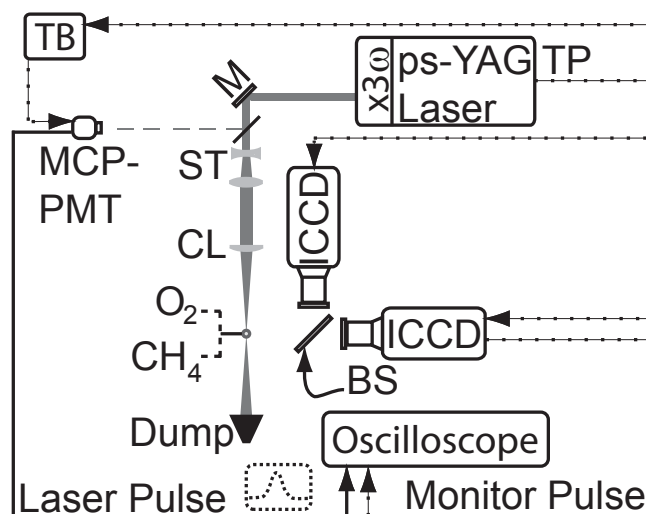


Figure 7.6: *Experimental setup for the PLIF imaging of formaldehyde in a methane/oxygen flame, the data being corrected for differences in the fluorescence quantum yield and the population distributions.*

Results for CH_2O PLIF

The results obtained are shown in Figure 7.7. A raw-data PLIF image of formaldehyde is shown in (a). A double-peak structure in the formaldehyde signal across the flame front can be noticed. The temperature data were obtained by performing Rayleigh measurements, the results being shown in Figure 7.7b. A fluorescence lifetime image of formaldehyde was obtained using the DIME algorithm for analyzing two PLIF images, acquired by two separate cameras. A double peak structure, similar to the formaldehyde PLIF image can be seen in the fluorescence lifetime image across the reaction zone as well. The PLIF image was corrected for inhomogeneities in the laser profile, as well as for differences in the fluorescence quantum yield and for temperature effects in the population distribution [69]. A corrected PLIF image is shown in Figure 7.7d, in which the double peak was canceled as the data was being corrected for quantum yield. An artifact can be seen in the center of the flame. The fluorescence lifetime imaging that was performed showed there to be very short lifetimes in the center, due to the instantaneous vibrational Raman scattering of methane there.

7.3.3 Oxygen concentration measurements

Prior to the present investigation, there had been few investigations that provided data on this matter. Koban et al. [71] presented a phenomenological model that predicted the fluorescence quantum yield for known temperatures and known partial pressures of oxygen in case of 266 nm excitation.

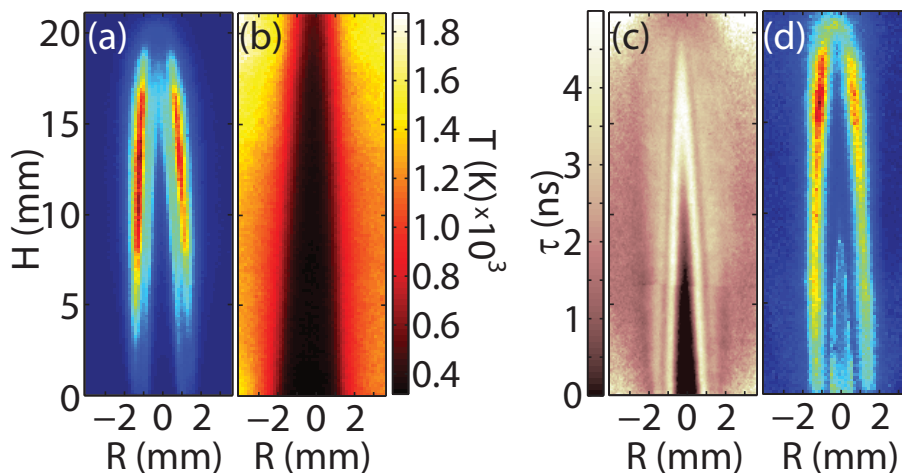


Figure 7.7: *PLIF of CH_2O , temperature, fluorescence lifetime and a corrected PLIF image of CH_2O . (a) Raw-data PLIF image of formaldehyde in the flame. (b) Temperature data from Rayleigh measurements. (c) Fluorescence lifetime image of formaldehyde. (d) PLIF image corrected for, the laser profile, differences in fluorescence quantum yield and temperature effects in the population distribution.*

The phenomenological model presented by Koban et al. could be used to determine partial pressures of oxygen on the basis of fluorescence lifetime measurements, using fluorescence-lifetime data obtained at known oxygen concentrations [72]. In a recent publication by Faust et al. [73], the model of Koban et al. was validated at atmospheric pressure for different oxygen concentrations and different temperatures. Rather than drawing conclusions here on the basis of this phenomenological study, a physical model was used to assess in a straightforward way how the partial pressure of oxygen and the fluorescence lifetime were related. This model employed, termed the Stern-Volmer relation [74], provides a description of the radiation-free deexcitation pathway that collisions of the excited molecules with the surrounding quencher molecules follows.

Temporally resolved toluene fluorescence measurements were performed using pico second excitation (266 nm), a streak camera being employed for measuring the shorter lifetimes, and an MCP-PMT for determining the longer lifetimes. The reason for not using the streak camera for measuring longer fluorescence lifetimes was that the streak unit on the camera that was available had a maximum temporal window of 20 ns, which is too small, since the longest lifetime that was measured was longer than 40 ns. The results are displayed in Figure 7.8, the relationship found between the oxygen concentration and the fluorescence lifetime being well described by the Stern-Volmer relation. It is useful to know the mathematical description of

the relationship, which is

$$[O_2] = k\tau^{-1} + m, \quad (7.2)$$

where k and m are $5.53 \cdot 10^{-9}$ and -0.127 , respectively.

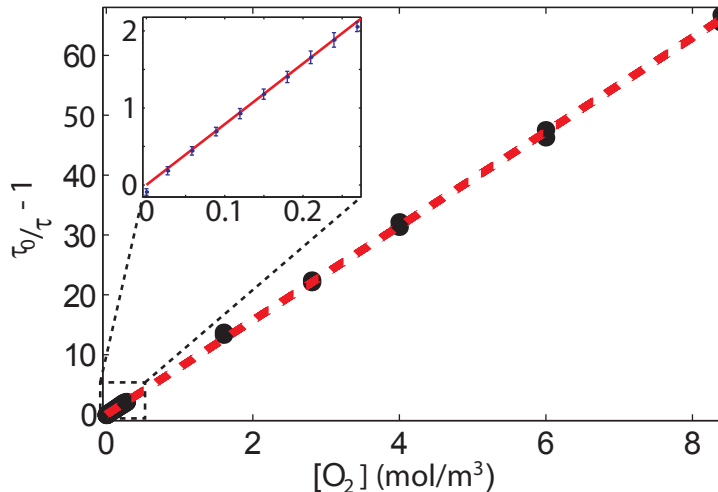


Figure 7.8: *The relationship between the partial pressure of oxygen and the fluorescence lifetime of toluene.*

7.4 Quantitative measurements in scattering environments

In performing PLIF experiments under realistic measurement conditions, problems that arise can in some cases degrade the imaging quality. Such degradation factors can be those, for example, of multiple scattering, interfering fluorescence, and stray light. If such interferences are introduced outside the focal plane, where the laser sheet is located they can be discriminated by using a scheme termed structured laser illumination planar imaging (SLIPI). Similar investigations have been performed in microscopy [75], [76]. There, however, the laser illuminates the sample perpendicular to the surface instead of from the side, as in PLIF imaging. Thus, spatial modulation can be utilized to image a section of illuminated volume. This modulation scheme is commonly referred to as optical sectioning, but the same evaluation scheme is performed as in SLIPI. The fluorescence lifetime scheme used by Cole et al. [75] and by Webb et al. [76] is based on multiple image acquisitions having differing delay times. The present investigation was performed using DIME, the current shape of the gate function being accounted for and utilized there. This was a reason for the combination of

these two schemes, which enables fluorescence lifetime imaging under harsh measurement conditions.

A straightforward, overall description of the scheme could be that it involves subtraction of the out of plane background. In performing SLIPI, the fluence of the laser sheet is modulated spatially by a sine wave, producing stripes on the laser sheet. Three separate PLIF images of the measurement object were acquired, using the modulated laser sheet. These images were obtained using a 120° internal phase shift (0°, 120° and 240°) of the spatial sine modulation, this enabling the acquired image to be expressed as

$$I_i(x, y) = I_{bkg} + I_S \cos(2\pi\nu y + \phi_i). \quad (7.3)$$

A background-subtracted image was found by taking account of the three images, I_{0° , I_{120° and I_{240° , in the mathematic expression

$$I_S(x, y) = \sqrt{\begin{bmatrix} (I_0(x, y) - I_{120}(x, y))^2 \\ + (I_{120}(x, y) - I_{240}(x, y))^2 \\ + (I_{240}(x, y) - I_0(x, y))^2 \end{bmatrix}}. \quad (7.4)$$

More thorough accounts of the scheme are to be found in [12] and [77], for example. The experimental setup used in performing SLIPI in PLIF is shown in Figure 7.9.

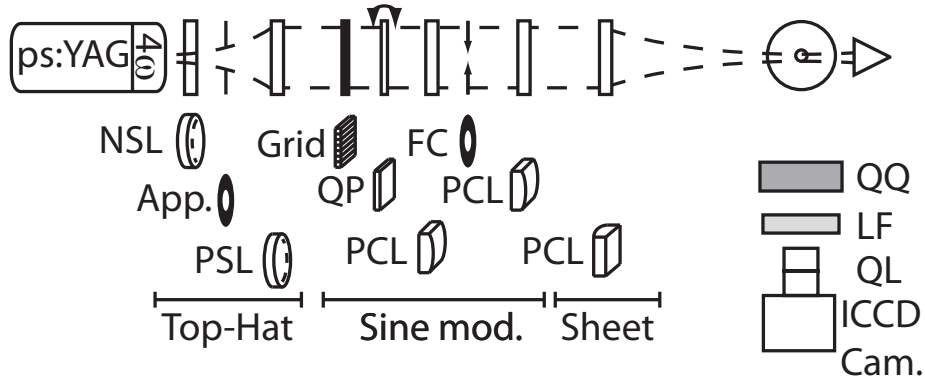


Figure 7.9: The experimental setup for combined measurements of SLIPI and FLI. The different lenses involved are a negative spherical lens (NSL), a positive spherical lens (PSL) and a positive cylindrical lens (PCL). The quartz plate is QP, QQ being the quartz cuvette and QL the quartz lens used on the ICCD camera.

The laser source is a quadrupled picosecond Nd:YAG laser delivering 266 nm light. A top-hat laser profile is formed by a two-lens telescope arrangement that has an aperture. A square-wave modulation of the laser sheet is

formed from a grid, this being followed by use of a quartz plate to introduce the 120° phase shift between the images. The sine wave modulation is formed using two lenses and a frequency cutter to cut out the overtones in the square-wave modulation. Finally, a laser sheet is formed using a cylindrical quartz lens, which focuses the laser within the measurement volume. The measurement object is a toluene-seeded gas jet and a co-flow of differing oxygen concentrations, this resulting in different toluene fluorescence lifetimes. The imaging is performed using an ICCD camera. In order to simulate imaging through scattering media, a quartz quvette containing a mixture of water and polystyrene spheres is placed between the camera and the measurement volume. The optical density of the scattering medium is 2.3, which means that roughly 10 % of the photons transmitted through the polystyrene/water solution are detected by the camera without being scattered once.

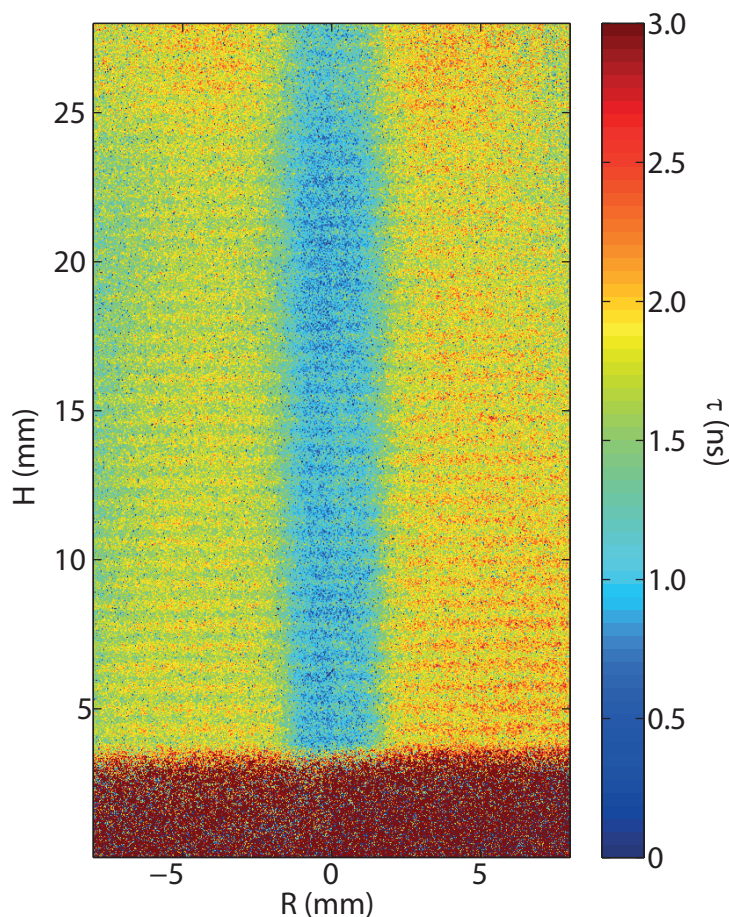


Figure 7.10: A fluorescence lifetime image of the jet flows obtained after use of the SLIPI algorithm.

The results of the accumulation are shown in Figure 7.10. The red area at the bottom of the image is not excited by the laser sheet, these values thus having no physical meaning. The center of the image displays fluorescence lifetime values that are lower than those in the co-flow. The fluorescence lifetime in the center jet, which makes use of air, should be at around 650 ps, whereas the lifetime in the co-flow should be at around 1.7-1.9 ns. There still are some stripes visible in the raw-data image after the three acquired images in the SLIPI algorithm have been combined. It would be possible to filter the image by use of some smoothing algorithm having a filter matrix able to average the stripes. This is evident in the cross-sectional data displayed in Figure 7.11, in which the averaged data, shown as a red curve, is presented along with data that were corrected for out-of-plane luminescence by use of the SLIPI algorithm, the latter set of data being displayed as a blue curve. The discrimination of the multiple scattered photons enables the photons of interest to be imaged at their source. Thus, determination of the fluorescence lifetime is fairly accurate for the data in which multiple scattering has been suppressed. The spikes seen in the blue spectrum is due to cosmic rays.

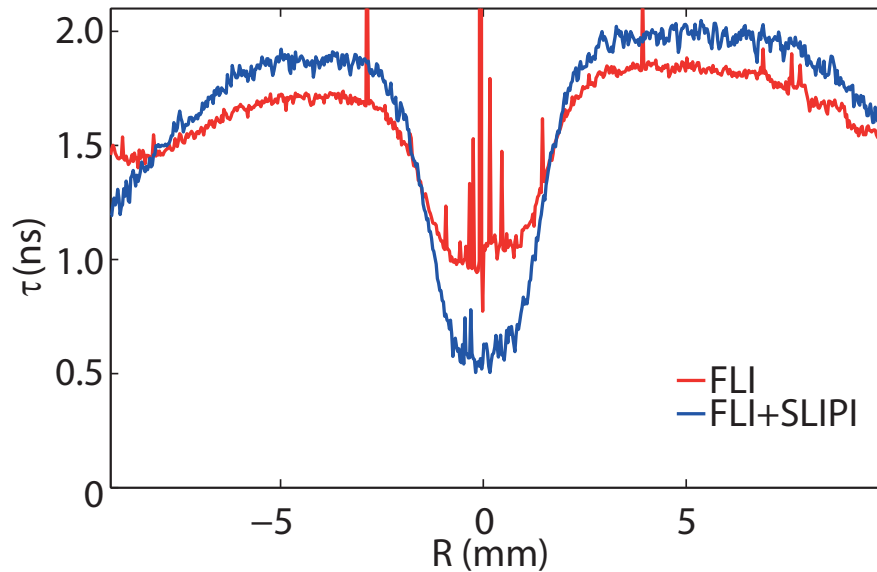


Figure 7.11: A cross-section of two fluorescence lifetime images, in one of which the out-of-plane background has been removed through performing SLIPI (blue), in the other conventional averaging having been performed (red).

Note that in performing fluorescence lifetime imaging in combination with SLIPI several acquisitions need to be performed. Also, the fact that scattered light is being removed makes the signal-to-noise ratio critical, so that averaging needs to be performed. If there are fluctuations of the lifetime

of the fluorescence signal that is imaged in a given pixel, the resulting signal is multi-exponential. This is a well-known problem that places limitations on the combining of SLIPI and DIME, since averaging needs to be performed. Nevertheless, the combining of SLIPI and DIME is useful when rather stable conditions are present, or when differences in fluorescence lifetime can be a help in distinguishing various processes.

Chapter 8

Conclusion

IN concluding what has been taken up in the thesis, it is to be noted that several laser-based diagnostic schemes were developed that appear to be potentially useful in a number of applied research fields that utilize laser induced fluorescence and molecular scattering, and that uses to which they can be put having been demonstrated. The major contributions of the work appear to be the following:

- The work on temporal filtering reported on provides a model that can be used to evaluate the filter efficiency of a measurement system in a given measurement situation. The important parameters were identified and investigated, and certain guidelines for performing temporal filtering, both connection with fluorescence and in Raman studies, were provided.
- Dual Imaging with Modeling Evaluation able to provide the possibility of determining the temporal shapes of signals was developed. The scheme in question was employed in fluorescence lifetime imaging, in quenching-corrected PLIF, as well as oxygen concentration measurements in model flows. The scheme was found to work in combination with SLIPI, this opening up possibilities of using it for quantitative measurements in harsh environments, where its use can serve to suppress both multiple scattering and interfering, out-of-plane fluorescence.
- A lifetime determination algorithm, referred to as Ramped Gain Profile-Lifetime Determination (RGP-LD) was proposed for use in combination with DIME for providing better sensitivity and better detection efficiency than traditional rapid lifetime determination schemes provide.

- The development of picosecond LIDAR having high spatial resolution was described as being a first step in making single-ended measurements in stationary power plants, for example, possible. Differential Absorption LIDAR, together with Rayleigh temperature and soot mapping approaches that could provide support for this were developed.
- The pilot study together with Professor Wang (III) in which ozone was used in the oxidation process of NO to NO_2 was followed up by professor Wang's implementing the technique in a power plant in China for reduction of NO_x emission.
- Finally, work on the imaging of different species by means of photo-fragmentation LIF showed that it provided the possibility to obtaining images of peroxide molecules in flames of a variety of different types. Since the species investigated had no electronic transition that could provide irradiation, the new approach developed here was seen to open up the possibility of gaining a better understanding of combustion processes generally in this way and of providing data useful for modeling of combustion.

Chapter 9

Outlook

THE title of the thesis indicates that the intention of the work undertaken was to provide tools and ideas for better quantification of data in this area. High-end equipment was used to develop and demonstrate schemes that could be of use to other research groups that might not have such equipment at hand. Since the ideas in question are not limited to signals possessing nanosecond characteristics, a first approach could possibly be to use the measurement schemes that were developed for investigating signals having slower time characteristics, traditionally investigated by use of nanosecond lasers, concerning such matters as laser induced incandescence (LII) and phosphor signals. In such studies, use can be made of off-the-shelf excitation and detection systems, approaches that in the form considered here could be useful within a broader area of research.

A second approach that could be taken concerns the fact that the generic conceptions developed and tested here pertaining to rapid excitation and detection appeared to be potentially useful in a wide variety of applications. It could be worth while, for example, to investigate the possibility of developing schemes involving use of nanosecond pulses. Lasers with longer pulse duration might also be of interest for serving as tools if the pulses in question were possible to modulate. Introducing the frequency dimension in connection with the determination of the temporal characteristics of signals could possibly open up new possibilities for obtaining more accurate qualitative and quantitative measurements for a number of molecules of interest in combustion.

A third approach would be to explore the possibility of various applications in which new tools related to the work reported here could be used

to provide more detailed information. Obviously, the calculation of fluorescence quantum yields for PLIF images, for example, would be beneficial in terms of the possibilities it could create of acquiring better quantitative and qualitative images, especially in the case of combustion in which the species of interest are located in the reaction zone, where collisional quenching varies spatially due to steep temperature and concentration gradients. Also, even if collisional quenching is dependent upon a number of different parameters, the fluorescence lifetime could be of particular interest in itself, especially since kinetic-modeling results could be used for calculating the expected fluorescence lifetimes of fluorescent molecules (similar to what was done in Paper IV). In addition, scientific fields in which lower temperatures and less complex chemistry are involved than here, could clearly benefit from this work, this applying to such fields as

- Applied Catalysis
- Epitaxial Growth Chemistry
- Mixing Studies
- Spray Studies

The temporal domain could serve as a tool there for distinguishing between the liquid and the gas phase, and between various molecules that are excited simultaneously, for the estimation of temperatures, for quantitative concentration measurements, for perform measurements close to surfaces and the like.

Finally, a patent on RGP-DIME is pending and we are involved in discussions with developers of fluorescence lifetime microscopy systems. We hope that our work will be implemented in commercial systems and that such products will also be of benefit to research that is outside of my own area of competence. I hope that in the future a commercial imaging system will be available for temporal studies of signals of relevance to applied energy science.

Acknowledgements

THERE are so many people I would like to thank for the support I have received over the years. I have had the opportunity to work with scientists of world class, all of whom I found to be fascinating persons with lots of ideas and a great deal of heart. In a very deep sense, I could never do justice to my feelings about any or all of you in only a few sentences, but at least I will try.

I would like to first thank my advisor, **Marcus Aldén**, who always stood up for, believed in, and supported me in this work. You have been a true source of inspiration, not only as a scientist and as a manager, but also as a fair and generous person. Without your help this book would never have been written.

Another person that I have a lot to thank for is my first advisor, **Mark Linne**. I miss our trips to Denmark (once towards Germany as we forgot to turn right) and our discussions about whatever came up in the car, at dinner or at a bar/poster-session. Your stubbornness and brilliance as a scientist have helped me understand what it takes to be the best.

The third person who has made my PhD journey outstanding is my co-advisor **Joakim Bood**. As we started sharing an office at the beginning of my PhD studies, I knew immediately that I had a good friend in you. When you then became my co-advisor I learned so much from you without your ever asking for anything back. That generosity is reflected in this book, in which every piece of the puzzle that I had the opportunity to try to solve could be traced back to some discussion we had sometime and somewhere. I could never thank you enough for just being who you are, a genuine humanist who always made me feel a bit better than I am.

9. OUTLOOK

In my PhD work I have had the pleasure to work with a number of very smart, helpful and skilled people.

When I was in Denmark I got the chance to work with **Jens Høgh**, who is one of the best guys I have ever met. I would like to thank you for being such a good friend and for the helpfulness you showed when things were tough.

In the laser studies I conducted, I had the opportunity to work with **Dr. Olof Johansson**. Your brilliance is so great that not even you understand it yourself. As you sighed and stated that "either we do it all, or we just go home" has been the driving force that made every thing we did worth doing. Thank you for being one of the most interesting and best friends I could ever ask for.

I have also had the opportunity to work with **Billy Kalvee**, whose never ending supply of "ordvitsar" made the days pass by like the wind. You have a great ability to find new ways of thinking and analyzing things, which I think makes you very unique. Above all, your intellectual mind has made our discussions flowering, and sometimes even obstructive, as we sometimes tried without succeeding to stay focused on the lab. Thanks for your always taking time aside to think things through and for your generosity in sharing your knowledge.

A fascinating friend who helped Olof and me to do things better (or at least a bit differently) is **Andreas Arvidsson**. You are a true friend who makes me laugh when I least expect it. Your curiosity and your insight into the fundamentals of science has made me think in new ways (even though you most of the time were wrong).

One person who has made my world larger and more interesting is my roommate, **Bo Li**. I enjoy your company so much and feel you have been a great inspiration to me over the years. Your ways of handling stress, success, problems and Sweden are very impressive. I know that whatever you throw yourself into you will do your best with and make your part of the world a better place.

In the latter part of my PhD studies I had the pleasure of working with **Elias Kristensson**. Your focus and sharpness opened up my mind to new ways of working. I am very grateful for that. Your work and your success have been very inspiring to me, especially since you always share what you have gained with others.

I would also like to thank **Edouard Berrocal** for being an inspiration and

a great lab partner as we were fighting in the lab for four weeks straight several years ago. The result of that work was a highly valued friendship along with amazing data that will find its way onto paper some day.

I had the benefit too of working with **Malin Jonsson** as she started her PhD studies at the Division. I really appreciate your enthusiasm and hard working spirit, which always makes me enjoy working in the lab with you. It was a memory for life to do the West Coast of US with you and Joakim, even though you spent most of your time asleep in the back of the car.

In the practical work, regarding construction of large scale flow systems and other very expensive stuff, I had the privilege of working with a true genius. **Rutger Lorensen** is a man who just makes things work, and while he is helping you, it is always hilarious. Thanks for showing me how it is done, at half the time and for a third of the cost.

For a period of time I had the opportunity to spend several hours in the lab with **Zhihua Wang** from Zhejiang University. I really appreciate your sense of humor and quick forehand in our table tennis tournaments.

Over the years I got the chance to represent the Division by playing badminton with **Per-Erik Bengtsson** and **Zhongshan Li**. Until I ruined my knee I had the best of times and I really enjoy your company.

In my pursuit of understanding of the world, I was funded by **CECOST** (Center of Combustion Science and Technology), by DALDECS, an advanced grant from the European Research Council (**ERC**), by the **Swedish Energy Agency** and by **SSF** (Swedish Foundation for Strategic Research). These investors made it possible for me to be a part of the **Modeling and Evaluation** group that placed my research in a wider context. I am truly grateful for that.

I can honestly say that there has not been one day of anxiety as I left home for work. This is not only due to the fact that I have found the work stimulating and fun, but also because I appreciate my colleagues, those of you that flew out and those of you who are still here. I think you all know that I enjoy being around you.

I would like to thank my mum, dad and two sisters, who have always been there for me with their love and help.

Finally, I would like to thank my wife Helena for being the best person in the world. You have not only given me the strength and support I needed

9. OUTLOOK

to finish this work, but also the greatest gift a man can ever wish for in Olle and Ester, my two wonders of the world.

Bibliography

- [1] Mainman, T.H. *Stimulated Optical Radiation in Ruby*. Nature, **187**(4736):493–494, 1960.
- [2] Rairoux, P., Schillinger, H., Niedermeier, S., Rodriguez, M., Ronneberger, F., Sauerbrey, R., Stein, B., Waite, D., Wedekind, C., Wille, H., Wöste, L., and Ziener, C. *Remote sensing of the atmosphere using ultrashort laser pulses*. Applied Physics B: Lasers and Optics, **71**:573–580, 2000.
- [3] Moore, D. *Recent Advances in Trace Explosives Detection Instrumentation*. Sensing and Imaging: An International Journal, **8**:9–38, 2007.
- [4] Kusunoki, Y., Imamura, F., Uda, H., Mano, M., and Horai, T. *Early detection of lung cancer with laser-induced fluorescence endoscopy and spectrofluorometry*. CHEST, **118**(6):1776–1782, 2000.
- [5] Olofsson, J., Seyfried, H., Richter, M., Aldén, M., Vressner, A., Hultqvist, A., Johansson, B., and Lombaert, K. *High-Speed LIF Imaging for Cycle-Resolved Formaldehyde Visualization in HCCI Combustion*. SAE Technical Report No. 2005-01-0641, pp. 1–8, 2005.
- [6] Nygren, J., Hult, J., Richter, M., Aldén, M., Christensen, M., Hultqvist, A., and Johansson, B. *Three-dimensional laser induced fluorescence of fuel distributions in an HCCI engine*. Proceedings of the Combustion Institute, **29**(1):679–685, 2002.
- [7] Kaminski, C., Hult, J., and Aldén, M. *High repetition rate planar laser induced fluorescence of OH in a turbulent non-premixed flame*. Applied Physics B: Lasers and Optics, **68**:757–760, 1999.
- [8] Seyfried, H., Olofsson, J., Sjöholm, J., Richter, M., Aldén, M., Vressner, A., Hultqvist, A., and Johansson, B. *High-Speed PLIF Imaging*

- for Investigation of Turbulence Effects on Heat Release Rates in HCCI Combustion*. SAE Technical Report No. 2007-01-0213, pp. 1–9, 2007.
- [9] Guillard, F., Fritzon, R., Revstedt, J., Trägårdh, C., Aldén, M., and Fuchs, L. *Mixing in a confined turbulent impinging jet using planar laser-induced fluorescence*. *Experiments in Fluids*, **25**:143–150, 1998.
- [10] Pomfret, M.B., Owrutsky, J.C., and Walker, R.A. *In Situ Studies of Fuel Oxidation in Solid Oxide Fuel Cells*. *Analytical Chemistry*, **79**(6):2367–2372, 2007.
- [11] Lantz, A., Collin, R., Sjöholm, J., Li, Z.S., Petersson, P., and Aldén, M. *High-Speed Fuel/Hydroxyl Radical Imaging in a Gas Turbine Pilot Burner*. *AIAA Journal*, **50**(4):971–975, 2012.
- [12] Berrocal, E., Kristensson, E., Richter, M., Linne, M., and Aldén, M. *Application of structured illumination for multiple scattering suppression in planar laser imaging of dense sprays*. *Opt. Express*, **16**(22):17870–17881, 2008.
- [13] Sun, Y., Day, R.N., and Periasamy, A. *Investigating protein-protein interactions in living cells using fluorescence lifetime imaging microscopy*. *Nature Protocols*, **6**:1324–1340, 2011.
- [14] Pepperkok, R., Squire, A., Geley, S., and Bastiaens, P.I. *Simultaneous detection of multiple green fluorescent proteins in live cells by fluorescence lifetime imaging microscopy*. *Current Biology*, **9**(5):269–274, 1999.
- [15] Bloch, S., Lesage, F., McIntosh, L., Gandjbakhche, A., Liang, K., and Achilefu, S. *Whole-body fluorescence lifetime imaging of a tumor-targeted near-infrared molecular probe in mice*. *Journal of Biomedical Optics*, **10**(5):054003, 2005.
- [16] Klucken, J., Outeiro, T.F., Nguyen, P., McLean, P.J., and Hyman, B.T. *Detection of novel intracellular α -synuclein oligomeric species by fluorescence lifetime imaging*. *The FASEB Journal*, **20**(12):2050–2057, 2006.
- [17] Bransden, B. and Joachain, C. *Physics of Atoms and Molecules*. Pearson Education. Prentice Hall, 2003.
- [18] Bransden, B. and Joachain, C. *Quantum Mechanics*. Prentice Hall, 2000.
- [19] Sakurai, J. and Tuan, S. *Modern Quantum Mechanics*. Advanced book program. Benjamin/Cummings Pub., 1985.

-
- [20] Yariv, A. *Quantum Electronics*. Wiley, 1989.
- [21] Kelvin, L. *I. Nineteenth century clouds over the dynamical theory of heat and light*. Philosophical Magazine Series 6, **2**(7):1–40, 1901.
- [22] Linne, M. *Spectroscopic Measurement: An Introduction to the Fundamentals*. Academic Press, 2002.
- [23] Herzberg, G. and Huber, K. *Molecular Spectra and Molecular Structure*. No. v. 4 in Molecular Spectra and Molecular Structure. Van Nostrand, 1979.
- [24] Kristensson, G. *Elektromagnetisk vågutbredning*. Studentlitteratur, 1999.
- [25] Settersten, T.B. and Linne, M.A. *Modeling pulsed excitation for gas-phase laser diagnostics*. J. Opt. Soc. Am. B, **19**(5):954–964, 2002.
- [26] Cheng, D. *Field and Wave Electromagnetics*. Addison-Wesley series in electrical engineering. Addison-Wesley, 1989.
- [27] Svanberg, S. *Atomic and Molecular Spectroscopy: Basic Aspects and Practical Applications*. Advanced Texts in Physics. Springer, 2004.
- [28] Boyd, R. *Nonlinear Optics*. Academic Press. Academic Press, 2008.
- [29] Hilborn, R.C. *Einstein coefficients, cross sections, f values, dipole moments, and all that*. American Journal of Physics, **50**(11):982–986, 1982.
- [30] Eckbreth, A. *Laser Diagnostics for Combustion Temperature and Species*. Combustion Science and Technology Book Series. Gordon and Breach Publishers, 1996.
- [31] Brockhinke, A., Lenhard, U., Bulter, A., and Kohse-Hoinghaus, K. *Energy transfer in the OH $A^2\Sigma^+$ state: The role of polarization and of multi-quantum energy transfer*. Phys. Chem. Chem. Phys., **7**:874–881, 2005.
- [32] Reif, F. *Fundamentals of Statistical and Thermal Physics*. McGraw-Hill series in fundamentals of physics. McGraw-Hill, 1965.
- [33] Heard, D.E. and Henderson, D.A. *Quenching of OH ($A^2\Sigma^+$, $v=0$) by several collision partners between 200 and 344 K. Cross-section measurements and model comparisons*. Phys. Chem. Chem. Phys., **2**:67–72, 2000.

- [34] Sutton, J.A. and Driscoll, J.F. *Rayleigh scattering cross sections of combustion species at 266, 355, and 532 nm for thermometry applications*. Opt. Lett., **29**(22):2620–2622, 2004.
- [35] Svelto, O. *Principles of Lasers*. Springer, 2009.
- [36] Brackmann, C., Aldén, M., Bengtsson, P., Davidsson, K., and Pettersson, J. *Optical and mass spectrometric study of the pyrolysis gas of wood particles*. Appl Spectrosc., **57**:216–222, 2003.
- [37] Kienle, R., Lee, M.P., and Kohse-Höinghaus, K. *A detailed rate equation model for the simulation of energy transfer in OH laser-induced fluorescence*. Applied Physics B: Lasers and Optics, **62**:583–599, 1996.
- [38] Efremov, E.V., Buijs, J.B., Gooijer, C., and Ariese, F. *Fluorescence Rejection in Resonance Raman Spectroscopy Using a Picosecond-Gated Intensified Charge-Coupled Device Camera*. Appl. Spectrosc., **61**(6):571–578, 2007.
- [39] Funfschilling, J. and Williams, D.F. *CW Laser Wavelength Modulation in Raman and Site Selection Fluorescence Spectroscopy*. Appl. Spectrosc., **30**(4):443–446, 1976.
- [40] Tahara, T. and Hamaguchi, H.O. *Picosecond Raman Spectroscopy Using a Streak Camera*. Appl. Spectrosc., **47**(4):391–398, 1993.
- [41] Everall, N., Hahn, T., Matousek, P., Parker, A.W., and Towrie, M. *Picosecond Time-Resolved Raman Spectroscopy of Solids: Capabilities and Limitations for Fluorescence Rejection and the Influence of Diffuse Reflectance*. Appl. Spectrosc., **55**(12):1701–1708, 2001.
- [42] Matousek, P., Towrie, M., Stanley, A., and Parker, A.W. *Efficient Rejection of Fluorescence from Raman Spectra Using Picosecond Kerr Gating*. Appl. Spectrosc., **53**(12):1485–1489, 1999.
- [43] McGinty, J., Requejo-Isidro, J., Munro, I., Talbot, C.B., Kellett, P.A., Hares, J.D., Dunsby, C., Neil, M.A.A., and French, P.M.W. *Signal-to-noise characterization of time-gated intensifiers used for wide-field time-domain FLIM*. Journal of Physics D: Applied Physics, **42**(13):135103, 2009.
- [44] van Munster, E.B. and Gadella, T.W.J. *Fluorescence lifetime imaging microscopy (flim)*. In J. Rietdorf, ed., *Microscopy Techniques*, vol. 95 of *Advances in Biochemical Engineering/Biotechnology*, pp. 1301–1303. 2005.

-
- [45] Cubeddu, R., Comelli, D., D'Andrea, C., Taroni, P., and Valentini, G. *Time-resolved fluorescence imaging in biology and medicine*. Journal of Physics D: Applied Physics, **35**(9):R61, 2002.
- [46] Gerritsen, H.C., Draaijer, A., Heuvel, D.J., and Agronskaia, A.V. *Fluorescence lifetime imaging in scanning microscopy*. In *Handbook Of Biological Confocal Microscopy*, pp. 516–534. 2006.
- [47] Jr., T.W.G., Jovin, T.M., and Clegg, R.M. *Fluorescence lifetime imaging microscopy (FLIM): Spatial resolution of microstructures on the nanosecond time scale*. Biophysical Chemistry, **48**(2):221–239, 1993.
- [48] Elder, A., Schlachter, S., and Kaminski, C.F. *Theoretical investigation of the photon efficiency in frequency-domain fluorescence lifetime imaging microscopy*. J. Opt. Soc. Am. A, **25**(2):452–462, 2008.
- [49] Draaijer, A., Sanders, R., and Gerritsen, H.C. *Fluorescence lifetime imaging, a new tool in confocal microscopy*. In *Handbook of Biological Confocal Microscopy*, pp. 491–505. 1995.
- [50] Becker, W., Stiel, H., and Klose, E. *Flexible instrument for time-correlated single-photon counting*. Review of Scientific Instruments, **62**(12):2991–2996, 1991.
- [51] Resch-Genger, U. *Standardization and quality assurance in fluorescence measurements I: techniques*. Springer Series on Fluorescence. Springer, 2008.
- [52] Woods, R.J., Scypinski, S., Love, L.J.C., and Ashworth, H. *Transient digitizer for the determination of microsecond luminescence lifetimes*. Analytical Chemistry, **56**(8):1395–1400, 1984.
- [53] Ni, T.Q. and Melton, L.A. *Fuel equivalence ratio imaging for methane jets*. Appl. Spectrosc., **47**(6):773–781, 1993.
- [54] Ni, T. and Melton, L.A. *Two-Dimensional Gas-Phase Temperature Measurements Using Fluorescence Lifetime Imaging*. Appl. Spectrosc., **50**(9):1112–1116, 1996.
- [55] Agronskaia, A.V., Tertoolen, L., and Gerritsen, H.C. *Fast fluorescence lifetime imaging of calcium in living cells*. Journal of Biomedical Optics, **9**(6):1230–1237, 2004.
- [56] Chan, S.P., Fuller, Z.J., Demas, J.N., and DeGraff, B.A. *Optimized Gating Scheme for Rapid Lifetime Determinations of Single-Exponential Luminescence Lifetimes*. Analytical Chemistry, **73**(18):4486–4490, 2001.

- [57] Molter, T.W., McQuaide, S.C., Suchorolski, M.T., Strovas, T.J., Burgess, L.W., Meldrum, D.R., and Lidstrom, M.E. *A microwell array device capable of measuring single-cell oxygen consumption rates*. Sensors and Actuators B: Chemical, **135**(2):678–686, 2009.
- [58] Carlsson, K. and Philip, J. *Theoretical investigation of the signal-to-noise ratio for different fluorescence lifetime imaging techniques*. vol. 4622, pp. 70–78. SPIE, 2002.
- [59] Tadrous, P.J., Siegel, J., French, P.M., Shousha, S., Lalani, E.N., and Stamp, G.W. *Fluorescence lifetime imaging of unstained tissues: early results in human breast cancer*. The Journal of Pathology, **199**(3):309–317, 2003.
- [60] Bormann, F., Nielsen, T., Burrows, M., and Andresen, P. *Single-pulse collision-insensitive picosecond planar laser-induced fluorescence of OH $A^2\Sigma^2(\nu = 2)$ in atmospheric-pressure flames*. Applied Physics B: Lasers and Optics, **62**:601–607, 1996.
- [61] Wängberg, I., Edner, H., Ferrara, R., Lanzillotta, E., Munthe, J., Sommar, J., Sjöholm, M., Svanberg, S., and Weibring, P. *Atmospheric mercury near a chlor-alkali plant in Sweden*. Science of The Total Environment, **304**:29–41, 2003.
- [62] Ohe, S. *Distillation, vapor pressure, vapor-liquid equilibria*. <http://www.s-ohe.com>.
- [63] Luque, J. and Crosley, D. *LIFBASE: Database and Spectral Simulation Program (Version 1.5)*. SRI International Report MP 99-009, 1999.
- [64] Bessler, W.G., Schultz, C., Sick, V., and Daily, J.W. *A versatile modeling tool for nitric oxide LIF spectra*. Proceedings of the Third Joint Meeting of the U.S. Sections of The Combustion Institute, Chicago, March 16-19, (PI05), 2003.
- [65] Lee, T., Bessler, W.G., Kronemayer, H., Schulz, C., and Jeffries, J.B. *Quantitative temperature measurements in high-pressure flames with multiline NO-LIF thermometry*. Appl. Opt., **44**(31):6718–6728, 2005.
- [66] Durme, J.V., Dewulf, J., Leys, C., and Langenhove, H.V. *Combining non-thermal plasma with heterogeneous catalysis in waste gas treatment: A review*. Applied Catalysis B: Environmental, **78**:324–333, 2008.
- [67] Griffiths, J. and Barnard, J. *Flame and Combustion*. Blackie Academic & Professional, 1995.

-
- [68] Brackmann, C., Nygren, J., Bai, X., Li, Z., Bladh, H., Axelsson, B., Denbratt, I., Koopmans, L., Bengtsson, P., and Aldén, M. *Laser-induced fluorescence of formaldehyde in combustion using third harmonic Nd:YAG laser excitation*. Spectrochim Acta A Mol Biomol Spectrosc., **59**:3347–3356, 2003.
- [69] Kyritsis, D.C., Santoro, V.S., and Gomez, A. *The effect of temperature correction on the measured thickness of formaldehyde zones in diffusion flames for 355 nm excitation*. Experiments in Fluids, **37**:769–772, 2004.
- [70] Ahlman, D., Brethouwer, G., and Johansson, A.V. *Direct numerical simulation of a plane turbulent wall-jet including scalar mixing*. Physics of Fluids, **19**(6):065102, 2007.
- [71] Koban, W., Koch, J.D., Hanson, R.K., and Schulz, C. *Oxygen quenching of toluene fluorescence at elevated temperatures*. Applied Physics B: Lasers and Optics, **80**:777–784, 2005.
- [72] Ehn, A., Kaldvee, B., Bood, J., and Aldén, M. *Development of a Temporal Filtering Technique for Suppression of Interferences in Applied Laser-Induced Fluorescence Diagnostics*. Appl. Opt., **48**(12):2373–2387, 2009.
- [73] Faust, S., Dreier, T., and Schulz, C. *Temperature and bath gas composition dependence of effective fluorescence lifetimes of toluene excited at 266 nm*. Chemical Physics, **383**:6–11, 2011.
- [74] Alberty, R. and Silbey, R. *Physical Chemistry*. Wiley, 1997.
- [75] Cole, M.J., Siegel, J., Webb, S.E.D., Jones, R., Dowling, K., Dayel, M.J., Parsons-Karavassilis, D., French, P.M.W., Lever, M.J., Sucharov, L.O.D., Neil, M.A.A., Juškaitis, R., and Wilson, T. *Time-domain whole-field fluorescence lifetime imaging with optical sectioning*. Journal of Microscopy, **203**(3):246–257, 2001.
- [76] Webb, S.E.D., Gu, Y., Lévêque-Fort, S., Siegel, J., Cole, M.J., Dowling, K., Jones, R., French, P.M.W., Neil, M.A.A., Juškaitis, R., Sucharov, L.O.D., Wilson, T., and Lever, M.J. *A wide-field time-domain fluorescence lifetime imaging microscope with optical sectioning*. Review of Scientific Instruments, **73**(4):1898–1907, 2002.
- [77] Kristensson, E. *Structured Laser Illumination Planar Imaging SLIPI - Applications for Spray Diagnostics*. Ph.D. thesis, Lund University, 2012.

Summary of Papers

After the summary of each paper my own responsibility regarding the work is listed so as to clarify my role and what parts I am not responsible for.

Paper I: Different types of signals that stem from various types of light-matter interaction phenomena can in some cases differ in the temporal characteristic they show, such as those of fluorescence (which has a lifetime) and elastic scattering (which is instantaneous). In studying fluorescence signals in a scattering environment, where the possibility of spectral filtering is limited, the fluorescence tail can be analyzed in time-resolved point measurements. In this paper, demonstrations of such a scheme were performed in imaging, using sharp ICCD camera gates in combination with picosecond excitation to cut out the early parts of the total signal. Demonstrations of this were carried out in two measurement situations in which scattered light from droplets and short lived from a metal surface were discriminated, in order to visualize the flow dynamics by means of the tracer LIF. In accordance with this, a mathematical description of the signal detection involved was provided and was validated, such parameters as camera gate characteristics, time jitter and laser pulse duration being identified, discussed and incorporated into the model.

I was responsible for the experimental, modeling and analysis. Joakim Bood and I wrote the manuscript.

Paper II: In most combustion applications the combustion processes are contained in some ways, such as in power plants, or in boilers, for example, in order to be able to achieve a high level of efficiency of the processes involved. In such enclosed geometries, optical access is usually very limited, sometimes only one opening in the geometry being available. Therefore, optical techniques that can perform mea-

measurements from a single-ended optical access is of utmost importance. LIDAR (LIght Detection And Ranging) is one such technique, the light being collected there in the backward direction, which thus places very limited demands on optical access. In this paper, a LIDAR scheme is demonstrated in which a picosecond laser source in combination with a streak camera are used in order to provide a range resolution of less than 0.5 cm in single-shot measurements. The experimental scheme was also used to demonstrate different diagnostic tools such as particle mapping (e.g. soot), Rayleigh thermometry (for which high resolution is crucial because of the highly non-linear dependence upon each other of the signal and temperature) in 2-dimensions under lean flame conditions, Differential Absorption LIDAR (DIAL) (which measures the absorption and provides spatially resolved data).

Billy Kaldvee was the person mainly responsible for this work. I was involved in the experimental work and assisted in planning the experiments. Billy Kaldvee and Joakim Bood evaluated the results and wrote the paper.

Paper III: Formation of NO_x in combustion processes is a well known problem due to the toxic nature of these molecules. A traditional scheme to reduce several toxic molecules in flue gas treatment is through scrubbing, since these molecules are soluble in water. Whereas reduction of NO_2 is successfully performed through scrubbing, NO , which is present in greater concentrations than NO_2 , cannot be removed using this cost-efficient approach. Injecting ozone into the flue gas leads to the chemical reaction $NO + O_3 \rightarrow NO_2$ reducing the NO , this making an important contribution to flue gas treatment in a fairly cost efficient manner. In order to visualize NO and NO_2 with and without the presence of ozone, the chemical reaction zone was visualized. This was performed under laminar as well as turbulent flow conditions and showed good conversion of NO to NO_2 . The substantial increase in conversion that occurs under turbulent conditions concludes is rather efficient flue gas treatment making use of ozone, one which is possible in an application if the mixing is optimized.

Zhihua Wang had the overall responsibility for the work. I was involved in the experimental work and contributed to the part of the manuscript concerning the experimental setup.

Paper IV: Peroxide molecules (H_2O_2 and HO_2) are important intermediate species in combustion processes, such as in high pressure autoignition in engines as well as in low temperature regions in flame chemistry according to kinetics models commonly employed. Such molecules have traditionally been investigated by absorption measurements obtained

through infrared spectroscopy, since the excited electronic state of the peroxide molecules is a repulsive state, which leads to formation of hydroxyl molecules. In this paper, this photo-induced dissociation was utilized while making use of a UV laser (266 nm) in order to create OH -fragments that could be detected by conventional fluorescence excitation at around 283 nm. Due to the natural OH production in combustion, the natural OH contribution needs to be subtracted in order to image the OH formed through photo-dissociation. This experimental scheme was utilized in order to image peroxide molecules in flames. Since strong UV pulses could potentially produce OH fragments from a variety of species in the reaction and the post-flame zone, the signals were compared with modeled results, making use of two kinetic mechanisms, CHEMKIN-II and the Konnov detailed C/H/N/O reaction mechanism. From such flame simulations, concentrations of the major species responsible for quenching as well as temperature data, that relates to the absorption cross-sections and to quenching, enabled the strength of the laser-induced signals to be calculated and to be compared with the experimental results. It was found that the dominant sources of OH -photofragments are HO_2 , H_2O_2 and CH_3O_2 , listed in order of importance. A fourth source of photo induced OH radicals, which contributes to OH buildup in the post flame following photolysis, appears to be dominated by CO_2 . This was found to be the case by incorporating the photolysis of CO_2 of different photolysis efficiencies in the kinetic model and studying the development of OH concentration over time following photo-dissociation. These simulations were compared with experimental data, which showed close agreement with the simulated results.

The work was supervised by Joakim Bood and Olof Johansson. I was involved in the experimental work. The flame calculations were performed by Alexander Konnov.

Paper V: Quantitative species concentration measurements utilizing laser-induced fluorescence signals is a challenging task in combustion-process research. In combustion, the reaction zone, in which the combustion chemistry occurs, involves thousands of reaction species and a steep temperature gradient which affects the fluorescence signal. The paper aims at presenting a robust imaging technique for the determination of fluorescence quantum yield, which is inversely proportional to the fluorescence lifetime. Accumulated fluorescence lifetime imaging of formaldehyde was performed using 355 nm pico second pulses in a rich ($\Phi = 2.6$) air/methane flame. A two camera setup was employed, the data being evaluated by use of the evaluation scheme DIME, which is short for dual imaging and modeling evaluation. The overlapping

routine of the images was based on a mathematical scheme called simulated annealing. PLIF images of formaldehyde showed a double intensity region, indicating there to be a double concentration peak of formaldehyde in the vicinity of the reaction zone. Since the PLIF image was compensated for the difference in fluorescence quantum yield, the double peak disappeared, only one peak being left. The evaluated lifetimes obtained by use of the detector scheme showed agreement with the PMT measurements that were also performed.

I was responsible for this work, apart from the pixel-to-pixel overlap routine, performed by Olof Johansson, and the flame-speed calculations, performed by Bo Li.

Paper VI: Fluorescence lifetime imaging (FLI) is a tool widely used in biomedical optical microscopy studies, a verity of different measurement schemes having been developed there to provide high quality and useful information at an affordable price. This tool has not been used to any great extent in combustion and flow dynamic studies, however. The reason for this is that combustion and flow studies usually focus on transient phenomena taking place in the gas phase, this requiring single-shot measurements. Also, the fluorescence lifetimes of interest are in the nanosecond range, which places high demands on the FLI schemes, since these very often suffer from the signals being weak. In this paper a new approach for use in single-shot laser induced fluorescence studies, involving assessment of sub-nanosecond fluorescence lifetimes, is introduced and its use is demonstrated. The experimental setup consists of one picosecond laser and two ICCD cameras. Each camera acquires one PLIF image, the two cameras differing in their gating features. The pixel-to-pixel overlapped images obtained could then be arranged in a ratio-image, cancelling out the differences in concentration and the fluctuations and inhomogeneties in the laser sheet. Simulating the detection for each of the two cameras and utilizing the ICCD-camera gate characteristics enabled the relationship between a similar ratio and a fluorescence lifetime that was detected to be defined. Details of this procedure and guidelines regarding how to set up a similar experiment are provided in the paper. The experimental results show that sub-nanosecond fluorescence lifetimes could be determined with a standard deviation of around 15 %, the results being validated by means of streak camera measurements. Monte Carlo simulation of the detection was also performed in order to determine the efficiency of the detector scheme for different fluorescence lifetimes. In addition, a new evaluation algorithm was proposed for the evaluation of single exponential functions. Monte Carlo simulations showed the features of this algorithm to be superior to the existing evaluation

schemes traditionally used in fluorescence lifetime imaging.

I was responsible of this work apart from the pixel-to-pixel overlap algorithm and the derivation of the equation that provides a graphical interpretation of the mathematical requirement placed on the choice of the gate functions to be used.

Paper VII: Quantitative concentration measurements utilizing laser-induced fluorescence, which provides good signals for imaging, are nevertheless somewhat troublesome since some of the parameters are difficult to characterize, stabilize and determine, such as quenching, inhomogeneities in laser profiles, and detection efficiencies for example. Fluorescence lifetime imaging can be used to overcome this problem, making it possible to determine the concentrations of the quencher species directly on the basis of the fluorescence lifetimes involved. In this paper, the fluorescence lifetime of toluene is mapped as a function of the oxygen concentration in $O_2/N_2/C_7H_8$ -gas mixtures under atmospheric pressure and room temperature conditions. Also, oxygen concentration imaging was performed using DIME. Finally, Monte Carlo simulations were carried out in order to determine the efficiency of the oxygen concentration determination achieved by the use of DIME, the reader being provided guidelines concerning the range in which the oxygen concentration would need to have in order to optimize the study of flow.

I was responsible for this work.

Paper VIII: In research fields in which applied laser studies are carried out, such as biology, medicine, physics, engineering, and chemistry, spontaneous Raman studies provide such advantages as species specificity and the signal scaling linearly with the laser intensity. The major drawback of spontaneous Raman signals is that the signal is very weak compared with the other, interfering signals, such as scattered light and fluorescence. By default, elastically scattered light does not spectrally overlap the Raman signal, which is an inelastic process. Fluorescence, on the other hand, can in some cases overlap the Raman signal spectrally. Interfering fluorescence stemming from smaller molecules has quite well separated absorption lines. Accordingly, an excitation wavelength that avoids the interfering fluorescence from such species could be used for Raman measurements there. In real applications, on the other hand, such as measurements in tissues, in oily combustion environments, and the like, the absorption spectra of these large molecules have basically continuous absorption spectra and a wide spectral emissions that would very probably interfere with the Raman signal. In such a context, temporal filters that could be combined with other

types of filters were analyzed by use of a picosecond laser and a fast ICCD camera. The filtering approach was demonstrated both in Raman imaging and in Raman spectroscopy, guidelines for use of the technique and potential problems with it also being discussed. A rather straightforward evaluation scheme is presented for evaluation of the effectiveness of a temporal filter in connection with certain types of instrumentation. This evaluation deals with such parameters as time jitter, laser pulse duration, the characteristics of the ICCD camera gate function, the fluorescence lifetime of the interfering signal, the relative signal intensities and the delay times of the ICCD camera. In a given experimental situation in which these parameters apply, the fraction of the total signal that the Raman signal represents can be determined as well as how much of the Raman signal is detected, since some of the Raman photons are filtered out.

I was responsible for this work.

Paper IX: In performing quantitative LIF measurements the signal needs to be corrected for the fluorescence quantum yield, the size of which can be determined by means of fluorescence lifetime imaging (FLI). In addition to such corrections of fluorescence signals, FLI can be used for a number of applications that can be useful in measurement situations in which strong demands are placed on the quantitative parameters. This paper investigates the potential of using the DIME algorithm in combination with Structured Laser Illumination Planar Imaging (SLIPI) to perform quantitative measurements in harsh measurement environments involving such obstacles as multiple scattering, out-of-plane interfering fluorescence, and the like. Measurements of this sort were conducted in a toluene seeded gas jet having spatial variations in the fluorescence lifetime and imaged through the scattering medium ($OD = 2.3$) considerable improvement in the image quality and rather accurate fluorescence lifetime determination being shown.

I was responsible for this work apart from the SLIPI evaluation and hardware, which Elias Kristensson was responsible for.